

η' meson production in the $pp \rightarrow pp\eta'$ reaction near threshold

Paweł Moskał



Jagellonian University
Cracow 1998

Jagellonian University

Institute of Physics

η' meson production in the
 $pp \rightarrow pp\eta'$ reaction near threshold

Paweł Moskal

A doctoral dissertation prepared at the Institut of Nuclear Physics of the Jagellonian University and at the Institute of Nuclear Physics of the Forschungszentrum Jülich, submitted to the Faculty of Mathematics and Physics at the Jagellonian University, conferred by Prof. Dr. Lucjan Jarczyk

Cracow 1998

Abstract

η' meson production in the $pp \rightarrow pp\eta'$ reaction near threshold

The η' meson belongs to the ground state pseudoscalar meson nonet. According to the SU(3) classification its quark composition is similar to the structure of the η meson. However, due to the small pseudoscalar mixing angle ($\Theta_{PS} \approx 15^\circ$) the η' meson is predominantly a flavour singlet state and hence can comprise a significant amount of gluons. A possible gluon admixture would be reflected in the production mechanism of the η' meson in the elementary proton-proton reaction, it would modify an $\eta'pp$ coupling constant which determines the direct production amplitude, and it would also influence the potential of the proton- η' meson interaction. These issues make the investigations of the η' meson very interesting.

The total cross section for the production of the η' meson in the $pp \rightarrow pp\eta'$ reaction has been measured close to the kinematical threshold. The experiment has been carried out at the cooler synchrotron COSY using the internal proton beam and the hydrogen cluster target. The ejected charged particles were registered using the COSY - 11 detection system, which allow for an unique identification of positively charged particles and determination of their four - momentum vectors. Events with the creation of the η' meson were identified by means of the missing mass technique.

The obtained cross sections for the η' meson production are by about a factor of fifty smaller than the cross section for the production of the η meson at the same center of mass excess energies. Such large difference suggests that these mesons are produced in a rather different way.

Comparison of the measured cross section values with calculations based on the effective Lagrangian approach yields an upper limit for the $\eta'pp$ coupling constant.

The analysis of the energy dependence of the total cross section for the $pp \rightarrow pp\eta'$ reaction suggests that either the primary production amplitude decreases very close to threshold or that the proton- η' interaction is repulsive.

Contents

1	Introduction	1
I THE η' MESON PROPERTIES		
2	The η' meson structure	7
2.1	Discovery of the η' meson	7
2.2	Flavour-SU(3) symmetry	7
2.3	Mixing of the η and η' mesons	8
2.4	The η' mass problem	11
2.5	Contents of glueball in the η' meson	13
3	Dynamics of the $pp \rightarrow pp$ Meson reaction	15
3.1	Production mechanisms of the π^0 and η mesons in the proton-proton collision	15
3.2	Possible mechanisms of the $pp \rightarrow pp\eta'$ reaction	17
3.3	$NN\eta'$ coupling constant	18
II EXPERIMENT		
4	Method of the measurement	23
4.1	Experimental setup	23
4.2	Beam momenta	25
4.3	Principle of the cross section measurement	25
5	Detection system	27
5.1	Drift chambers	27
5.2	Scintillation detectors	30
5.2.1	S1, S2 and S7 hodoscopes	30
5.2.2	S3 detector and the time-of-flight calibration	32
5.3	Silicon detector	35
6	Data evaluation	37
6.1	Data acquisition	37
6.2	Trigger logic - hardware event selection	37
6.3	Off-line analysis - software event selection	40
6.4	$pp \rightarrow pp\eta'$ reaction identification	42

7	Luminosity determination	47
8	Absolut beam momentum determination	51
9	Detection efficiency	55
9.1	Efficiency definition	55
9.2	Beam momentum spread	55
9.3	Target and beam dimensions	56
9.4	Geometrical acceptance	59
9.5	Efficiency of the track reconstruction in the drift chambers	61
9.6	Energy loss analysis - events with close flying particles	63
 III RESULTS AND DISCUSSION		
10	Total cross section	69
11	Comparison with model predictions	71
11.1	proton-proton final state interaction	71
11.2	One-pion-exchange model	73
11.3	Born-term - upper limit for the $pp\eta'$ coupling constant	75
11.4	Comparison of the production amplitudes for the $pp \rightarrow pp\pi^0$, $pp \rightarrow pp\eta$, and $pp \rightarrow pp\eta'$ reactions	76
12	Conclusion and perspectives	79
 IV APPENDICES		
A	Formula for the cross section	83
B	Phase space factors	87
C	Proton-proton final state interaction	91
D	Dominant partial waves	95
E	Jacobi coordinates system	97
F	Reaction kinematics	101
	Acknowledgement	105
	References	107

1. Introduction

Experiments carried out in recent years at the new accelerators such as IUCF, CELSIUS, and SATURNE, delivered precise data on the π^0 and η mesons production in proton-proton collisions near the kinematical threshold. These data enable investigations of the reaction dynamics and the final state interaction between the produced meson and nucleons. The hitherto existing investigations have shown that the short range component of the $N-N$ force and the off-shell pion rescattering dominate the production process of the π^0 meson [1], whereas the η meson is predominantly produced through the excitation of the intermediate baryonic resonance [2, 3]. It was also established that the η production cross section is largely influenced by the strong η -proton interaction [4, 3].

In context of the extensive experimental and theoretical studies of the π^0 and η production it is natural to ask about the mechanism of the η' production - the heaviest partner of these mesons in the pseudoscalar meson nonet - and about the strength of the η' -proton interaction. The investigations concerning the η' meson are particularly interesting since it is predominantly a flavour-singlet state and hence it can couple directly to gluons. Therefore one plausible production mechanism, suggested by N. Nikolaev, can be a fusion of gluons emitted from the two colliding protons, which is complementary to meson exchange current and would probe the gluonic content of the η' meson [5]. At present, any quantitative conclusions are not possible because of the lack of the theoretical calculations, however the data on the η' meson production in the nucleon-nucleon and γ -nucleon collisions enables the studies [6, 7] of this intricate issue.

There exists a lot of open issues concerning, for example, the unexplained large mass or just mentioned gluonium contents of the η' meson. None of the experimentally observed baryonic resonances decays into the η' meson, whereas many of them decay into pions, kaons or η mesons. This and other interesting issues concerning the η' will be presented in the first part of this work, which gives a review of the present knowledge of this meson.

The main purpose of this dissertation, however, is the determination of the total cross section for the $pp \rightarrow pp\eta'$ reaction at a few excess energies close to the kinematical threshold, and the discussion of the results in context of the production mechanism by the confrontation of the experimental data with the existing theoretical calculations as well as by the comparison of the obtained data with the production of the η and π^0 mesons. Measurements close to the kinematical threshold have both experimental and theoretical advantages. This is because measuring the meson production close to threshold with the fixed target allows to register all ejectiles by means of relatively small detectors, and in the

theoretical analysis it is enough to consider only an S-wave production in the exit channel.

One of the interesting conclusions will be the estimation of the upper limit for the proton- η' coupling constant under some plausible model assumptions. It is worth noting that the proton- η' coupling $g_{\eta'pp}$ measures the total spin of the proton carried by its constituent quarks [8].

The data on the η' as well as on the η and π^0 meson production in the proton-proton collisions are useful for an understanding of the dilepton mass spectra measured in the heavy-ion collisions in order to study the properties of the vector mesons in a dense nuclear matter [9, 10]. The π^0 , η and η' contributions to the e^+e^- invariant mass spectra arise from the Dalitz decay of these mesons.

A few months before the experiment presented in this thesis was performed, the data have been published concerning the η' meson production in the $pd \rightarrow {}^3\text{He} \eta'$ reaction, which have been obtained at the SATURNE accelerator using the SPES4 spectrometer [11]. The evaluated total cross section amounts to $\sim 0.16 \text{ nb}$ at an excess energy of $Q = 0.5 \text{ MeV}$. However, there were no published data concerning the total cross section for the $pp \rightarrow pp\eta'$ reaction close to the kinematical threshold. The only existing very preliminary results, obtained by the SPES3 collaboration, revealed that the near threshold total cross section for the $pp \rightarrow pp\eta'$ reaction is two or three orders of magnitude lower than the one for the η production [12]. Therefore a cross section in the order of one nanobarn was expected.

The only known values of the total cross section for the $pp \rightarrow pp\eta'$ reaction were measured far above threshold at excess energies of $Q = 793 \text{ MeV}$ and $Q = 2100 \text{ MeV}$, and amount to 0.08 mb (upper limit) and $1.96 \text{ mb} \pm 0.3 \text{ mb}$, respectively [13]. The extrapolation to excess energies of a few MeV above threshold, as given by the at that time only existing model [14], predicted values smaller than 50 nb .

The presented in this dissertation experiment was performed by the COSY - 11 collaboration¹ at the proton beam of the COSY-Jülich accelerator [15] by means of the internal hydrogen cluster target [16] installed in front of a regular COSY dipole magnet, which acts as a spectrometer. The charged ejectiles were registered by the COSY - 11 detection system [17], and the η' mesons were identified via the missing mass method [18, 19].

The work is divided into four parts. The first one comprises a detailed description of the η' meson properties and presents the most interesting issues concerning the physics of this meson. Specifically, the so called mass problem, the probable gluonium content, the missing resonance problem, and the possible dynamics of the $pp \rightarrow pp\eta'$ reaction will be discussed. Most of the presented issues will not be

¹List of the COSY - 11 collaborators:

J.T. Balewski, A. Budzanowski, H. Dombrowski, C. Goodman, D. Grzonka, L. Jarczyk, M. Jochmann, A. Khoukaz, K. Kilian, M. Köhler, A. Kozela, T. Lister, P. Moskal, W. Oelert (spokesman), I. Pelmann, C. Quentmeier, R. Santo, G. Schepers, U. Seddik, T. Seifick, S. Sewerin, J. Smyrski, M. Sokołowski, A. Strzałkowski, C. Thomas, M. Wolke, P. Wüstner, and D. Wyrwa

solved by this work. They are mentioned in order to show that the structure of the η' is still not established and that studies of this meson are connected with current and interesting problems of physics.

The second part describes the performed experiment. A discussion of all issues regarding the data evaluation is preceded by the presentation of the COSY - 11 detection system and the description of the calibration of each detector. In separate chapters methods of the determination of the luminosity, true beam momentum, and the detection efficiency are described.

In the third part the evaluated values of the total cross section are shown and compared with simple model predictions. In the discussion, the recently reported results obtained at the SATURNE accelerator using the SPES3 spectrometer [20] are also included. Some conclusions concerning the production mechanism and the proton- η' coupling constant will be drawn. Specifically, the influence of the proton-proton final state interaction on the energy dependence of the total cross section will be discussed.

The last part comprises appendices, which show explicitly the derivations of some formulas used in the text. For example, the method of calculating the proton-proton scattering amplitude is presented, and it is shown, based on the conservation laws and the Pauli excluding principle, why the transition between ${}^3P_0 \rightarrow {}^1S_0$ partial waves dominates the production close to the kinematical threshold.

PART I

THE η' MESON PROPERTIES

When one attempts to construct a realistic model of nature one is often confronted with the difficulty that most simple models have too much symmetry

G.'t Hooft

2. The η' meson structure

2.1 Discovery of the η' meson

First evidence of the existence of the η' meson has been seen in 1964 in the reactions $K^- + p \rightarrow \Lambda + \text{neutrals} + \text{charged pions}$ investigated independently by G.R. Kalbfleisch et al. [21] and M. Goldberg et al. [22]. Both experiments were performed by means of bubble chamber detectors with K^- beams having momenta in the range between 2.3 and 2.7 GeV/c . The η' meson was identified as a peak in the missing mass spectrum observed for the $K^-p \rightarrow \Lambda X^0$ reactions, and also as a clear enhancement in the distribution of the effective mass obtained from the measured five pions in the $K^-p \rightarrow \Lambda\pi^+\pi^+\pi^0\pi^-\pi^-$ reaction.

A spectrum of the effective mass of four possible $\pi^+\pi^0\pi^-\pi^-$ combinations from the $\Lambda\pi^+\pi^+\pi^0\pi^-\pi^-$ events resulted in a clean peak corresponding to the η meson mass [21]. This indicated that the discovered meson decays into π^+ , π^- and η mesons¹. At present many other decay channels are established, however the structure of the η' meson is still not well understood.

2.2 Flavour-SU(3) symmetry

In the year of the discovery of the η' meson Gell-Mann and Zweig independently postulated a hypothetical triplet of quarks (u-up, d-down, s-strange) [23, 24], which transforms according to the representations of the special unitary group SU(3), and which is fully symmetric under the strong interaction. All proposed quarks should have the same masses.

In this quark theory mesons are interpreted as bound states of quark-antiquark systems ($q\bar{q}$), which transform among themselves as a representation of the product of the SU(3) group and its complex conjugate. Therefore they should form

¹For completeness some properties of the η' meson are listed below [25]:

some quantum numbers:

$$I^G(J^{PC}) = 0^+(0^{-+})$$

mass: $m_{\eta'} = 957.77 \pm 0.14 MeV/c^2$

width: $\Gamma_{\eta'} = 0.201 \pm 0.016 MeV/c^2$

main decay modes:

mode	$\Gamma/\Gamma_{\eta'}$
$\pi^+\pi^-\eta$	$(43.7 \pm 1.5)\%$
$\rho^0\gamma$	$(30.2 \pm 1.3)\%$
$\pi^0\pi^0\eta$	$(20.8 \pm 1.3)\%$
$\omega\gamma$	$(3.02 \pm 0.30)\%$
$\gamma\gamma$	$(2.12 \pm 0.13)\%$

the SU(3)-octet and -singlet states.

Three different types of quarks -flavours- allow to construct nine different quark - antiquark ($q\bar{q}$) combinations all having the same spin and parity (for example pseudoscalar or vector nonets). Three of them, namely $u\bar{u}$, $d\bar{d}$ and $s\bar{s}$ are flavour neutral, and their superposition, in case of the ground pseudoscalar meson nonet, should correspond to the mesons π^0 , η_8 and η_1 .

The η_1 state being an SU(3)-singlet contains equal amounts of $u\bar{u}$, $d\bar{d}$ and $s\bar{s}$ combinations [23]:

$$\eta_1 = \frac{1}{\sqrt{3}}(u\bar{u} + d\bar{d} + s\bar{s}). \quad (2.1)$$

As the η_1 , the η_8 state has isospin equal to zero and comprises the isospin singlet state ($u\bar{u} + d\bar{d}$). On the other hand, the η_8 state must be orthogonal to the η_1 one, which implies that:

$$\eta_8 = \frac{1}{\sqrt{6}}(u\bar{u} + d\bar{d} - 2s\bar{s}). \quad (2.2)$$

Particles belonging to the pseudoscalar meson octet differ drastically in mass among each other, which indicates that the flavour-SU(3) symmetry is violated. Only partly these mass differences can be explained by the much larger mass of the strange quark compared to the masses of up and down quarks. However, the flavour-SU(3) classification is still successful, and most of the mesons discovered so far which consist of only u-, d- and s- quarks could be assigned to the octet or singlet representation of the SU(3) symmetry group [24].

2.3 Mixing of the η and η' mesons

The physical η and η' mesons are mixtures of the pure SU(3)- η_1 and $-\eta_8$ states. By introducing a pseudoscalar mixing angle Θ one can define the real η and η' meson wave functions as follows ²:

$$\begin{aligned} \eta &= \cos\Theta \cdot \eta_8 - \sin\Theta \cdot \eta_1, \\ \eta' &= \sin\Theta \cdot \eta_8 + \cos\Theta \cdot \eta_1. \end{aligned} \quad (2.3)$$

Knowing the η and η' meson masses as well as the mass of the η_8 state one can calculate the mixing angle according to the equation derived in reference [26]:

$$\sin^2\Theta = \frac{m_{\eta_8}^2 - m_{\eta}^2}{m_{\eta'}^2 - m_{\eta}^2}. \quad (2.4)$$

²In this work the mixing notation introduced by Gilman and Kauffman [27] will be used, see also recent work of Bramon, Escribano and Scadron [28].

The mass of the η_8 state can be obtained from the Gell-Mann-Okubo mass formula for the pseudoscalar meson multiplet [26, 29]:

$$m_{\eta_8}^2 = \frac{4}{3} \cdot m_K^2 - \frac{1}{3} \cdot m_\pi^2. \quad (2.5)$$

This relation was inferred under the assumptions that the masses of quarks are not the same and that the binding energies of quarks within a given meson multiplet are independent of the quark flavours [26]. The former assumption violates the SU(3) symmetry, and thus is responsible for the mass splitting within an SU(3)-octet.

Taking the experimental masses of the π , K , η and η' mesons and using the two above introduced equations one obtains the mixing angle for the pseudoscalar mesons to be about³ $\Theta \approx -11^\circ$. However, regarding the chiral corrections⁴ in the calculations of m_{η_8} [27] results in $\Theta = -20^\circ$ ⁵.

In the remaining part of this section a few other possibilities of determining the pseudoscalar mixing angle will be presented.

One of the first experimental determinations of the pseudoscalar mixing angle Θ was performed by comparing the production cross sections for the $\pi^+p \rightarrow \Delta^{++}\eta'$ and the $\pi^+p \rightarrow \Delta^{++}\eta$ reactions [30]. The ratio of the cross sections at a beam momentum of 8 GeV/c led to $\Theta = -11^\circ \pm 6^\circ$. For the calculations the relation [30]

$$\frac{\sigma(\pi^+p \rightarrow \Delta^{++}\eta)}{\sigma(\pi^+p \rightarrow \Delta^{++}\eta')} = (\text{kinematical factors}) \cdot \text{ctg}^2(\Theta - \Theta_{ideal}) \quad (2.6)$$

(predicted by the nonet-symmetry) was used, where $\Theta_{ideal} = -\arctan(\sqrt{2}) \approx -54.7^\circ$ denotes the ideal mixing angle. The up to date analysis based on the ratio between the reactions $\pi^-p \rightarrow \eta'n$ and $\pi^-p \rightarrow \eta n$ results in $\Theta = -17.3 \pm 1.8$ [28].

Another way for the determination of the $\eta - \eta'$ mixing angle was the study of the $\gamma\gamma$ decay widths for the η and η' mesons. In this case one can use the relation [31, 27, 32, 33, 34]:

$$\frac{\Gamma(\eta' \rightarrow \gamma\gamma)}{\Gamma(\eta \rightarrow \gamma\gamma)} = \frac{m_{\eta'}^3 \cdot \left[\frac{1}{f_8} \cdot \sin\Theta + \frac{\sqrt{8}}{f_1} \cdot \cos\Theta \right]^2}{m_\eta^3 \cdot \left[\frac{1}{f_8} \cdot \cos\Theta - \frac{\sqrt{8}}{f_1} \cdot \sin\Theta \right]^2} \quad (2.7)$$

where f_1 and f_8 are the decay constants of the singlet and eighth component of the octet, respectively ($f_8 \approx 1.2 \cdot f_1$) [27, 33]. The investigation of the η' or η decay

³The minus sign is chosen because the η' meson is heavier than η and thus should contain more strangeness. See also comments in reference [35].

⁴The one loop chiral corrected relation reads: $m_{\eta_8}^2 = \frac{4}{3}m_K^2 - \frac{1}{3}m_\pi^2 - \frac{2}{3} \frac{m_K^4}{(4\pi f_\pi)^2} \ln(m_K^2/\mu^2)$, where $\mu \approx 1$ GeV and f_π denotes the pion decay constant [27]

⁵The chiral corrected value of Θ is only accidentally equal to the one obtained from the linear Gell-Mann-Okubo relation ($m_{\eta_8} = \frac{4}{3} \cdot m_K - \frac{1}{3} \cdot m_\pi$), which is not relevant for the pseudoscalar mesons [29]. This is because the quark binding energies of these mesons are comparable with the constituent quark masses, hence one can not add them nonrelativistically.

widths was performed by the observation of the photons produced in the reactions $e^+e^- \rightarrow e^+e^-\eta'(\eta) \rightarrow e^+e^-\gamma\gamma$. The mixing angle Θ obtained in such a manner ranges between -21° and -17° [33, 36]. The new analysis of the two photon decays of π^0 , η and η' with regard of the SU(3)-breaking effects ($\frac{m_u+m_d}{2m_s} = 0.67$) gives $\Theta = -12.3^\circ \pm 2.0^\circ$ [28].

It is also possible to infer about the pseudoscalar mixing angle by studying the charmonium ($c\bar{c}$) decay into pseudoscalar and vector mesons. In this case it is conveniently to express the η and η' meson wave functions in the up, down and strange quark basis [37, 28]:

$$\begin{aligned}\eta &= X_\eta \cdot \frac{1}{\sqrt{2}}(u\bar{u} + d\bar{d}) + Y_\eta \cdot s\bar{s} \\ \eta' &= X_{\eta'} \cdot \frac{1}{\sqrt{2}}(u\bar{u} + d\bar{d}) + Y_{\eta'} \cdot s\bar{s}\end{aligned}\quad (2.8)$$

where, X and Y describe the nonstrange and strange quarkonium contents, respectively. Combining equations 2.8, 2.3, 2.1 and 2.2 one can relate the mixing angle Θ to the X and Y parameters [28]:

$$\tan\Theta = -\frac{\sqrt{2}X_\eta + Y_\eta}{X_\eta - \sqrt{2}Y_\eta} = \frac{X_{\eta'} - \sqrt{2}Y_{\eta'}}{\sqrt{2}X_{\eta'} + Y_{\eta'}}. \quad (2.9)$$

The values for X and Y can be obtained from the study of the various J/ψ decay modes. For example, the comparison of branching ratios of the J/ψ decay into $\omega\eta$ and $\rho^0\pi^0$ gives an X_η value as [38]:

$$\frac{B(J/\psi \rightarrow \omega\eta)}{B(J/\psi \rightarrow \rho^0\pi^0)} = X_\eta^2. \quad (2.10)$$

The η - η' mixing angle, obtained from the data on the J/ψ meson decay measured at the MARK III and DM2 detectors, amounts to $-16.9^\circ \pm 1.7^\circ$ [39].

The most up to date value of the pseudoscalar mixing angle Θ , averaged over all present experimental results, discussed widely in reference [28], amounts to:

$$\Theta = -15.5^\circ \pm 1.3^\circ. \quad (2.11)$$

It is worth noting that this value is centered inbetween the predictions based on the Gell-Mann-Okubo mass relation (-11°) and its chiral corrected version (-20°).

The relatively small octet-singlet mixing angle ($\Theta = -15.5^\circ$) implies that the η' meson is predominantly built out of the SU(3)-singlet state and the η meson of the SU(3)-octet.

The pseudoscalar mixing angle Θ differs significantly from the ideal mixing angle $\Theta_{ideal} \approx -54.7^\circ$. In case of the ideal η - η' mixing the η would consist of nonstrange quarks only, and the η' would be a pure $s\bar{s}$ state. The approximately ideal mixing takes place in the case of the vector mesons ϕ and ω .

At the beginning of this section it was stated that the η' is a mixture of the SU(3)- η_1 and $-\eta_8$ states. More generally it should be pointed out that this meson is a mixture of all flavour neutral SU(3) states [40]. However, the mixing between $\pi^0 - \eta$ and $\pi^0 - \eta'$, which arises from the mass difference between up and down quarks is much smaller than the $\eta - \eta'$ one, which is mainly due to the mass difference between strange and nonstrange quarks [41]. The analysis of the $\pi^0 - \eta - \eta'$ mixing, described in reference [40], revealed that the $\pi^0 - \eta'$ mixing is more than one order of magnitude smaller than the $\eta - \eta'$ one, and hence can be neglected.

The mixing angle Θ implies univocally the strange and nonstrange quark contents of η and η' mesons ($X_\eta = Y_{\eta'} \approx \cos(\Theta + 54.7)$, $Y_\eta = -X_{\eta'} \approx -\sin(\Theta + 54.7)$) [28]. Specifically, $\Theta = -15.5^\circ$ yields:

$$\begin{aligned}\eta &= 0.77 \cdot \frac{1}{\sqrt{2}}(u\bar{u} + d\bar{d}) - 0.63 \cdot s\bar{s}, \\ \eta' &= 0.63 \cdot \frac{1}{\sqrt{2}}(u\bar{u} + d\bar{d}) + 0.77 \cdot s\bar{s}\end{aligned}\quad (2.12)$$

The obtained similar amounts of strange and nonstrange quarkonium in both η and η' mesons suggests that the masses of these particles should be similar in magnitude. In reality, however, the η' is almost two times heavier than the η meson indicating that the structure of η or η' is more complicated than would be concluded from the mixture of the SU(3)-flavour states.

2.4 The η' mass problem

The π mesons possess exactly the same quark structure as the ρ mesons, however, their masses differ by more than a factor of five. The only difference between these mesons is their spin configuration. In the π mesons the quark and antiquark spins are antiparallel whereas in the ρ mesons they are parallel, indicating a significant contribution of the quark spin-spin interaction to the meson masses. Regarding this effect allows to relate meson mass to quark masses more generally than given by the Gell-Mann-Okubo mass formula.

The energy shift caused by the spin-spin coupling is proportional to the dot product of the spins and inversely proportional to the product of the quark constituent masses. Thus one can relate the mass of the $q\bar{q}$ system to the quark masses by the following expression [42, 43]:

$$m_{q_1\bar{q}_2} = m_{q_1} + m_{\bar{q}_2} + A \cdot \frac{\vec{S}_1 \cdot \vec{S}_2}{m_{q_1} \cdot m_{\bar{q}_2}}, \quad (2.13)$$

Meson	Calculated mass [MeV/c ²]	Observed mass [MeV/c ²]
π	140	138
K	484	496
η	559	549
η'	349	958
ρ	780	776
ω	780	783
K*	896	892
ϕ	1032	1020

Table 2.1: Pseudoscalar and vector meson masses [42]. In the calculations the mixing between SU(3) states was neglected.

where, A is a constant value and \vec{S}_i denotes the quark spin ⁶.

Assuming that the parameter A is the same for the vector and pseudoscalar meson nonets and fitting equation 2.13 to all mesons from these multiplets results in the constituent quark masses and the value of the parameter A, ($m_u = m_d = 310 \frac{MeV}{c^2}$, $m_s = 483 \frac{MeV}{c^2}$, $A = (2m_u/\hbar)^2 160 \frac{MeV}{c^2}$) [42]. Now conversely, having these values one can calculate the meson masses using equation 2.13. Table 2.1 shows the comparison of experimental and calculated meson masses. The mass formula 2.13 matches simultaneously, within an accuracy of 2%, all mesons from the vector and pseudoscalar ground nonets **except the mass of the η' meson**, which is predicted to be almost a factor of three smaller than the observed one⁷. According to equation 2.13, even if the η' meson would be a pure $s\bar{s}$ system, its mass would amount to $\sim 768 MeV/c^2$, which is still almost 200 MeV/c^2 less than the observed η' mass. The difficulty in describing the η' mass becomes even more surprising when one realizes that not only the masses of pseudoscalar or vector mesons are well described in terms of quark models but also the masses of other hadrons like tensor mesons [44] or baryons [29].

There exist many theoretical models, mainly connected with the proposal of G.'t Hooft [45] based on the ‘‘U(1) anomaly’’, trying to explain the large η' meson mass. For example, one considers the two-gluon annihilation process $gg \longleftrightarrow q\bar{q}$ as a contribution to the SU(3)-flavour singlet state [46, 51, 52]. Because of the small pseudoscalar mixing angle such an additional gluon-induced interaction should mainly affect the properties of the η' which is predominantly built out of the

⁶The dot product $\vec{S}_1 \cdot \vec{S}_2$ amounts to $\frac{1}{4}\hbar^2$ for the vector mesons and $\frac{-3}{4}\hbar^2$ for the pseudoscalar ones.

⁷The present values of the meson masses [25] differ within 1% from the ones in reference [42] shown in table 2.1

SU(3)-flavour singlet state. In order to reproduce the observed η' mass, a gluonium component ranging between 29% and 53% is required [53].

Similarly the analysis of the production cross sections of the η and η' mesons in the pion-proton and kaon-nucleon collisions, revealed that the predictions under the assumption that the η and η' are mixtures of the SU(3)-flavour states, disagree with the experimental results [54, 55].

2.5 Contents of glueball in the η' meson

The additional admixture in the η' wave function could be for example $q\bar{q}$ state made of charmed or heavier quarks. However, the appreciable contents of the $c\bar{c}$ is excluded by the observed $J/\psi \rightarrow \eta\gamma$ and $J/\psi \rightarrow \eta'\gamma$ decay rates [55]. Another possibility is that the η' , additionally to the combination of $u\bar{u}$, $d\bar{d}$ and $s\bar{s}$ quarkonium states, contains also their radial excitations [55, 56].

It is also possible that other states, predicted by the QCD theory, contribute to the η' wave function, as for example, hybrids containig glue like $q\bar{q}g$ or even pure glue states like gg or ggg called glueballs [44]. Thus, generally the η and η' wave function may be described as a linear combination of the quarkonium, radially excited $q\bar{q}$ states, gluonium, or other exotic objects [43, 57, 51]:

$$\begin{aligned}\eta &= X_\eta \cdot \frac{1}{\sqrt{2}}(u\bar{u} + d\bar{d}) + Y_\eta \cdot s\bar{s} + Z_\eta \cdot G \\ \eta' &= X_{\eta'} \cdot \frac{1}{\sqrt{2}}(u\bar{u} + d\bar{d}) + Y_{\eta'} \cdot s\bar{s} + Z_{\eta'} \cdot G,\end{aligned}\quad (2.14)$$

where G denotes the (gg) gluonium state as proposed by E. Kawai [57] and J. Rosner [43], combination of radial excited $q\bar{q}$ states as proposed by H. Lipkin [56], or hybrids. The coefficients X, Y and Z must satisfy the normalization condition $X^2 + Y^2 + Z^2 = 1$.

Investigating the two body decays of the J/ψ meson into a vector and a pseudovector meson ($\phi\eta$, $\omega\eta$, $\rho^0\eta$, $\phi\eta'$, $\omega\eta'$, $\rho^0\eta'$) the MARK III collaboration has established that [38]:

$$X_\eta^2 + Y_\eta^2 = 1.1 \pm 0.2, \quad X_{\eta'}^2 + Y_{\eta'}^2 = 0.65 \pm 0.18, \quad (2.15)$$

which indicates that the η meson is saturated by its quarkonium contents while the η' is **not**, $Z_{\eta'}^2 = 0.35$. Thus, the η' meson may contain as much as 35% of other than $q\bar{q}$ components. However, no answer about the nature of the missing admixture was obtained. The analysis was based on the assumption that the J/ψ meson annihilates into gluons or virtual photon which further convert into mesons.

Similar measurements of the charmonium decay were carried out later by the same group [37] as well as by the DM2 collaboration [58]. The data were analyzed including an additional *disconnected* diagram in the J/ψ decay. This analysis

has yielded that both the η and η' can be regarded as a pure combination of $q\bar{q}$ systems. For example, in the case of the η' it was found that $|Z_{\eta'}|^2 \approx 0.01$ [37, 58].

The above examples show that the amount of the gluonic component within the η' meson is still not established, and it is also not obvious how to deduce the relative gluonic and quark contributions in a model independent way [59].

Another interesting analysis was performed by K. Geiger et al. [60]. They have assumed that the η and η' mesons are mixed with $\eta(1440)$, and that all are composed of glueballs, strange and nonstrange quarkonium and of the $q\bar{q}$ radial excited states, similarly as in equation 2.14. They have identified the $\eta(1440)$ as a glueball state with a 25% admixture of quark-antiquark components. The η meson was found to be consistent with the pure quarkonic components with dominant nonstrange quark content, and the η' was determined to be mostly built out of strange quarks with an 18% admixture of gluonium. However, the $\eta - \eta' - \eta(1440)$ mixing ought to be revisited in view of the new results [61, 62] suggesting that the $\eta(1440)$ is separated into two resonances.

The connection of the η' to glue can also be inferred from the decay of the scalar meson $f_0(1500)$, which is supposed to be a glueball- $q\bar{q}$ mixture [61], and which decays more frequently into $\eta\eta'$ than into $\eta\eta$ [63].

Another indications of the gluonic contents of the η' mesons come from the measurements of the beauty particles decays performed by the CLEO collaboration [64, 65, 66]. The observed anomalously large branching ratio in the inclusive $B \rightarrow \eta' X$ decays suggests the strong coupling of the η' to gluons. Predictions of the standard model for the b-quark decays into light quarks, lead to results which are two orders of magnitude smaller than the data [67]. Specifically, the CLEO measurements of the $B \rightarrow \eta' K$ decay imply a significant gluon or charm content of the η' meson [67]. As far as charm is concerned the suggested mechanism is that the b-quark decays into $c\bar{c}s$ states and that further virtual $c\bar{c}$ converts into η' . However, this may be possible only if the η' meson contains significant amounts of $c\bar{c}$ [67]. On the other hand, as already mentioned, according to reference [55] the charmonium contents of the η' meson should be negligible.

One may conclude that the structure of the η' meson is still not well established and requires further experimental and theoretical investigations. Since the up to date knowledge of the η' meson is mostly based on studying of the decay of heavier mesons it would be very important to investigate the production of the η' for example in hadronic collisions.

3. Dynamics of the $pp \rightarrow pp$ Meson reaction

An essential point of the study of the $pp \rightarrow pp$ Meson reactions is the understanding of the reaction mechanisms and as a consequence the insight into the meson structure. The advent of the cooler storage rings enabled such investigations very close to the kinematical threshold, where the reaction may be described by only a few partial waves, which simplifies the theoretical analysis. The discussion of the possible processes which may contribute to the production of the η' meson in the proton-proton collision, will be preceded by the short review of the mechanisms, which are accounted for the creation of other neutral pseudoscalar mesons like π^0 and η .

3.1 Production mechanisms of the π^0 and η mesons in the proton-proton collision

The question which processes (on the mesonic level) are responsible for the π^0 meson production was considered already in 1966 by D.S. Koltun and A. Reitan [68]. The authors have calculated that the direct pion production on one of the protons, as shown in Figure 3.1a, plays the most important role in the $pp \rightarrow pp\pi^0$ reaction. However, the exact measurement of the total cross section

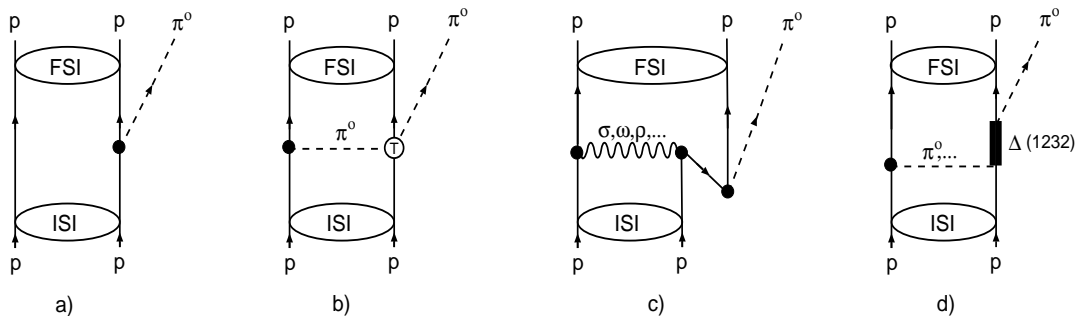


Figure 3.1: Feynman diagrams for the $pp \rightarrow pp\pi^0$ reaction near threshold: (a) direct term, (b) rescattering term, (c) production through the heavy-meson exchange, (d) resonant term, “ISI” and “FSI” denote proton-proton initial and final state interaction, respectively.

for the $pp \rightarrow pp\pi^0$ reaction performed at IUCF [69, 70] and CELSIUS [71] revealed that this mechanism can not account for more than 20% of the total reaction am-

plitude. Subsequent theoretical investigations showed that the inclusion of a process illustrated in Figure 3.1b, when the pion is produced on one proton and then scattered on the other one, increased the amplitude essentially but not enough to describe the data [72]. The further enhancement of the production amplitude comes from the exchange of heavy mesons shown in Figure 3.1c, where the σ and ω mesons [72, 73] exchange plays the dominant role. There exist also theoretical calculations indicating that the close to threshold π^0 production can be described without regarding the heavy meson exchange, provided that one takes the πN off shell amplitudes [74] into account. Finally, it is shown in reference [1] that both mechanisms, the heavy meson exchange and the off-shell pion rescattering are necessary in order to obtain agreement with the experiments. The resonant π^0 meson production, shown in Figure 3.1d, with the formation of the intermediate $\Delta(1232)$ state is strongly suppressed close to threshold, because of conservation laws¹.

In contrary, the creation of the η meson in the $pp \rightarrow pp\eta$ reaction is dominated by the intermediate $S_{11}(1535)$ state (see Figure 3.2), which further decays into η and proton² [75, 2, 76, 77]. The $S_{11}(1535)$ resonance is excited mainly by the exchange of the π , ρ or η mesons [4, 2, 77].

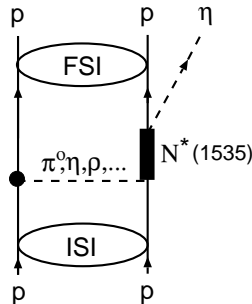


Figure 3.2: Dominant term for the $pp \rightarrow pp\eta$ production amplitude.

The production mechanisms for π^0 and η are appreciably different, however, in both cases the observed energy dependence for the total cross section close to threshold is determined predominantly by the phase space factors and the final state interaction of the outgoing particles [78, 79].

¹Close to threshold all particles are produced in the relative angular momentum of zero. The $\Delta(1232)$ resonance ($I(J^P) = \frac{3}{2}(\frac{3}{2}^+)$) decays into a p-wave πN system and can therefore contribute to s-wave meson production through a recoil term only [7].

²The branching ratio of the $S_{11}(1535)$ resonance into $N\eta$ system amounts to 30% – 55% [25].

3.2 Possible mechanisms of the $pp \rightarrow pp\eta'$ reaction

Similarly as depicted in the π^0 case, the η' meson can be produced via mechanisms depicted in Figures 3.3a-d. Since the η' is much heavier than the π^0 meson and its production requires much larger four momentum transfer between the interacting protons, it is expected that the creation through the heavy meson exchange, as illustrated in Figure 3.3c, will be even more significant than in the π^0 case. The resonant production via the excitation of a S_{11} resonance, can contribute already at the reaction threshold. However, in contrary to the η meson case, none such resonance is known, which may decay into an s-wave $\eta'N$ system³. Therefore one does not expect that the production via the excitation of the baryonic resonance will be appreciable. The only resonance which could be considered here is the $D_{13}(2080)$ [80] one⁴. However, due to its spin $\frac{3}{2}$, its contribution should be suppressed in the close to threshold $pp \rightarrow pp\eta'$ reaction.

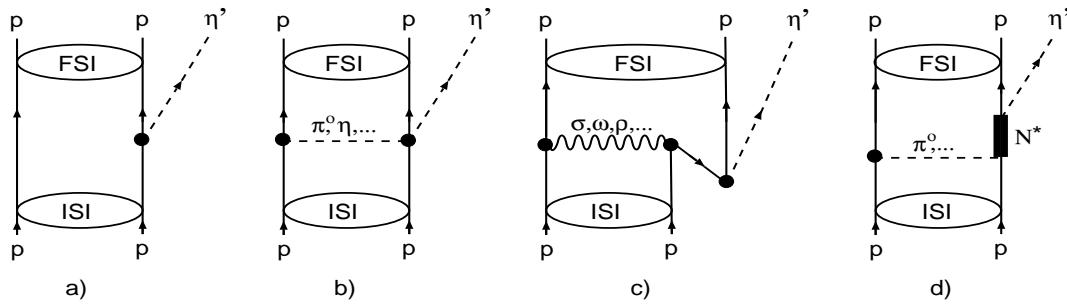


Figure 3.3: Feynman diagrams for the $pp \rightarrow pp\eta'$ reaction near threshold: (a) direct term, (b) “rescattering” term, (c) production through the heavy-meson exchange, (d) excitation of an intermediate resonance.

For the presented in this work measurement of the $pp \rightarrow pp\eta'$ reaction, we can not observe an appreciable influence of the probable N^* resonance on the total cross section energy dependence, because the range of the covered excess energy is smaller than $\sim 4 \text{ MeV}$ which is to be compared with a typical resonance width of about 100 MeV . However, the absolute values for the total cross section should differ significantly, depending whether the production is resonant or not. Unfortunately, till now, there exist no quantitative predictions of the production cross section for the $pp \rightarrow pp\eta'$ reaction. At present, even the contribution to the

³In the *relativized quark model* approach one predicts many nonstrange baryon resonances which should decay into η' [81, 82]. For instance, $S_{11}(2030)$, $D_{13}(2055)$, $D_{13}(2080)$, $S_{11}(2090)$ or $D_{13}(2095)$. The lack of the experimental confirmation of many predicted resonances in the $2 \text{ GeV}/c^2$ mass region is referred to as a **missing resonance problem** [80].

⁴The study of the $\gamma p \rightarrow \eta' p$ reaction revealed the existence of the $\mathbf{D}_{13}(2080)$ resonance [80, 50], which can decay into η' and proton.

total cross section from the direct production process, shown in Figure 3.3a, can not be established because of the large uncertainty of the coupling constant for the $NN\eta'$ vertex, which is discussed in the next section.

Additionally to the mechanisms which govern also the π^0 or η production, in case of the η' meson two other processes, shown in Figure 3.4 are proposed [7, 5, 83]. According to Figure 3.4a the η' meson would be emitted by a virtual ω , ρ , or σ meson, which couples strongly to the η' . The strong coupling is manifested by the decay of the η' into $\rho\gamma$ or $\omega\gamma$ (see page 7). The emission showed in diagram 3.4a may be understood as an inverse process to the η' decay. For instance, the $\omega\omega\eta'$ vertex is determined by the $\eta' \rightarrow \omega\omega^* \rightarrow \omega\gamma$ decay⁵, whereas the $\sigma\eta\eta'$ corresponds to the $\eta' \rightarrow \pi\pi\eta$ decay, with σ describing the two pions.

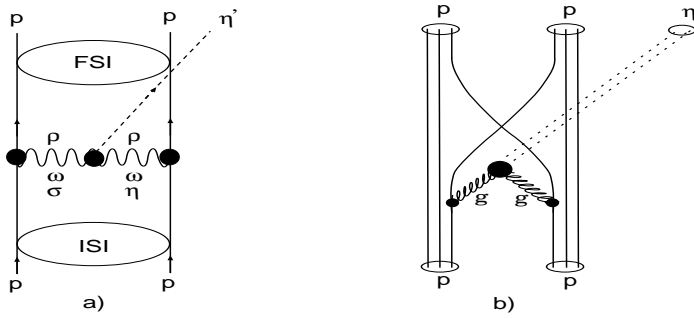


Figure 3.4: Diagrams for the $pp \rightarrow pp\eta'$ reaction near threshold: (a) emission from the virtual particle, (b) production via a fusion of gluons.

Since the η' meson is essentially built out of the SU(3)-flavour singlet state η_1 , which can couple to the purely gluonic states [47], it can also be produced in the fusion of gluons emitted from the exchanged quarks of the colliding protons, as shown in Figure 3.4b [5]. An evaluation of the contribution of this production mechanism to the total cross section would enable the insight into a probable gluonic contents of the η' meson. Unfortunately, at present there are no theoretical calculations concerning this mechanism. There are some plans to evaluate the meson-exchange mechanisms based on the measurements of the $\gamma p \rightarrow p\eta'$ reaction, where a gluon fusion is not expected. Next, having the parameters for the meson-exchange graphs fixed one could calculate the cross section for the $pp \rightarrow pp\eta'$ reaction. The probable discrepancy between the prediction based on the meson-exchange currents and the experimental data would reveal information about the gluons fusion mechanism [7].

3.3 $NN\eta'$ coupling constant

In the effective Lagrangian approach [80, 50] the strength of the nucleon- η' coupling is driven by the quantity $g_{NN\eta'}$ called the $NN\eta'$ coupling constant, which

⁵The ω^* denotes here the virtual ω

comprises the information about the structure of the η' meson and the nucleon. The knowledge of the coupling constant is necessary in the calculation of the production cross section if one considers the Feynman diagrams as illustrated in Figures 3.3. Specifically, the interaction Lagrangian describing the $NN\eta'$ production vertex from diagram shown in Figure 3.3a reads [80]:

$$L_{NN\eta'} = g_{NN\eta'} \left[-i\epsilon \bar{N} \gamma_5 N \eta' + (1 - \epsilon) \frac{1}{2M} \bar{N} \gamma_\mu \gamma_5 N \partial^\mu \eta' \right], \quad (3.1)$$

where, the γ 's indicate Dirac matrices and N and M denote the free nucleon field operator and the nucleon mass, respectively.

The first and second terms in equation 3.1 describe the pseudoscalar and pseudovector coupling, respectively. The value of the parameter ϵ indicates the relative contribution of these couplings. Till now the η' -nucleon coupling has not been determined experimentally. The main difficulty is due to the fact that usually the direct production on the nucleon is either associated with the production through baryonic resonances, as in the case of the $\gamma p \rightarrow \eta' p$ reaction, or through the exchange of other mesons. Therefore, if the direct production mechanism is not dominant it is not possible to extract the $NN\eta'$ coupling without the clear understanding of the other mechanisms.

Assuming that the η and η' mesons are mixtures of the SU(3) singlet and octet states, one can relate the $NN\eta$ and $NN\eta'$ coupling constants by the following equations [80]:

$$\begin{aligned} g_{NN\eta} &= \cos\Theta \cdot g_{NN\eta_8} - \sin\Theta \cdot g_{NN\eta_1} \\ g_{NN\eta'} &= \sin\Theta \cdot g_{NN\eta_8} + \cos\Theta \cdot g_{NN\eta_1}, \end{aligned} \quad (3.2)$$

where, $g_{NN\eta_8}$ and $g_{NN\eta_1}$ stand for the SU(3)-octet and singlet coupling constant, correspondingly. Further, assuming that the strange quark content in the nucleons is negligible one obtains that $\frac{g_{NN\eta_1}}{g_{NN\eta_8}} \approx \sqrt{2}$ [80]. This is because, the nonstrange quark content in the η_1 is by a factor of $\sqrt{2}$ larger than in the η_8 state - compare equations 2.1 and 2.2. It follows that:

$$g_{NN\eta'} = \frac{\sin\Theta + \sqrt{2}\cos\Theta}{\cos\Theta - \sqrt{2}\sin\Theta} \cdot g_{NN\eta} \stackrel{\Theta=-15.5^\circ(\text{page } 10)}{=} 0.82 \cdot g_{NN\eta}. \quad (3.3)$$

The measurements of the $\gamma p \rightarrow p\eta$ [84, 85] reaction have yielded that:

$$0.2 \leq g_{NN\eta} \leq 6.2, \quad (3.4)$$

whereas the comparison of the $\pi^- p \rightarrow \eta n$ and $\pi^- p \rightarrow \pi^0 n$ reaction cross sections implies [84]:

$$5.7 \leq g_{NN\eta} \leq 9.0, \quad (3.5)$$

and the estimation based on SU(3) relations ⁶ gives:

$$3.8 \leq g_{NN\eta} \leq 6.7. \quad (3.6)$$

⁶In the SU(3)-flavour model one obtains [86, 84] $g_{NN\eta_8} = \frac{1}{\sqrt{3}}(3 - 4\alpha_p)g_{NN\pi}$, where, $0.59 \leq \alpha_p \leq 0.66$ and $g_{NN\pi}^2/4\pi = 14.4$, which gives $2.8 \leq g_{NN\eta_8} \leq 5.0$. Next, applying equation 3.2 one obtains the relation 3.6.

The above inequalities and equation 3.3 lead to a following range for the $g_{NN\eta'}$ value:

$$4.7 \leq \mathbf{g}_{NN\eta'} \leq 5.1, \quad (3.7)$$

which is to be compared to the η' coupling determined from the fits to low energy nucleon-nucleon scattering in the one boson exchange models amounting to $g_{NN\eta'} = 7.3$ [87].

On the other hand, the $g_{NN\eta'}$ coupling constant determined via dispersion methods [88] turns out to be smaller than 1, $\mathbf{g}_{NN\eta'} < \mathbf{1}$, which is in contradiction to the above estimations.

The $g_{NN\eta'}$ coupling constant is also related to the issue of the total quark contribution to the proton spin ($\Delta\Sigma$). The approximate equation derived in reference [8] reads:

$$\Delta\Sigma = \Delta u + \Delta d + \Delta s = \frac{\sqrt{3}f_{\eta'}}{2M}g_{NN\eta'} \quad (3.8)$$

where, $f_{\eta'} \approx 166 \text{ MeV}$ [8] denotes the η' decay constant and M stands for the proton mass. Δu , Δd and Δs indicate the contributions from up, down and strange quarks, respectively ⁷. The total contribution of the quarks to the proton spin amounts to $\Delta\Sigma = 0.38^{+0.09}_{-0.10}$ [90]. Applying this value in equation 3.8 one obtains $\mathbf{g}_{NN\eta'} = 2.48^{+0.59}_{-0.65}$.

In any case, the coupling for the $NN\eta'$ vertex turns out to be essentially smaller than the $NN\pi$ one with $g_{NN\pi} = 13.45$ [86, 97].

Exact measurements of the $g_{NN\eta}$ and $g_{NN\eta'}$ coupling constants would test equation 3.3 and could verify the assumption used when deriving this equation, namely regarding η and η' as mixed SU(3)-flavour states and the neglect of the strange quark content within nucleons.

⁷Contribution of quarks heavier than the *strange* quark are normally not considered, but I. Halperin and A. Zhitnitsky suggested [89] that the intrinsic charm component of proton may also carry a significant amount of the proton spin. The quark and gluon contributions to the proton spin are widely discussed in the literature [90, 91, 92, 93, 94, 95, 96, 8] based on measurements of the spin asymmetries in deep-inelastic scattering of polarised muons on polarised protons.

PART II
EXPERIMENT

4. Method of the measurement

4.1 Experimental setup

The experiment was performed at the cooler synchrotron COSY-Jülich [15] which accelerates protons up to a momentum of $3400 \text{ MeV}/c$. The threshold momentum for the $pp \rightarrow pp\eta'$ reaction is equal to **3208.3 MeV/c**. About 10^{10} accelerated protons circulate in the ring passing $1.6 \cdot 10^6$ times per second through the H_2 cluster target [16] installed in front of one of the dipole magnets, as depicted schematically in Figure 4.1. The target¹ having a density of about $5 \cdot 10^{13} \text{ atoms}/\text{cm}^2$ is realized as a beam of H_2 molecules grouped inside clusters of about 10^4 atoms.

At the intersection point of the cluster beam with the COSY proton beam the collision of protons may result in the production of the η' meson. The ejected protons of the $pp \rightarrow pp\eta'$ reaction, having smaller momenta than the beam protons, are separated from the circulating beam by the magnetic field. Further they leave the vacuum chamber through a thin exit foil² and are registered by the detection system consisting of drift chambers and scintillation counters as depicted in Figure 4.1.

The measurement of the track direction by means of the drift chambers, and the knowledge of both the dipole magnetic field and the target position allow to reconstruct the momentum vector for each registered particle. The time of flight measured between the S1 (S2, S7) - and the S3 scintillators gives the particle velocity. Having momentum and velocity for each particle one can calculate its mass, and hence identify it, for example to be a proton. The knowledge of the momenta of both protons before and after a reaction allows to calculate a mass of a not observed particle or system of particles in the outgoing channel, which in case of the $pp \rightarrow pp\eta'$ reaction should be equal to the mass of the η' meson.

The energy loss information from the S1, S2, S7 and S3 scintillation detectors is used to verify the efficiency of the track reconstruction in the drift chambers in the case of two close tracks.

The scintillation detector S4 and the position sensitive silicon pad detector Si are used for the detection of one of the elastically scattered protons. The second, elastically scattered proton is registered in coincidence with the first one by both of the drift chambers and the S1 scintillation counter.

¹The H_2 cluster target is described in details in references [16, 98]. The dimensions of the beam-target overlap are discussed in chapter 9

²The exit foil consists of $30 \mu\text{m}$ layer of aluminium foil and $300 \mu\text{m}$ of an carrier material ($C_{89.4\%}$, $N_{4.1\%}$, $O_{6.2\%}$, $Cl_{0.3\%}$) with the averaged density of $2.1 \text{ g}/\text{cm}^3$ [17]

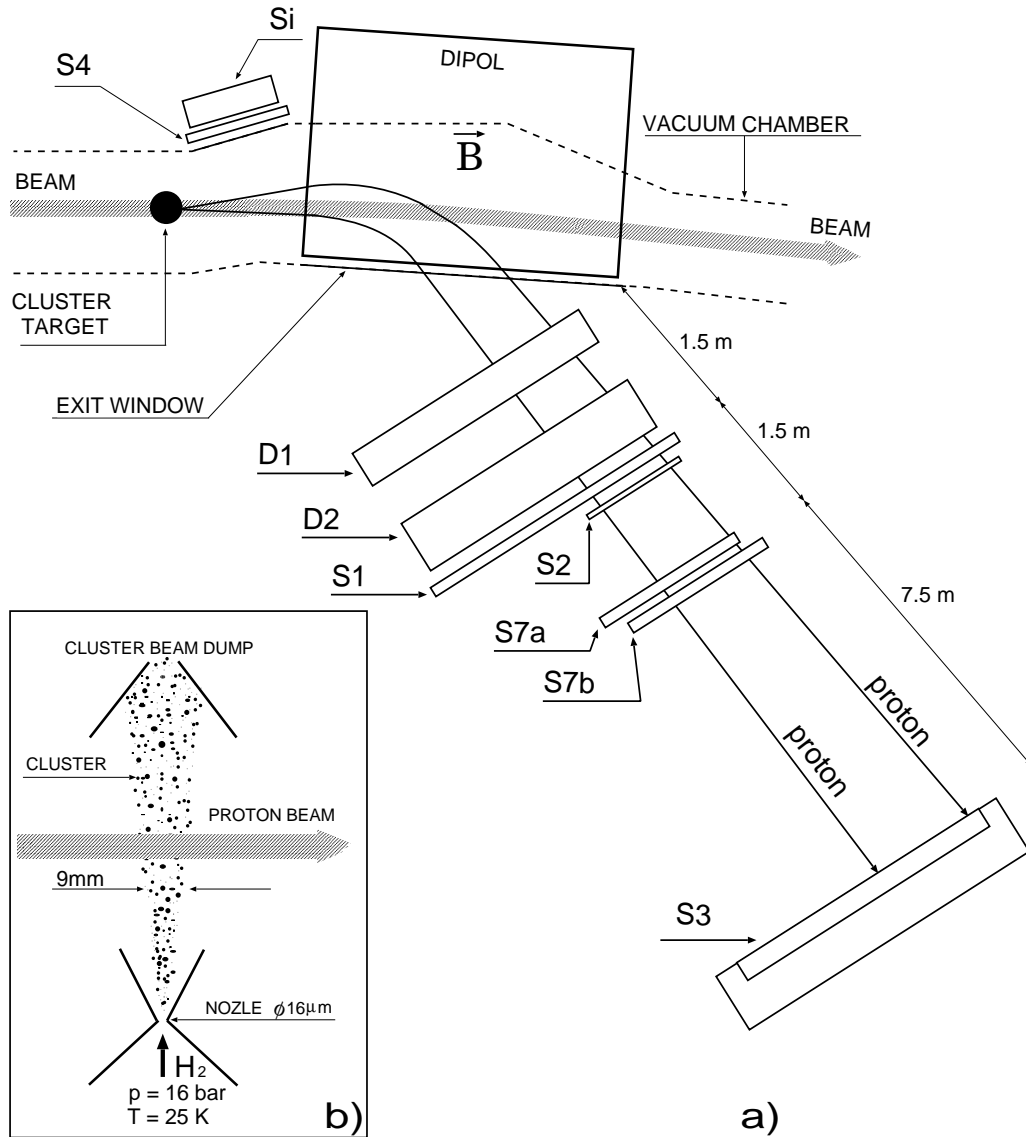


Figure 4.1: a) Schematic view of the COSY-11 detection setup [17]. The cluster target is located in front of the accelerator dipole magnet. Protons from the $pp \rightarrow pp\eta'$ reaction are bent by the magnetic field of the dipole magnet, whereas the beam particles keep circulating in the COSY ring. The decay products of the η' meson are not shown, since the analysis is based on the measurement of the four-momenta of the outgoing protons. Shown tracks indicate the space limits expected for the protons ejected after the $pp \rightarrow pp\eta'$ reaction at a beam momentum of 3.222 MeV/c. The produced protons leave the vacuum chamber through the thin exit foil and are detected: i) in two drift chamber stacks D1, D2, ii) in the scintillator hodoscopes S1, S2, S7, iii) and in the scintillator wall S3.

For the measurement of the elastically scattered protons, additionally, scintillation detector S4 and silicon pad detector Si are used in coincidence with the S1, D1 and D2 detectors.

b) In the left-low corner the schematic view of the cluster target is depicted.

4.2 Beam momenta

The experiment was divided into two periods with different beam tunings. In the first period the beam momentum has been changed continuously during the measurement cycle from $P_{beam} = 3.200 \text{ MeV}/c$ to $P_{beam} = 3.224 \text{ MeV}/c$. Each cycle lasted ten minutes, and the constant growth of the beam momentum amounted to $\frac{\Delta P}{\Delta t} = 40 \frac{\text{KeV}}{\text{c.s}}$. For each event the time past from the beginning of the acceleration cycle was written on tape. Therefore it was possible to analyze each event with the appropriate nominal beam momentum.

Next, the measurement was performed for three discrete nominal beam momenta settings. Namely, two above the η' meson production threshold at: $P_{beam} = 3222 \text{ MeV}/c$ ($13.7 \text{ MeV}/c$ above threshold $\equiv Q \approx 4.4 \text{ MeV}$) and $P_{beam} = 3214 \text{ MeV}/c$ ($5.7 \text{ MeV}/c$ above threshold $\equiv Q \approx 1.8 \text{ MeV}$), and one about $8 \text{ MeV}/c$ below threshold at $P_{beam} = 3201 \text{ MeV}/c$. Q denotes the centre-of-mass excess energy.

In the case of the measurement with a constant beam momentum a special COSY - 11 beam optics [17, 99] was used which minimized the horizontal beam dimension to the width of the cluster target. The influence of beam parameters on the measured particle momenta are discussed in chapter 9.3.

4.3 Principle of the cross section measurement

The simplest observable, characterizing $pp \rightarrow pp\eta'$ reaction, is the *cross section* defined as the $pp \rightarrow pp\eta'$ reaction rate normalized to the target density and to the number of protons passing through the target in the unit of time. The normalizing factor is called *luminosity*³. The cross section for the $pp \rightarrow pp\eta'$ reaction at a given excess energy Q can be expressed as:

$$\sigma(Q) = \frac{N(Q, T)/E_{eff}(Q)}{L(T)} \quad (4.1)$$

where, N denotes the number of η' mesons produced and identified during the time T , E_{eff} gives the detection efficiency, and $L(T)$ stands for the integrated luminosity, which is monitored by the measurement of the elastically scattered protons.

In the following, - after the description of the particular detectors, their calibration and the data evaluation, - the method of establishing N , L , Q and E_{eff} will be presented.

³Taking into account the target density and the beam current (see section 4.1) one can roughly estimate the obtained luminosity to be $l = 5 \cdot 10^{13} \cdot 1.6 \cdot 10^6 \cdot 10^{10} \text{ cm}^{-2}\text{s}^{-1} = 8 \cdot 10^{29} \text{ cm}^{-2}\text{s}^{-1}$ for typical conditions. However, during the measurement it varied within a factor of two.

5. Detection system

5.1 Drift chambers

The chamber stack D1 standing closer to the bending magnet contains six detection planes: two planes with vertical wires and four with inclined wires, whereas the D2 stack contains eight planes as depicted in Figure 5.1a. The wires in consecutive pairs of planes are shifted by half of the cell width in order to resolve the left-right position ambiguity with respect to the sense wire. The drift cells are of the graded field type as shown in Figure 5.1b.

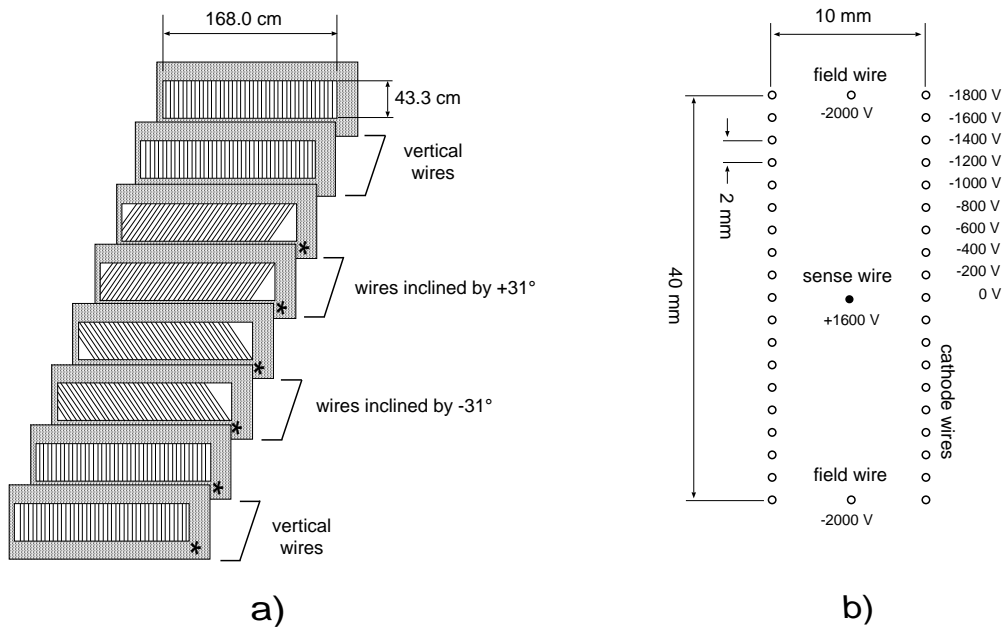


Figure 5.1: (a) Orientation of wires in the drift chamber D2. The smaller drift chamber D1 contains six planes which are indicated by asterisks. (b) Cell structure and voltage distribution. The sense wires are made of $20\mu\text{m}$ thick gold-plated tungsten, and for the field and cathode wires $50\mu\text{m}$ Cu-Be was used. Pictures a) and b) are taken from [17].

A charged particle passing through the drift cell produces ionization of electrons which drift towards the sense wire. The measurement of the drift time ¹

¹The drift time is measured by means of LeCroy multihit TDC 1877 and TDC 1879 modules [100] with the pulses from the drift chamber as a start signal and a trigger pulse as a common stop.

allows the determination of the distance between the sense wire and the particle trajectory. A relationship between the distance X from the sense wire and the drift time, called the time-space calibration ² (see fig. 5.2b), was established from the experimental data. For all measuring periods lasting a few hours each, a new calibration was performed, in order to avoid fluctuations of the drift velocity caused by the atmospheric pressure and the gas mixture changes ³.

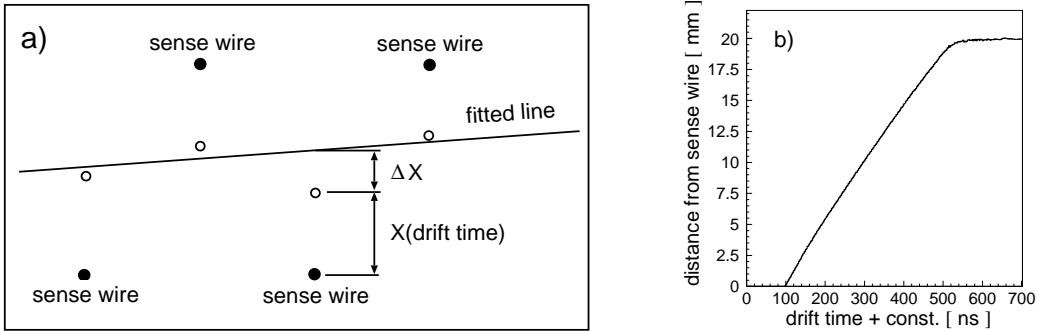


Figure 5.2: (a) Principle of the correction of the time-space calibration. X denotes the distance from the sense wire obtained from the measured drift time applying the time-space calibration. (b) Time-space calibration i.e. relationship between the distance from the sense wire and the drift time.

The calibration was calculated by the series of iterative improvements which were performed in the following way: Having an approximate time-space function ⁴ one calculates distances X of the particle trajectory to the sense wire in each detection plane and fits to the obtained points a straight line. Now assuming that the fitted line corresponds to the real particle trajectory one calculates the deviation (ΔX) between the measured and the fitted distances of tracks from the sense wire as shown in Figure 5.2a. From a sample of experimental data the averaged deviation ΔX_{mean} is established as a function of the drift time (see Figure 5.3a), which is further used for the correction of the time-space relation. Next, the improved time-space function is used for the track reconstruction. The whole procedure is repeated until these corrections are much smaller than the position resolution of the chambers.

The position resolution is obtained from the chi-square distribution of the

²After the correction for the time offsets, the time-space calibration was averaged over all cells within one plane. However, it was performed for each detection plane separately.

³The chambers were operating with a gas mixture of 50% argon and 50% ethane at atmospheric pressure.

⁴The first approximation of the time-space calibration was calculated according to “the uniform irradiation method” described in [101, 102].

deviations ΔX normalized to the number of degrees of freedom defined as follows:

$$\chi^2 = \sum_{i=1}^N \frac{\Delta X_i^2}{\sigma^2} / (N - 4), \quad (5.1)$$

where, N denotes the number of planes which registered a signal, σ denotes the position resolution of the chambers and ΔX is defined in Figure 5.2a. Since, the mean of the normalized chi-square distribution must be equal to unity one can deduce the value of σ , which in this experiment amounted to **0.25 mm (rms)**⁵. Figure 5.3b shows an example of the chi-square distribution obtained with $\sigma = 0.25 \text{ mm}$.

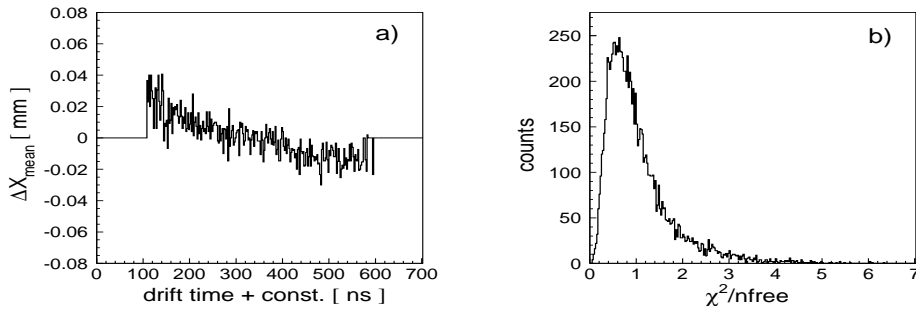


Figure 5.3: (a) Corrections to the time-space relationship. The time-space calibration optimized for one experimental run was used to the data from another run. One observes the change of the drift velocity between these runs. (b) χ^2 distribution defined in equation 5.1.

The registered signals from two particles being too close together may be undistinguishable from the signals produced by one particle. If the distance Δ (see Figure 5.4a) between particles crossing the same cell at the same time is smaller than some minimum value, called the *two-track-resolution* then only one signal will be registered by the corresponding sense wire. Thus, if this happens in many planes simultaneously, the reconstruction of both tracks is impossible and instead of two tracks only one is reconstructed. The reconstruction efficiency, discussed in chapter 9, depends strongly on the two-track-resolution. Therefore the determination of this parameter is crucial for the calculation of the absolute cross section.

In order to estimate the two-track-resolution for a given plane of the drift chamber, a sample of events with two tracks was studied. For each event the distance between the tracks within the studied plane, and the number of real signals in this plane was calculated. Furthermore, for a given distance the ratio of the number of events with two signals to the number of all two track events was computed (see for example Figure 5.4b). For each event with the distance between tracks (in

⁵*rms* stands for root-mean-square value $\equiv \sigma$.

the studied plane) larger than the two-track-resolution at least two signals should be observed. Thus this ratio should be equal to one for distances larger than the two-track-resolution and equal to zero for smaller distances. Figure 5.4b shows that for distances larger than 4 cm, which corresponds to the relevant dimension of the drift chamber cells, this ratio is equal to one. For smaller distances the ratio is about 0.96 and at 0.3 cm drops suddenly to zero. Thus, Figure 5.4b indicates that the two-track-resolution of the studied plane is equal to 3.0 ± 1.0 mm, which agrees with the estimation given in [101]. The same value was obtained for all planes of the drift chambers used in this experiment.

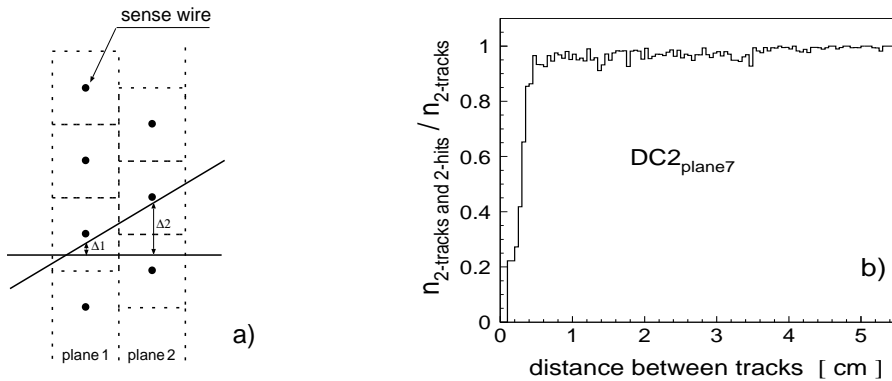


Figure 5.4: (a) A schematic view of two subsequent planes of the drift chamber. If the distance between two tracks in a given plane is smaller than some minimum value, then only one signal will be detected on the sense wire in this plane. (b) The number of events with two tracks and two hits divided by the number of events with two tracks as a function of distance between tracks in the seventh plane of the drift chamber D2.

5.2 Scintillation detectors

5.2.1 S1, S2 and S7 hodoscopes

The scintillation hodoscope S1 consists of sixteen scintillation⁶ modules read out at both sides, via twisted strip light guides, by photomultipliers⁷. The modules with dimensions $45 \times 10 \times 0.4$ cm³, as shown in Figure 5.5a, are arranged vertically with a small overlap (~ 1 mm) in order to avoid “holes” in the geometrical acceptance. For each photomultiplier the integrated charge of the pulse (ADC), as well as the time interval between a common reference timing (trigger signal) and the time of the signal arrival to the TDC⁸ unit was measured.

⁶For all scintillation detectors in the COSY - 11 detection system a Bicron BC 404 ternary scintillator material is used [103].

⁷For the S1, S3, S4 and S7 detectors a Thorn EMI 9954B [104] photomultipliers are used, and the scintillators of the S2 detector are read out by photomultipliers Hamamatsu R 1635-02 [105].

⁸TDC — time to digital converter. The COSY - 11 experiment make use of a FASTBUS crate equipped with LeCroy ADC 1881 and TDC 1875A [100] for the signals from scintillators.

The sum of the signals charge from the upper and the lower photomultipliers for monoenergetic particles is approximately constant, to an accuracy of about 10%, independently of the impact position [106]. Therefore the energy loss was calculated as being proportional to this sum. The resolution of the energy loss measurement for all scintillation detectors is about 20%, see Figures 9.5 in chapter 9.6.

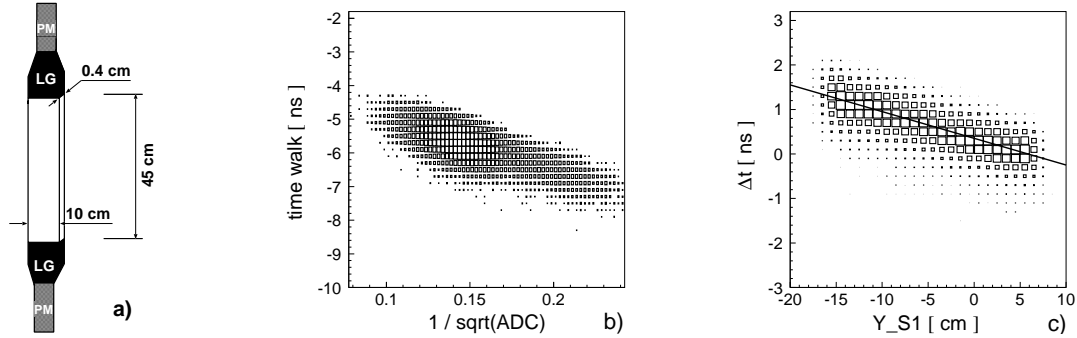


Figure 5.5: (a) Schematic view of a separate scintillation segment of the S1 detector. LG stands for light guide and PM for photomultiplier. (b) An example of the time walk effect for the upper part of one module of the S1 detector. $\frac{1}{\sqrt{ADC}}$ is given in arbitrary units. The time walk values are negative because of the still wrong time offsets at this stage of the analysis (see next section). (c) The velocity of the light signal in the S1 scintillator. The same time difference as in b), but after a time walk correction, versus the vertical position in the S1 detector.

Since signals were discriminated by the leading edge discriminators [107] the registered time varied with the signal amplitude. This effect, referred to as a *time walk* was corrected assuming a linear dependence between the time walk and the inverse of the square root of the signal charge $\frac{1}{\sqrt{ADC}}$ [108]. In order to measure the time walk, the time-of-flight between the S1 and the S3 counters was compared with a time-of-flight deduced from the reconstructed particle momentum⁹, and plotted as a function of $\frac{1}{\sqrt{ADC}}$ as shown in Figure 5.5b. For the time walk correction, only events with a certain constant distance between the hit position and the scintillator edge were taken into account. This allowed to avoid the biasing caused by the time dependence on the impact position. Parameters of a straight line fitted to the points of the scatter plot were used in the data analysis for the time walk correction, which was performed for each photomultiplier (discriminator channel) separately.

After the reduction of the time walk the velocity of the light pulse in the scintillator was calculated for each detection segment. Again the difference between

ADC stands for charge to digital converter.

⁹The momentum reconstruction was performed by the back-tracking of the (measured by the drift chambers) particle trajectory to the target point.

time-of-flights calculated by two different methods were studied as a function of the vertical hit position in the S1 scintillator as depicted in Figure 5.5c. The velocity was calculated for each segment separately. The obtained values oscillate around $16.0 \pm 0.5 \text{ cm/ns}$.

The start time for the time-of-flight was calculated as a weighted mean of times measured by the upper and lower photomultiplier. The weights were computed as the inverse of the squared time resolution ($w = \frac{1}{\sigma^2}$), which changes¹⁰ with the distance between the hit position of the counter and the photomultiplier.

Similar calculations were performed for each of the S2 and S7 detection segments. The S2 detector, in the same way as S1, consists of sixteen scintillation modules with dimensions of $45 \times 1.3 \times 0.2 \text{ cm}^3$, and the S7 is built out of eight segments each with dimensions of $100 \times 10 \times 0.4 \text{ cm}^3$ positioned in two rows as depicted in Figure 4.1.

5.2.2 S3 detector and the time-of-flight calibration

The S3 detector delivers the stop signal for the time-of-flight measurement. It consists of a large area non-segmented scintillation wall of dimensions $220 \times 100 \times 5 \text{ cm}^3$ viewed by a matrix arrangement of 217 photomultipliers [109, 110, 17] as shown schematically in Figure 5.6.

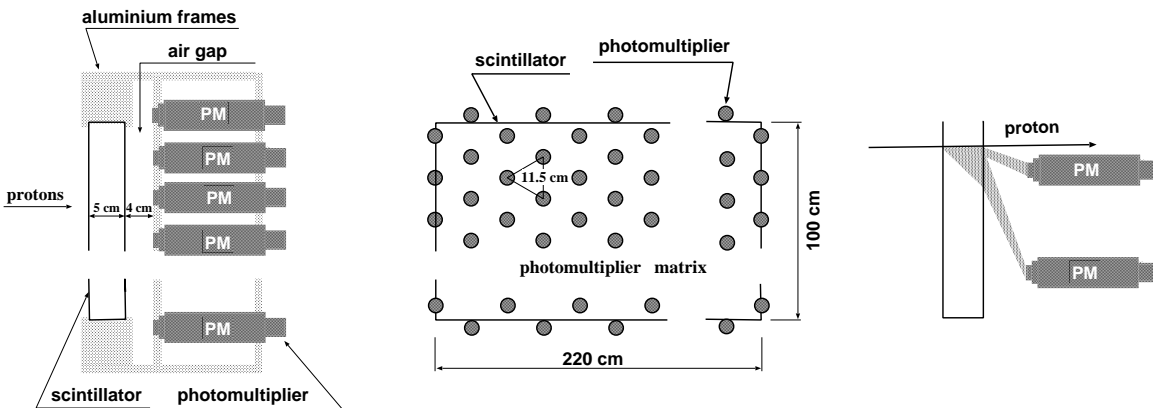


Figure 5.6: Schematic view of the S3 scintillation detector. A side view (left part). The photomultiplier matrix together with the dimensions of the scintillation wall (middle part). Principle of the light collection (right part).

An impinging charged particle passing through the scintillator produces a scintillation light (see Figure 5.6). The amount of light registered by a given photomultiplier decreases rapidly with increasing distance to the particle's impact position. Therefore, only a few photomultipliers register enough light to produce a signal

¹⁰The changes of the time resolution with the hit position of the counter were minimized because the edges of the scintillator were not used as seen in Figure 5.5c. Note that the scintillator covers values of Y_{s1} from -22.5 cm to 22.5 cm .

higher than the discriminator threshold. This feature allows for the identification of the number of registered particles and for the assignment which photomultiplier belongs to which particle. For brevity the group of the photomultipliers assigned to one particle will be called *cluster*.

Using the signal charge distribution among photomultipliers one can not resolve two particle tracks if they are closer than 11 *cm*. Such cases can be resolved, however, provided that the difference between impact times for registered particles is significantly larger than the time resolution.

A signal charge given by a photomultiplier depends on the particle energy loss, distance between the hit position and the photomultiplier, and on the photomultiplier gain. Figure 5.7a shows the dependence between the signal charge and the distance between the photomultiplier and the particle hit position. Having this dependence and knowing the photomultiplier gain one can calculate the energy loss from each photomultiplier and takes the average as the result. Alternatively, the particle energy deposition can be derived as being proportional to the sum of the ADC values from photomultipliers of an appropriate cluster.

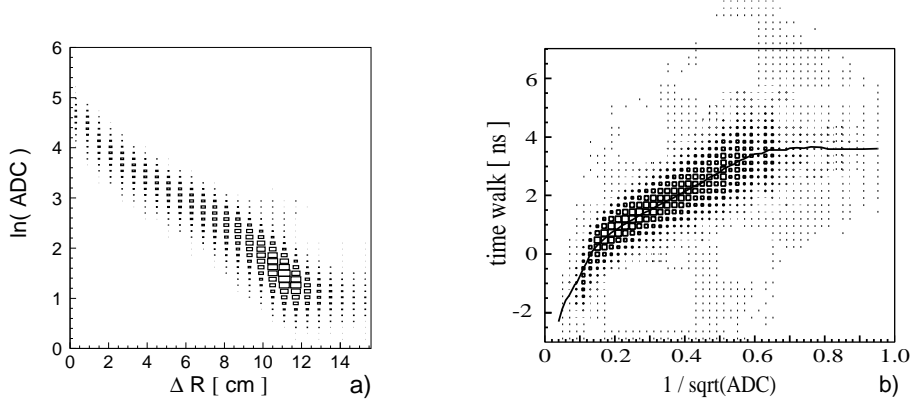


Figure 5.7: (a) A natural logarithm of the ADC value normalized to the path length in the scintillator, in arbitrary units, as a function of a distance between the photomultiplier and the position where particle crossed the scintillation wall. The picture was done for protons with velocities in the range of $[0.73 \cdot c : 0.77 \cdot c]$. (b) Time walk effect in the S3 detector. Difference between TOF measured between S1 detector and a chosen photomultiplier in the S3 detector and TOF calculated from the reconstructed particle momentum as a function of the inverse of the square root of the signal charge ($\frac{1}{\sqrt{ADC}}$) in the studied photomultiplier. The line shows the mean time walk values calculated for each ADC channel, $\frac{1}{\sqrt{ADC}}$ is given in arbitrary units.

The hit position is calculated as the centre-of-gravity of the pulse charges of the photomultipliers from an appropriate cluster. The position resolution obtained in the present experiment amounts to 1.5 *cm* (*rms*) as long as the particles are not closer than 11 *cm*.

The stop of the time-of-flight measurement is calculated, for each cluster separately, as the weighted average of times obtained from the participating photomul-

tipliers. The signal time from each photomultiplier is corrected for the time walk effect and the time needed by the light signal to arrive at the photomultiplier. The dependence of the time walk on the inverse of the square root of the signal charge ($\frac{1}{\sqrt{ADC}}$) is not linear in the whole range of the ADC values ¹¹, see Figure 5.7b. Therefore, unlike in the S1 case, the correction was done by calculating the mean time walk for each ADC value, as given by the line in Figure 5.7b. This figure shows also that the time resolution changes with the signal amplitude. That is why, the appropriate weights - depending on the charge of the signal - were used for the calculation of the mean time in the cluster.

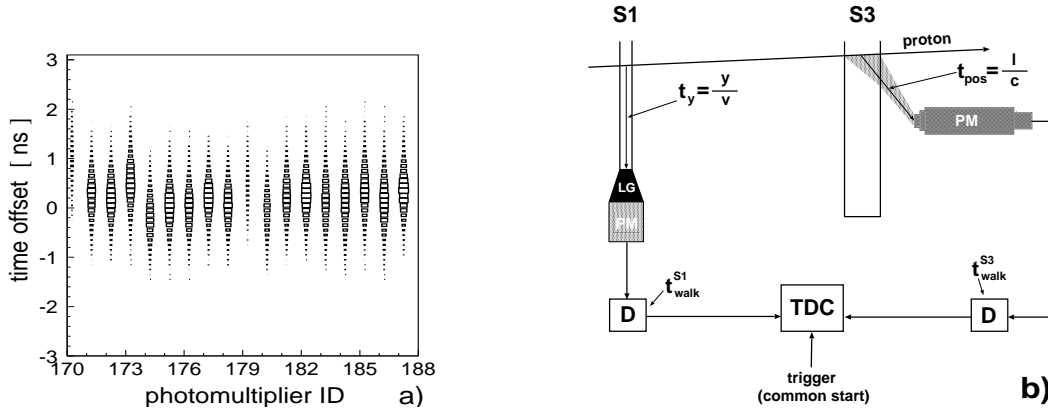


Figure 5.8: (a) The same time difference as in Figure 5.7b, but after the time walk correction, versus a photomultiplier ID of the S3 scintillator. The picture shows offsets only for two columns of photomultipliers. Note that the photomultipliers with numbers 170 and 179 have registered essentially less events than others. This is because they are positioned at the upper and lower scintillator edge (see Figure 5.6). (b) Principle of the time-of-flight measurement between the S1 and S3 scintillation counters. “D” stands for discriminator.

In order to obtain the absolute values of the time-of-flight it is necessary to adjust relative time offsets among all photomultipliers within each scintillation detector as well as the relative offsets between different detectors. Denoting the real time when a particle crosses the S1 detector by t_{s1} and similarly t_{s3} for the S3 detector the time-of-flight reads: $tof = t_{s3} - t_{s1}$. Figure 5.8b depicts schematically the principle of the time-of-flight measurement. According to this figure the experimental TDC values can be expressed as:

$$\begin{aligned}
 TDC_{s1} &= t_{s1} + t_y(y) + t_{walk}^{s1}(PM) + t_{offset}^{s1}(PM) - t_{trigger} \\
 TDC_{s3} &= t_{s3} + t_{pos}(l) + t_{walk}^{s3}(PM) + t_{offset}^{s3}(PM) - t_{trigger}
 \end{aligned}
 \tag{5.2}$$

¹¹Note that here the range of the ADC values is much broader than in the case of the S1 counter, compare Figure 5.5b, and also that for the S3 detectors other leading edge discriminator modules are used [17].

where l denotes the distance between the hit position and the photomultiplier in the S3 detector and y stands for the distance between the cross point in the S1 counter and the scintillator edge closer to the photomultiplier.

In both of the equations 5.2 $t_{trigger}$ is identical and thus is unimportant in the calculation of the tof value. The only unknown quantities, are the time offsets t_{offset} , which for the S3 detector, for example, can be extracted by comparing the tof values with the time-of-flight calculated from the reconstructed particle momentum. Of course, at least the approximate t_{offset} values of the S1 detector have to be known. Iteratively, using the obtained time offsets for the S3 detector one can calculate the S1 offsets. After repeating this procedure a few times offset values for both detectors are obtained. Figure 5.8a shows the time offsets for some photomultipliers of the S3 counter after the third series of improvements.

With the parameters for the time walk, the light pulse velocity in the scintillators, and all time offsets, one can calculate the $tof = t_{s3} - t_{s1}$ applying equations 5.2. However, in the analysis t_{s1} was taken as a weighted average of times obtained from upper and lower photomultipliers of the S1 module, and t_{s3} as a weighted mean of times from an appropriate photomultipliers cluster of the S3 detector.

For events with more than one registered particle the segments of the S1 detector were assigned to the corresponding cluster in the S3 counter, using the particle trajectory obtained from the drift chamber.

The same way as described for the S1 detector, the time-of-flight was also calculated using the start time from signals of the S2 or S7 detectors.

For events with more than one registered particle, only those detectors (S1, S2, S7) were taken into account in which each particle was registered in a different segment. If both particles crossed only one segment in each detector than the averaged value was taken.

The overall obtained time-of-flight resolution amounts to **330 ps** (*rms*) for events with two or more particles.

5.3 Silicon detector

The silicon pad detector together with the S4 scintillation counter is used for the detection of the recoil protons from the proton-proton elastic scattering. The silicon detector [111, 17] consists of 144 pads with dimensions of $22.0 \times 4.5 \times 0.28 \text{ mm}^3$ arranged as depicted in Figure 5.9. Each pad is read out separately. The detector granularity allows the determination of the scattering angle for the recoil protons with an accuracy of $\pm 0.5^\circ$.

In Figure 5.10a the ADC spectrum integrated over all pads is shown. Already in the histogram of the raw data clear signals from the minimum ionizing pions and elastically scattered protons are visibly separated from the noise signals. In the analysis only pads having ADC signal larger than seven were considered.

However, as can be seen in Figure 5.10c, this requirement did not caused losses of the data.

Using events identified as a proton-proton elastic scattering reaction the relative amplification of single pads was checked. Figure 5.10b shows the measured energy loss divided by the energy loss expected from the dE/dx signal of the proton at a given scattering angle. The amplifications from all channels were found to be the same within a few per cent.

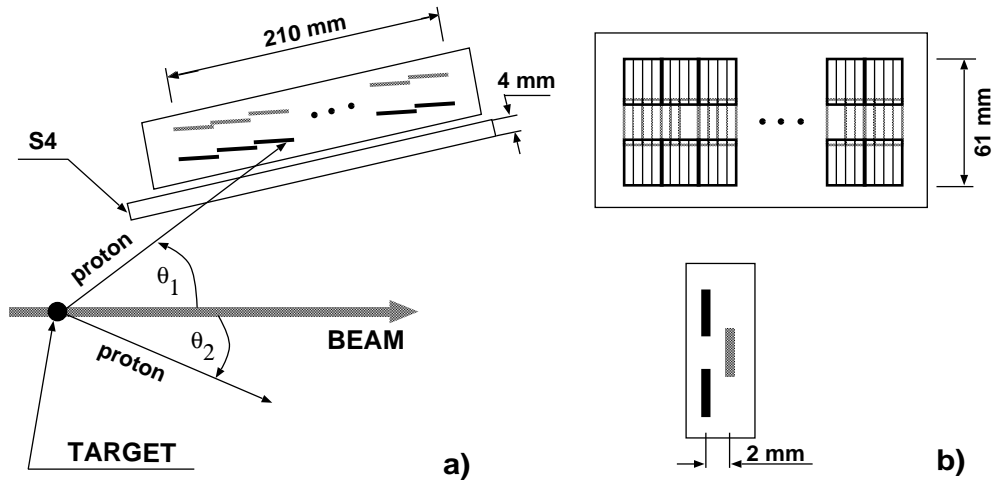


Figure 5.9: (a) Top view of the silicon pad detector (compare Figure 4.1). Each element contains four separate pads with dimensions $22. \times 4.5 \times 0.28 \text{ mm}^3$. The overlap between the detection elements allows to avoid insensitive areas. (b) Silicon pad detector as seen from the target point (above). Side view (below).

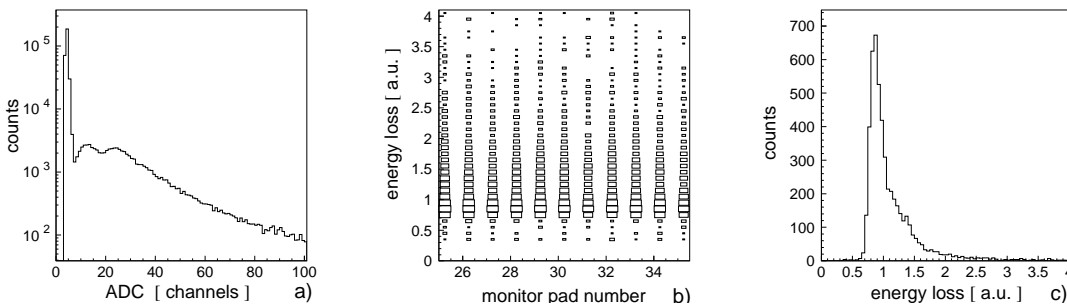


Figure 5.10: (a) Charge (ADC) spectrum from the silicon detector, integrated over all pads. (b) Energy loss measured by means of the silicon pad detector, for the elastically scattered protons, as a function of the pad number. Only ten pads from the middle row of the detector are shown. (c) The normalized energy loss integrated over all pads for the elastically scattered protons. In the analysis it was required that the energy loss must be larger than 0.3 in the units from the picture which corresponds to the ADC value of 7. One observes that this demand has negligible influence on the efficiency.

6. Data evaluation

6.1 Data acquisition

For each signal from the scintillation detectors both the charge and the time relative to the trigger pulse as well as the time signals from the drift chambers were converted from analog to digital form by FASTBUS modules [100]. The signals from the silicon detector were digitalized by means of CAMAC units. The general control of the data stream was carried out by an *event-builder* processor [112], which collects the data from FUSTBUS and CAMAC controllers and sends them to the EXABYTE [113] device which writes them on the 8 *mm* magnetic tape. Part of the data stream was sent, parallel, to the ALPHA station, from where the experiment was controlled and the on-line analysis was possible.

A detailed description of all issues connected with the data acquisition system can be found in references [114, 115, 17, 116].

The dead time of the data acquisition system, corresponding to the registration of one event, amounted on the average to 1 *ms* [114]. This caused, with the typical trigger rate of hundred events per second, that about five per cent of events were not accepted. However, since the studied $pp \rightarrow pp\eta'$ reaction was measured simultaneously with the proton-proton elastic scattering used for the luminosity determination, it was not necessary to monitor precisely the dead time.

6.2 Trigger logic - hardware event selection

The $pp \rightarrow pp\eta'$ reaction is identified through the measurement of the four-momentum vector of the outgoing protons. The very first requirement was, that at least two charge particles were detected which was done using the signals from the scintillation detectors only. The scheme of the trigger logic used for this purpose is shown in Figure 6.1. A distinction between proton and pion was left for the off-line analysis.

For simplicity we only consider the S1 and the S3 detectors. One can differentiate two cases which are taken into account: i) both particles impinge the S3 detector and cross different segments in the S1 detector and ii) both particles impinge the S3 detector but are registered in the same segment of the S1 counter. In the first case the multiplicity of the S1 segments is larger than one, and the number of the photomultipliers giving signals in the S3 detector should be larger than two. This is realized by the trigger $T_{s1,\mu>1} \wedge T_{s3,\mu>2}$ (see Figure 6.1). In the second case, realized by the trigger $T_{s1,high} \wedge T_{s3,\mu>2}$, when two protons cross the same segment of the S1, on the average two times larger energy deposition

is expected in this segment and therefore only events with the appropriate high amplitude will be accepted.

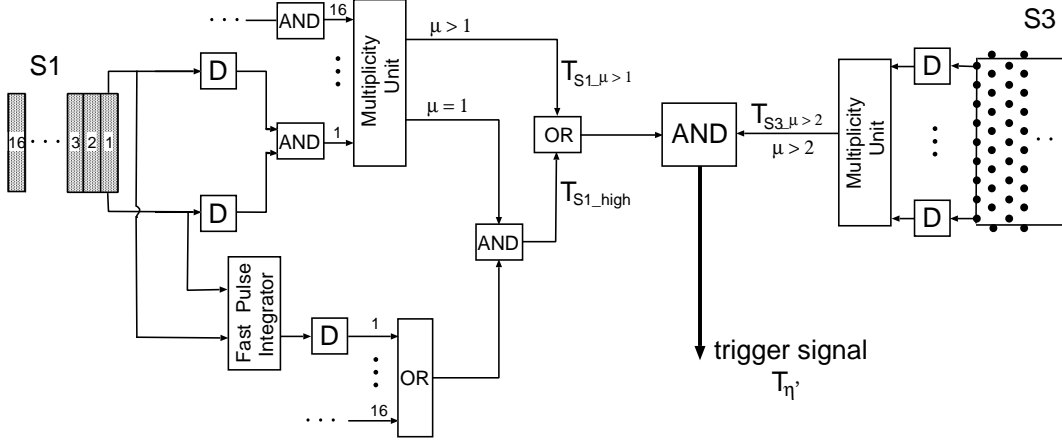


Figure 6.1: Simplified scheme of the trigger electronics for the detection of two outgoing charge particles. The S2 detector, not shown here, is connected identically as the S1 counter. In the case of the S1 detector the multiplicity unit defines the number of segments which have a signal, and in the case of the S3 detector the number of active photomultipliers is determined. For more details of the trigger electronics see [114, 117].

Special *fast-pulse-integrator* [118] units, which add the signals from the lower and upper photomultipliers, deliver analog pulses to the discriminators with amplitudes proportional to the energy loss¹. Using appropriate discriminator levels, only such signals which corresponds to the energy loss larger than the demanded minimum were accepted.

Since the energy deposition depends on the particle velocity, this threshold value had to be adjusted for signal amplitudes of protons from the $pp \rightarrow pp\eta'$ reaction, which have the velocity of about $0.75 c$. Figure 6.2a shows the spectrum of the energy loss in the S1 counter in the case when only one particle is registered. The shaded histogram shows the energy loss distribution corresponding to protons with velocities ranging from $0.7 c$ to $0.8 c$. Setting the hardware threshold to ninety most of the events with one particle crossing the segment are rejected, but still most of the events, where two protons with velocity $0.75 c$ cross the same segment simultaneously are registered. Figure 6.2b shows an energy loss spectrum from the raw data taken with the trigger $T_{\eta'}$ used in the experiment. Two peaks at the same positions as in Figure 6.2a are due to the trigger with multiplicity larger than one, and the sharp edge at 90 (energy loss in a.u.) comes from the “high amplitude” threshold.

¹The hardware summation of signals required an adjustment of the same amplifications for the lower and upper photomultiplier.

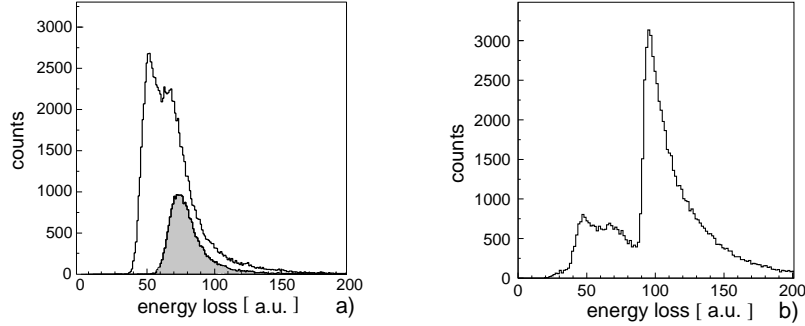


Figure 6.2: (a) Energy loss distribution in a segment of the S1 detector measured with a test trigger ($T_{s1,\mu=1} \wedge T_{s3,\mu>2}$). Values on the horizontal-axis correspond to the sum of the ADC values from upper and lower photomultiplier. Two peaks originate from pions and protons. The shaded histogram corresponds to protons with the velocity in the range between $0.7c$ and $0.8c$. Producing this spectrum exactly one track in the drift chambers was required. (b) Energy loss distribution in a segment of the S1 detector obtained with the $T_{\eta'}$ trigger. If the trigger is released by the S2 detector or two particles cross separate segments in the S1 then, in each segment separately, the same structure as in a) is observed. However, if only one segment has a signal, then it is required (by the electronics - compare Figure 6.1) that the sum of the pulse charges from the upper and the lower readout must be larger than the threshold value, which is in this case equal to ninety.

The S2 detector, having segments about seven times narrower than S1, was additionally used in the trigger in the same way as the S1 detector. Thus summarizing, the main trigger for the detection of the $pp \rightarrow pp\eta'$ reads:

$$T_{\eta'} = (T_{s1,\mu>1} \vee T_{s1,high} \vee T_{s2,\mu>1} \vee T_{s2,high}) \wedge T_{s3,\mu>2} \quad (6.1)$$

In order to verify the influence of the threshold settings on the trigger efficiency two histograms, shown in Figure 6.3, were built. Figure 6.3a showing the energy loss distribution for two protons with velocities of $0.75c$, indicates that the adjusted threshold, equal to ninety, was low enough to neglect the number of rejected events. Similarly, one can conclude from Figure 6.3b that the number of events with the multiplicity lower than three in the S3 detector is to be neglected.

Another branch of electronics was prepared for the selection of events with elastically scattered protons. The corresponding trigger T_{pp} required the coincidence between signals from the S4 and the S1 scintillation detectors. However, because of the high rate only every eighth T_{pp} trigger signal was accepted.

The efficiency of the T_{pp} trigger depends directly on the efficiency of the S1 detector, which was found to be larger than 99.99% [106] and on the S4 detector. In order to verify the efficiency of the S4 detector, which was working in the fringe

magnetic field of the dipole, additionally every 256'th event triggered by the S1 detector alone was registered. The efficiency of the S4 counter was found to be 99.9%

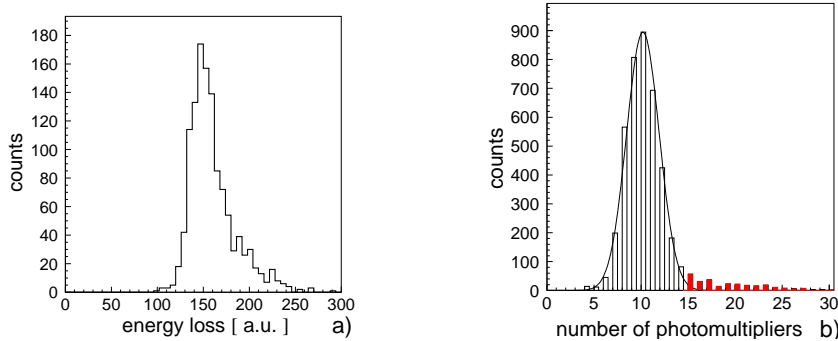


Figure 6.3: (a) Energy loss distribution measured in a segment of the S1 detector obtained for events with two protons having velocities in the range between $0.7 c$ and $0.8 c$, both crossing through the same segment. Units on the horizontal-axis are the same as in Figures 6.2a and 6.2b. (b) Number of photomultipliers (multiplicity) giving signals in the S3 detector, for two protons with velocities in the range between $0.7 c$ and $0.8 c$ crossing the scintillation wall. The line shows the Gaussian distribution fitted to the data. The shaded tail corresponds to events when at least one proton made a nuclear reaction in the scintillator.

The information which trigger opened the data acquisition was written on tape. This was necessary for the calculation of the absolute number of events with elastically scattered protons since such event could also release the $T_{\eta'}$ trigger which, opposite to the T_{pp} trigger, was not prescaled.

6.3 Off-line analysis - software event selection

In the following the evaluation of the data from the $T_{\eta'}$ trigger is presented. The selection of events from the elastically scattered protons will be discussed in chapter 7.

The $T_{\eta'}$ trigger was adjusted in such a way that all events with two or more charge particles were registered². However, if only one particle cross the detectors it could also release the $T_{\eta'}$ trigger, provided that the energy deposited in the S1 or S2 segment was larger than the “high amplitude” threshold. Thus, in the first step of the off-line data analysis, events with two or more tracks in the drift chamber were preselected.

A particle trajectory in the drift chambers was reconstructed by fitting a straight line to the measured cross points in all planes. In case of many tracks, the

²Of course this concerns only the geometrical region in which protons from the $pp \rightarrow pp\eta'$ reaction were expected.

correlation between hit-point and track must be decided. In short, one can say that all possibilities were checked and the one with the smallest chi-square was accepted³. Since for the track reconstruction it was required that each fitted track has at least twelve hits, the fast preselection was performed by rejecting all events which have less than 24 hits in drift chambers. This criterion allowed to reject about 85% of the data, see Figure 6.4a. However, performing the reconstruction with this condition about 6% of the events with two tracks were lost. This and other aspects of the reconstruction efficiency are discussed in chapter 9.5.

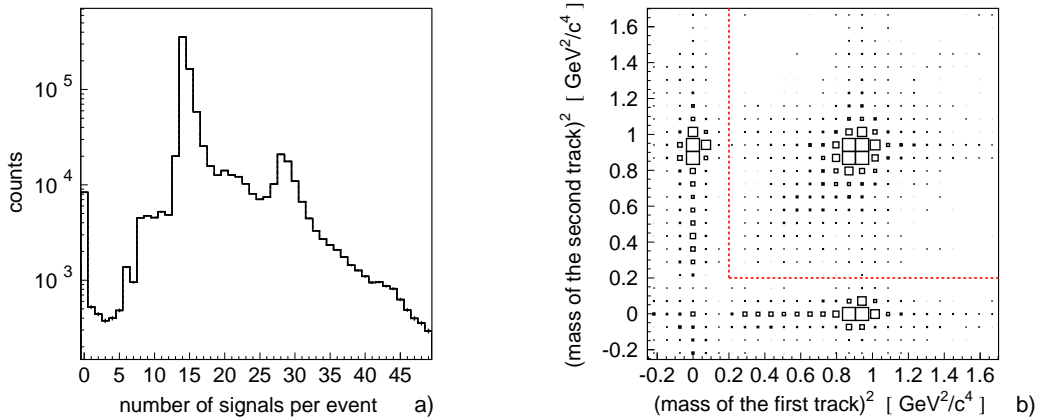


Figure 6.4: (a) Number of signals from drift chambers per event. A sample of data from a six hours measurement is shown. The D1 and D2 drift chambers have together fourteen planes. Thus, peaks with maxima at 14 and 28 number of signals per event correspond to one and two particles crossing the chambers, respectively. The enhancement at 42 corresponds to three particles. A small peak at 6 originates from one particle which passed through the insensitive area in the planes with inclined wires (compare Figure 5.1). Similarly, an enhancement at 20 corresponds to two particles from which one passed through this area. The peak in zero appears because the trigger detector S1 is larger than the drift chamber active area. (b) Squared masses of two particles measured in coincidence. The pronounced peak close to the centre of the figure corresponds to two registered protons. Peaks are recognized also when proton and pion or two pions were detected.

Knowing the trajectory of each particle in the drift chambers it was possible to compute the particle momentum and its velocity. The particle velocity was calculated from the time of flight measured between the scintillation hodoscopes S1, S2, S7 and the scintillation wall S3. The particle momentum were computed by the “back tracking” in the magnetic field to the target point. It was performed as follows: taking the approximate momentum, the particle trajectory in the three dimensional dipole magnetic field [119, 120] was reconstructed and the distance

³for more details about the track reconstruction see [102] or contact Mariusz Sokółowski msokolo@if.uj.edu.pl

between this trajectory and the target was calculated. Next the momentum was varied as long as the trajectory crossed the target. However, in the computations only horizontal coordinates of the target point were fixed, and thus the distribution of the vertical component of the reaction point could be obtained from the data. For the first iteration, the approximate value of the momentum was calculated assuming that the dipole field is constant and has only a vertical component [121].

Figure 6.4b shows the squared mass of two simultaneously detected particles. The masses were calculated from the momentum and the velocity established for each trajectory. A clear separation into groups of events with two protons, proton and pion or two pions is seen. The dashed line indicates a software cut for the selection of events with two registered protons, which were accepted for the further analysis.

Events with three reconstructed tracks were also analyzed, since the charged pion from the η' decay may also give signals in the drift chambers. In such cases, two out of three registered particles must have been identified as a proton.

6.4 $pp \rightarrow pp\eta'$ reaction identification

After the selection of events with two outgoing protons the possible η' meson was not identified directly but its four-momentum vector was determined via the missing mass techniques⁴. The knowledge of the momenta of both protons before and after the reaction, and the energy and momentum conservation, allow to calculate a mass of a not observed particle or system of particles in the exit channel. Namely:

$$m_x^2 = E_x^2 - \vec{P}_x^2 = (E_{beam} + E_{target} - E_1^{proton} - E_2^{proton})^2 - (\vec{P}_{beam} - \vec{P}_1^{proton} - \vec{P}_2^{proton})^2 \quad (6.2)$$

Figure 6.5a shows a histogram of the missing mass obtained from the measurement below the η' production threshold (solid line). This spectrum does not contain any statistically significant structure and especially there is no enhancement in the region corresponding to the η' meson mass. In order to reduce the statistical fluctuations the histogram was smoothed out as indicated by the dashed line. The smoothed representation of these data is used in the following as a background to the $pp \rightarrow pp\eta'$ reaction.

The shape of the background can well be reproduced by Monte Carlo simulations taking a multi-pion production into account. Figure 6.5b compares the experimental yield of the $pp \rightarrow ppX$ reaction measured below the η' threshold to the missing mass spectrum obtained from a simulation of the $pp \rightarrow pp\pi^+\pi^-$ and $pp \rightarrow pp\pi^0\pi^+\pi^-$ reactions (dashed line).

⁴The missing mass techniques is described in [122], and was first applied by [123].

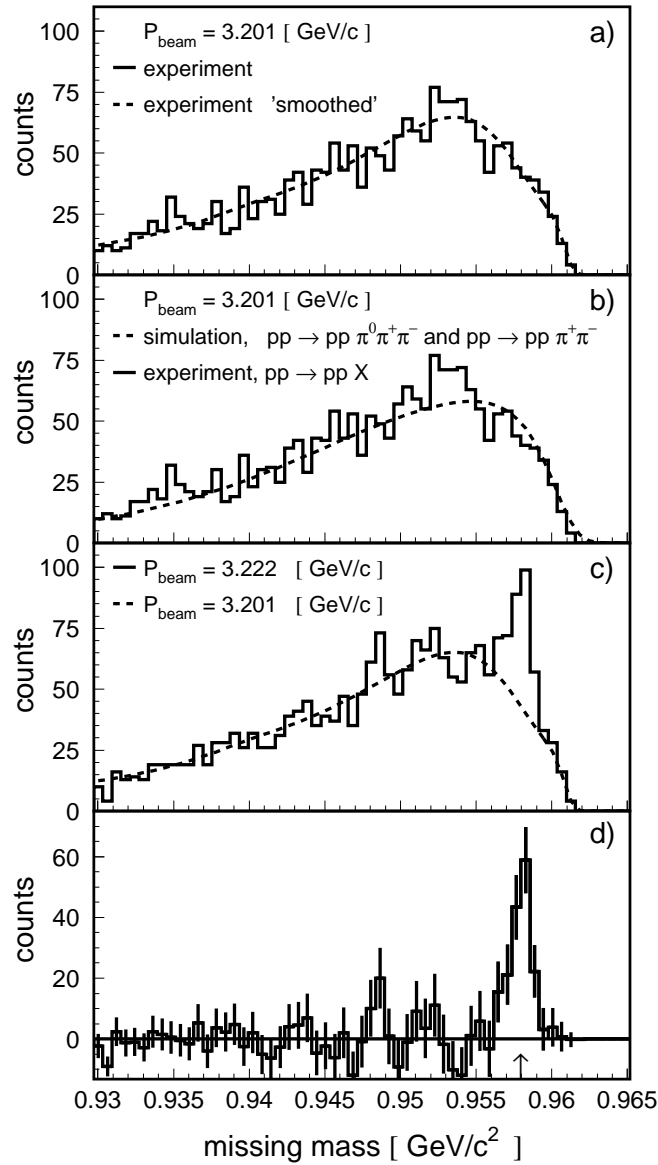


Figure 6.5: Missing mass of the unobserved particle or system of particles in the $pp \rightarrow ppX$ reaction.

(a) Missing mass spectrum measured at a nominal beam momentum of 3201 MeV/c which is about 7 MeV/c below the $pp \rightarrow pp\eta'$ reaction threshold (solid line). The spectrum is shifted towards higher masses to the kinematical limit of the beam momentum of 3222 MeV/c. Smoothed fit function to the data (dashed line). (b) The solid line is the same as in a). The dashed line represents the missing mass distribution obtained from a Monte Carlo simulation of the $pp \rightarrow pp\pi^+\pi^-$ and $pp \rightarrow pp\pi^0\pi^+\pi^-$ reactions. (c) Data at a nominal beam momentum of 3222 MeV/c (~ 14 MeV/c above the $pp \rightarrow pp\eta'$ reaction threshold) - solid line. Scaled background from a) - dashed line. (d) Difference between solid and dashed line of c), the arrow indicates the η' meson mass.

Since the angular distributions for the two or three pion production is not known the simulations were performed considering the phase space factors only. The result of this Monte Carlo simulation is not used in the analysis, it is presented here only to show that the form of the background is well understood.

It is worth noting that not only the shape but also the absolute number of background events (amounting to ~ 2050) agrees fairly well with the yield calculated from the total cross section for the two and three pion production which is found to be ~ 2800 ⁵.

At the present value of the beam momentum up to seven pions could be produced in the proton-proton scattering, however, due to the decreasing cross section with increasing number of pions these reactions do not contribute significantly⁶.

Figure 6.5c shows the missing mass spectrum from the measurement at the nominal beam momentum of $3222 \text{ MeV}/c$ together with the smoothed representation of the data taken below threshold. Subtracting both reaction yields from each other (above threshold minus below threshold), after normalization to the integrated luminosity, one obtains a clear peak in the region corresponding to the η' meson mass, as seen in Figure 6.5d. The small seemingly structure at missing mass values below the η' mass is not significant from statistical point of view and it does not reproduce itself for measurements at the other beam momenta.

For the subtraction the spectrum from below threshold was shifted in such a way that the kinematical limits for both histograms are the same. Since the background is mainly due to two or three pion production the form of its missing mass distribution remains the same for the measurements at the beam momenta of $3201 \text{ MeV}/c$ and $3222 \text{ MeV}/c$. This is because, this momentum variation corresponds to only about one per cent change of the momentum above threshold for the $pp \rightarrow pp\pi^+\pi^-$ or $pp \rightarrow pp\pi^0\pi^+\pi^-$ reactions. For example, the threshold beam momentum for the $pp \rightarrow pp\pi^+\pi^-$ reaction amounts to $1219 \text{ MeV}/c$.

Integration of the entries in the peak from Figure 6.5d gives the number of registered events for the production of the η' meson in the $pp \rightarrow pp\eta'$ reaction, which was denoted as “N” in the equation 4.1, and which in this case amounts to $N = 164.3 \pm 23.4$.

Table 6.1 presents the number of $pp \rightarrow pp\eta'$ events obtained for various beam momenta. A first column indicates the used beam optics, where the name COSY-11 stands for the standard beam tuning used in the COSY-11 experiments [17, 99], and *ramping* denotes the beam optics used in the measurements with the

⁵The total cross section at a beam momentum of $3200 \text{ MeV}/c$ for the $pp \rightarrow pp2\pi$ is equal to $\sigma \approx 3.4 \text{ mb}$ and for $pp \rightarrow pp3\pi$ $\sigma \approx 0.6 \text{ mb}$ [124]. The detection efficiency amounts to $0.7 \cdot 10^{-5}$ and $3.7 \cdot 10^{-5}$ for two and three pion production, correspondingly. The integrated luminosity was equal to 60.9 nb^{-1} (see table 7.1 in chapter 7). Hence, the expected number of registered events amounts to ~ 2800 .

⁶The cross section goes down with the number of produced particles, additionally the available phase space decreases drastically nearly as $(Q/\sqrt{s})^{(3n-5)/2}$ [6, 122], where Q and s denote the excess energy and the total energy in the centre-of-mass system, respectively, and n stands for the number of particles in the exit channel.

continuous beam momentum change.

For measurements with the continuous beam momentum increase each event was analyzed with an appropriate beam momentum and only the missing mass spectrum was grouped into bins corresponding to the beam momentum range of $4 \text{ MeV}/c$.

beam optics	nominal beam momentum P_{beam} [MeV/c]	nominal excess energy Q [MeV]	number of registered $pp \rightarrow pp\eta'$ events
COSY-11	3222	4.4	164.3 ± 23.4
COSY-11	3214	1.8	70.7 ± 14.4
ramping	$3220 \rightarrow 3224 ; \overline{3222}$	4.4	43.6 ± 11.0
ramping	$3216 \rightarrow 3220 ; \overline{3218}$	3.1	20.5 ± 8.0
ramping	$3212 \rightarrow 3216 ; \overline{3214}$	1.8	3.0 ± 5.5
ramping	$3208 \rightarrow 3212 ; \overline{3210}$	0.5	-1.5 ± 5.0

Table 6.1: Number of identified $pp \rightarrow pp\eta'$ reactions

A seemingly inconsistency of the number of registered $pp \rightarrow pp\eta'$ events at an excess energy of $Q = 1.8 \text{ MeV}$ for different beam optics will be explained later in chapter 8, where the true beam momentum shall be established on the basis of the experimental data. But first, in the next chapter, the method of calculating the luminosity “L” shall be presented.

proton, which is bent in the magnetic field of the dipole and registered in the drift chambers, one can determine a momentum vector at the target point. According to two body kinematics [122, 126] the parallel and perpendicular to the beam momentum components of this momentum vector should form an ellipse. Figure 7.2a shows the appropriate part of the kinematical ellipse together with the experimental data gathered with the trigger T_{pp} , which demanded simultaneous signals in the S1 and the S4 scintillators. Already, a sample of the raw data gives a clear peak at the expected kinematical line. The boundary of the region filled with the data in Figure 7.2a is determined by the detection acceptance. If the value of the transversal momentum component was larger than $-0.5 \text{ GeV}/c$, as indicated by the dashed line, then the event was not taken into account in the further analysis.

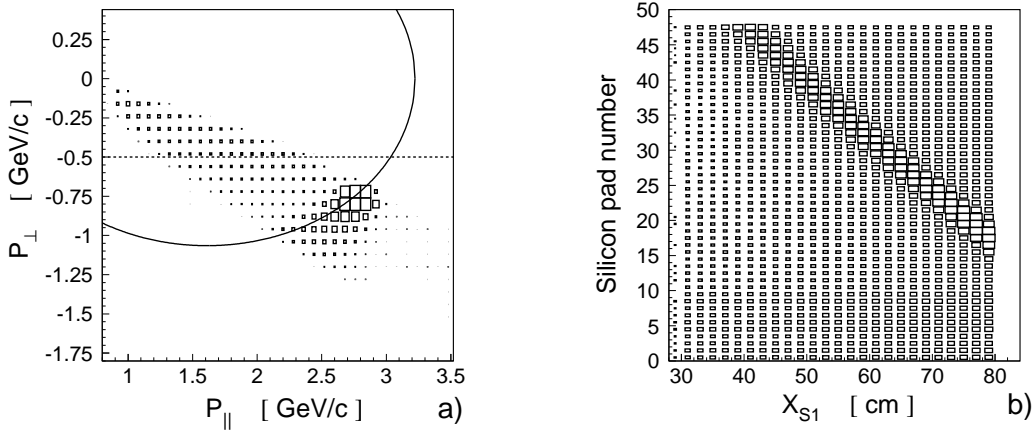


Figure 7.2: (a) Components of the momentum vector of particles registered in both drift chambers and the S1 detector. The momentum component transversal with respect to the beam direction is shown versus the parallel one. The solid line corresponds to the expected dependence between both momentum components for the elastically scattered protons. The dashed line shows the cut performed in the analysis. The shown sample of data was measured at the nominal beam momentum of $P_{beam} = 3222 \text{ MeV}/c$ with the trigger $T_{pp} \equiv T_{S1} \wedge T_{S4}$. (b) Pad number of the silicon detector versus the position in the S1 detector. Only the data below the dashed line from Figure (a) were taken. Essentially only silicon pads with numbers from 14 to 48 and the S1 segments from 1 to 4 recorded simultaneously elastically scattered protons. Note that the number of entries per bin is given in the logarithmic scale.

The two body kinematics gives the unique dependence between the recoil angles Θ_1 and Θ_2 of both scattered protons ($tg\Theta_1 \cdot tg\Theta_2 = \frac{1}{\gamma_{cm}^2}$). Therefore, one expects for events with elastically scattered protons a correlation between the position in the Si and the S1 detectors. Figure 7.2b shows the position measured along the silicon pad detector as a function of the position determined in the S1 scintillator. The observed correlation is close to a straight line.

For the range between 40 *cm* and 80 *cm* along the X_{S1} axis, defined in Figure 7.1, the scattering angle Θ_2^* varies between 64° and 42° . This part of the S1 scintillator was divided into eleven strips each corresponding to the region of the scattering angle $\Delta\Theta_2^*$ equal to 2° . Figure 7.3a shows the projection of the data from Figure 7.2b along the expected correlation line for the range of the scattering angle $\Theta_2^* = 45^\circ \pm 1^\circ$ corresponding to the X_{S1} range of $73\text{cm} \leq X_{S1} \leq 76\text{cm}$. The peak, seen on a rather constant background corresponds to events from elastically scattered protons. The background is due to $pp \rightarrow pn\pi^+$ or other reactions with pion production, where the proton is registered in the drift chambers and the charged pion gives a signal in the silicon detector. The number of entries in the observed peak in Figure 7.3a gives the number of events $\Delta N(\Theta_2^* = 45^\circ)$ with protons scattered at the scattering angle ranging between $\Theta_2^* = 44^\circ$ and $\Theta_2^* = 46^\circ$.

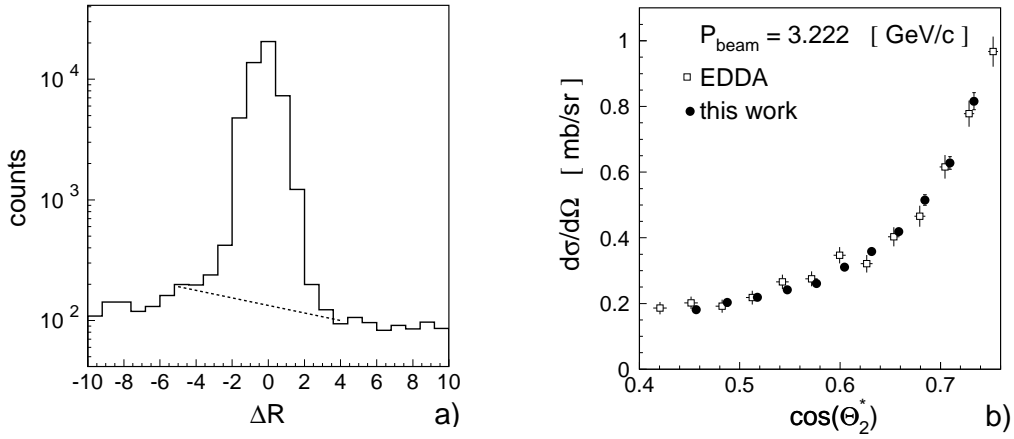


Figure 7.3: (a) Projection of the data from Figure 7.2b along the expected correlation line. The dashed line indicates the estimation of a background. (b) Differential cross section for the elastic proton-proton scattering measured at the beam momentum of $P_{\text{beam}} = 3222 \text{ MeV}/c$. Cross sections measured by the EDDA collaboration are shown by open squares [125]. Full circles indicate the result of the present work. The points from this work are fitted in the overall normalization to the cross section measured by EDDA. To be better distinguishable both the EDDA data and the points from this work were shifted in the horizontal direction from each other by a half size of the point.

The solid angle $\Delta\Omega^*$ corresponding to a given region (strip) in the S1 detector was calculated by means of the Monte Carlo simulation. For this, N_0 events of the elastic proton-proton scattering were simulated taking realistic target and beam parameters, as it is described in chapter 9. Next the simulated events were analyzed in exactly the same way as the real data, and the number of protons N_{accepted} registered in a given S1 region was established. Further the solid angle for this region was calculated as follows:

$$\Delta\Omega^* = \frac{4\pi \cdot N_{\text{accepted}}}{2 \cdot N_0} \quad [\text{sr}], \quad (7.2)$$

where, 4π stands for the full solid angle and factor 2 in the denominator is used because both recoil protons are undistinguishable ².

Figure 7.3 indicates the angular distribution of the differential cross section for the elastic proton-proton scattering obtained in this experiment (full circles) at a beam momentum of $P_{beam} = 3222 \text{ MeV}/c$. The amplitude of this distribution was fitted to the data of the EDDA experiment [125] with the only free parameter being the integrated luminosity. The extracted integrated luminosity amounts to $L = (61.6 \pm 1.4) \cdot 10^{33} \text{ cm}^{-2} = (61.6 \pm 1.4) \text{ nb}^{-1}$, which gives the average luminosity of $l = 8 \cdot 10^{29} \text{ cm}^{-2} \text{ s}^{-1}$.

Table 7.1 summarizes the obtained luminosities for all measurement periods. The variations of the averaged luminosity for the measurements with the COSY-11 optics are due to the fluctuations of the target density, whereas for the measurements with the ramping optics they are caused by the losses of the proton beam during the acceleration cycle.

beam optics	nominal beam momentum P_{beam} [MeV/c]	integrated luminosity [nb^{-1}] \equiv [10^{33} cm^{-2}]	measurement duration [hours]	average luminosity [$10^{29} \text{ cm}^{-2} \text{ s}^{-1}$]
COSY-11	3201	60.9 ± 1.4	22.5	7.5
COSY-11	3214	126.2 ± 3.0	58.0	6.0
COSY-11	3222	61.6 ± 1.4	21.5	8.0
ramping	3222	24.7 ± 0.6	25.0	2.7
ramping	3218	34.3 ± 0.8	25.0	3.8
ramping	3214	36.4 ± 0.9	25.0	4.0
ramping	3210	37.1 ± 0.9	25.0	4.1

Table 7.1: Luminosities and duration of the measurement periods.

The signal to background ratio shown in Figure 7.3a is larger than 100 to 1. Therefore, assuming the background to be estimated with the precision of 20% the systematical error of the background subtraction is about 0.2%. This is negligible with the estimated systematical error of the solid angle ($\Delta\Omega^*$) determination which amounts to $\sim 2\%$ and the absolute normalization of the EDDA differential cross sections $\sim 1\%$ [125]. The overall systematical error of the luminosity determination is equal to **3%**, whereas the statistical error is $\sim 2.4\%$ as can be deduced from table 7.1.

²For instance, if a used detector would be half a sphere, it means it would cover $2\pi \text{ sr}$, then out of N_0 generated events N_0 protons would be registered. Hence, equation 7.2 gives, indeed, a proper result.

8. Absolut beam momentum determination

Near the kinematical threshold the total cross section for the $pp \rightarrow pp\eta'$ reaction grows rapidly with increasing beam momentum. Therefore, in view of the theoretical description, the determination of the absolute beam momentum is as important as the accuracy of the cross section values. The aim of this chapter is to establish the real absolute beam momenta for all measurements and to evaluate the error in the beam momentum determination caused by the applied method.

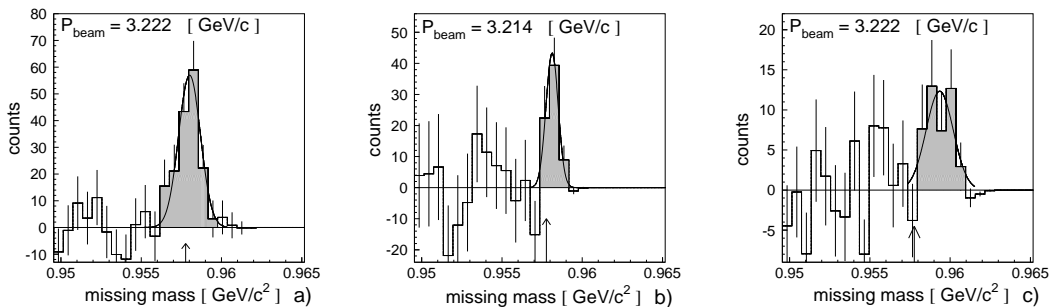


Figure 8.1: (a) Missing mass spectrum measured with the COSY-11 beam optics at a constant nominal beam momentum of 3222 MeV/c . The shaded area corresponds to events assigned to the η' meson production. The fit of the Gaussian distribution to the data is shown as the solid line. The arrow indicates the η' meson mass.

(b) As in a) but for a constant nominal beam momentum of 3214 MeV/c .

(c) Missing mass spectrum measured with the continuous beam momentum change. The data taken at the nominal momentum range between 3220 MeV/c and 3224 MeV/c are shown. Each event was evaluated with the appropriate beam momentum depending on the time past from the beginning of the acceleration cycle. Note that the obtained missing mass peak corresponding to the events for the production of the η' meson is shifted towards larger masses by $\sim 1.5 MeV$ with respect to the η' meson mass.

The absolute beam momentum was calculated from the position of the η' peak in the missing mass spectrum. Figures 8.1a,b,c show the missing mass spectra evaluated for three different measurement periods. The first two 8.1a,b correspond to the measurements with the standard COSY-11 beam optics and the third one to the measurement with the continuous beam momentum increase (ramping optics). A fit of the Gaussian distribution to the missing mass spectra obtained with the COSY-11 optics gives the mean of the peak, which is about $0.3 MeV/c^2$ larger than the mass of the η' meson. This implies that the real beam momen-

tum was about $0.9 \text{ MeV}/c$ smaller than the nominal one. This result is consistent with the momentum offset of $0.7 \text{ MeV}/c$ obtained, by a completely different method [127, 128], from a study of the $pp \rightarrow pK^+\Lambda$ reaction performed with the same beam optics at the COSY beam momentum of $2350 \text{ MeV}/c$ [128].

Figure 8.1c indicates that in case of the ramped beam the obtained missing mass exceeds by about $1.5 \text{ MeV}/c^2$ the η' meson mass, which results in a real beam momentum to be smaller by $\sim 4.5 \text{ MeV}/c$ with respect to the nominal one. Such large offset could still be explained by the inaccuracy of the beam orbit length estimation, which is used for the nominal beam momentum calculations [129].

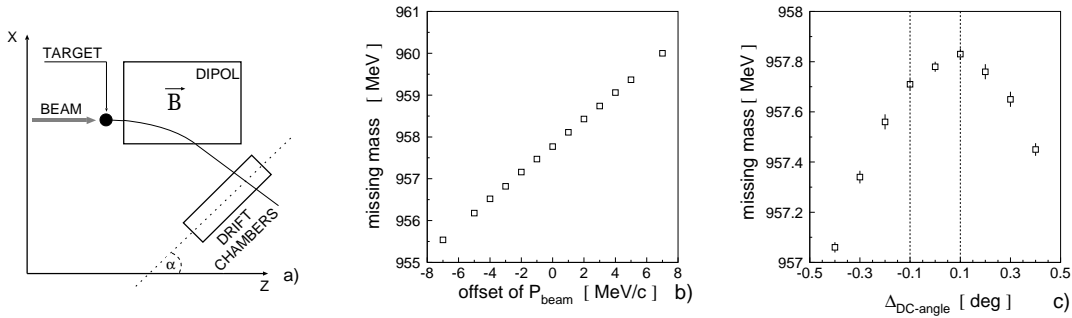


Figure 8.2: (a) Schematic view of the relative settings for the target, the dipole magnet and the drift chamber stack at the COSY - 11 detection system. (b) Offset of the absolute beam momentum transfers linearly to the the missing mass, namely as: $3 \cdot \Delta P [\text{MeV}/c] \simeq \Delta mm [\text{MeV}]$. (c) Missing mass of the η' meson as a function of the error of establishing the drift chamber angle. This angle is known with an accuracy better than $\pm 0.1^\circ$ where the missing mass changes by less than $\sim 0.15 \text{ MeV}$. The results of b) and c) were obtained by means of the Monte Carlo method.

The used method assumes that the deviation of the experimental missing mass from the real meson mass is due to the offset between the real beam momentum and the one used in the analysis as shown in Figure 8.2b. Consequently the precision of calculating this offset is influenced by the inaccuracy of the four-momentum vectors of both protons, since they are also used in the missing mass computations. Thus the accuracy of the absolute beam momentum determination from a missing mass spectrum is defined by the accuracy of the measured proton momenta, which are derived from the numerical reconstruction of the track between the target and the drift chambers (see Figure 8.2a) through the magnetic field in the dipole.

The crucial parameters for the proton momentum determination and hence for the meson mass calculations are the target position, the magnetic field in the dipole and the settings of the drift chambers. Figures 8.2c and 8.3a,b,c depict how the error of these parameters influences the determination of the missing mass.

This study was performed by simulating a sample of events with the Monte Carlo method and then analyzing them in the same way as the experimental data.

The simulated “data” were analyzed varying the target position, drift chambers angle, and the dipole magnetic field with respect to the one used in the simulations ¹. The dashed lines in Figures 8.2c and 8.3a,b,c indicate the maximum expected deviation in the determination of the considered parameters. The systematical error of the target position and the angle of the drift chambers is smaller than 2 mm and 0.1° , respectively. Specifically the 0.1° was deduced assuming that the inaccuracy of the drift chamber stack position amounts to $\sim 3\text{ mm}$. This very conservative assumption was checked by performing the track reconstruction for the experimental data in each drift chamber separately. It was found, that the difference of the relative angle between the drift chambers extracted from the experimental data and the angle calculated from the measured chamber geometry was smaller than 0.1° .

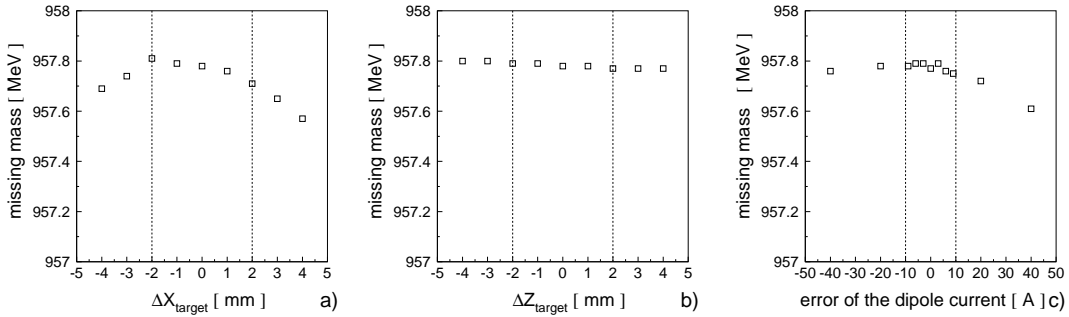


Figure 8.3: (a) The reconstructed missing mass versus the deviation of the target position in the horizontal direction perpendicular to the beam axis. The position of the target is known with an accuracy better than $\pm 2\text{ mm}$ which corresponds to the missing mass variation smaller than $\sim 0.1\text{ MeV}$. (b) Missing mass versus the deviation of the target position along the beam direction. Since the position of the target is known to be better than $\pm 2\text{ mm}$ the missing mass variation caused by this parameter is less than $\sim 0.04\text{ MeV}$. (c) Missing mass versus changes of the dipole current. The absolute current value used in the measurement of the $pp \rightarrow pp\eta'$ reaction was $\sim 3700\text{ A}$ which corresponds to the vertical magnetic field component of $\sim 1.53\text{ T}$. The magnetic field is known with the accuracy better than 0.25% which is equivalent to a missing mass variation of less than $\sim 0.06\text{ MeV}$.

The three space components of the magnetic field were measured for a few different dipole currents by means of a Hall probe with an accuracy of 0.1% [121, 119]. However, because of the interpolation error the overall accuracy amounts to $\sim 0.25\%$ [120]. Hence, for the dipole currents used in this experiment, which ranged between 3687 A and 3724 A depending on the beam momentum, the

¹In the simulation the target dimensions, the beam spread in space and momentum, as well as the drift chamber resolution were taken into account. All mentioned parameters were established from the experimental data. The target is a cylindrical hydrogen beam with a diameter of 9 mm . The proton beam has the Gaussian distribution in horizontal and vertical direction with $\sigma \sim 4\text{ mm}$ and the beam momentum spread of $1.2\text{ MeV}/c$ (see chapter 9).

expected systematical error of the dipole current should be smaller than 10 A as shown by the vertical lines in Figure 8.3c.

Thus, i) a misalignment of the angles of the drift chambers relative to the chosen coordinate system (Figure 8.2c), ii) an uncertainty in the definition of the target position in both vertical and longitudinal directions (Figures 8.3a,b), and iii) the inaccuracy of the knowledge of the dipole magnetic field (Figure 8.3c) altogether result in an error of the reconstructed missing mass of less than ~ 0.35 MeV. This gives the systematical error in the absolute beam momentum determination of 1.1 MeV/c, which is two times smaller than the error of the estimations based on the beam orbit length and the revolution frequency [125].

Table 8.1 compares the nominal beam momenta with the real ones evaluated from the position of the η' peak in the missing mass spectrum.

beam optics	P_{beam} nominal [MeV/c]	beam momentum correction ΔP_{beam} [MeV/c]	ΔP_{beam} averaged [MeV/c]	P_{beam} real [MeV/c]	real excess energy Q [MeV]
COSY-11	3222	0.8	0.9	3221.1 ± 1.1	4.1 ± 0.4
COSY-11	3214	1.0		3213.1 ± 1.1	1.5 ± 0.4
ramping	3222	4.8	4.5	3217.5 ± 1.1	2.9 ± 0.4
ramping	3218	4.2		3213.5 ± 1.1	1.7 ± 0.4
ramping	3214	—		3209.5 ± 1.1	0.3 ± 0.4
ramping	3210	—		3205.5 ± 1.1	-0.9 ± 0.4

Table 8.1: Absolute beam momenta

The obtained results show that the difference between the true and the nominal beam momentum depends on the tuning of the accelerator. Particularly, the nominal beam momentum calculated using the parameters of the COSY accelerator is greater than the true value obtained from the experimental data. It is worth noting that the similar conclusions were drawn for the SATURNE accelerator [20].

The measurements with the ramping optics at the 4 MeV/c momentum bins with the averaged beam momenta as quoted in the two last lines in table 8.1 will not be taken into account in the further analysis. This is because the true excess energies found for these measurements are smaller or equal to zero within the estimated errors. This fact explains also why the number of $pp \rightarrow pp\eta'$ events derived for this measurements is consistent with zero as it is shown in table 6.1 on page 45.

9. Detection efficiency

9.1 Efficiency definition

In this chapter the procedure of the detection efficiency calculations will be presented. The efficiency E_{eff} can be defined as the ratio of the number of detected $pp \rightarrow pp\eta'$ reactions to the total number of $pp \rightarrow pp\eta'$ events which occurred in the target.

In order to establish this ratio a sample of $N_{generated}$ $pp \rightarrow pp\eta'$ events was simulated and subsequently, the response of all detectors was evaluated by means of a GEANT [130] program, for each event separately. The generated detector signals were written on disk and analyzed in the same way as the experimental data. The analysis of the simulated events results in the number $N_{accepted}$ of identified $pp \rightarrow pp\eta'$ reactions. Hence, the ratio $N_{accepted}/N_{generated}$ gives the detection efficiency E_{eff} , which in general should be dependent on the angular distribution of the reaction products, what is neglected here since only S-waves contribute to the threshold production.

In the calculations of the E_{eff} value the real target dimensions, as well as the beam spread in momentum and space must be taken into account. Therefore evaluation of the values of E_{eff} is preceded by the estimation of the beam and the target parameters.

9.2 Beam momentum spread

The beam momentum spread $\frac{\Delta p}{p}$ was measured on the basis of the following equation [131]:

$$\frac{\Delta f}{f} = \frac{1}{\gamma_{tr}^2} \frac{\Delta B}{B} + \left(\frac{1}{\gamma^2} - \frac{1}{\gamma_{tr}^2} \right) \frac{\Delta p}{p} \quad (9.1)$$

where Δf is the change of the beam revolution frequency f corresponding to the variation ΔB of the dipole magnetic field B . The Lorentz factor γ is equal to $\gamma = \sqrt{p^2 + m^2}/m$, where m is the proton mass. The value of the quantity $\gamma_{tr} = 2.18$ was established before the experiment. This was performed by the measurement of the beam revolution frequency changes Δf caused by the variation of the dipole magnetic field B , where the dipole magnetic field was changed so much that the term $\left(\frac{1}{\gamma^2} - \frac{1}{\gamma_{tr}^2} \right) \frac{\Delta p}{p}$ in equation 9.1 could be neglected in comparison to $\frac{\Delta B}{B}$ ¹.

¹By changing the magnetic field the accelerating RF-cavity was switched off. Therefore one expects that the Δp was equal to zero.

On the other hand, during the experiment the variation of the magnetic field B can be neglected and the value of the $\frac{\Delta p}{p}$ can be obtained by measuring the value of $\frac{\Delta f}{f}$ applying the approximate equation:

$$\frac{\Delta f}{f} = \left(\frac{1}{\gamma^2} - \frac{1}{\gamma_{tr}^2} \right) \frac{\Delta p}{p}. \quad (9.2)$$

In this experiment the value of the standard deviation Δf was controlled every few hours, and it was found to vary between 65 Hz and 80 Hz . The mean revolution frequency for the beam momentum of $3222 \text{ MeV}/c$ is equal to $f = 1.56876 \text{ MHz}$. Hence, according to equation 9.2, the standard deviation of the beam momentum spread varied between $\Delta p = 1.0 \text{ MeV}/c$ and $\Delta p = 1.2 \text{ MeV}/c$. Thus, on the average $\Delta \mathbf{p} = 1.1 \text{ MeV}/c \pm 0.1 \text{ MeV}/c$. This implies that the relative momentum spread is equal to $\frac{\Delta \mathbf{p}}{p} = \frac{1.1}{3222} = 3.4 \cdot 10^{-4}$.

9.3 Target and beam dimensions

The cluster target beam diagnostic was performed by the elastic electron scattering with a 5 keV electron beam [16, 98]. It was established, that the cluster beam is homogenous with a diameter of **9 mm**.

For the simulation it is important to know the overlap between the COSY proton beam and the cluster target beam. Therefore the knowledge of the beam parameters is also necessary. The density of the circulating proton beam at the target place can approximately be described by the Gaussian distribution in the horizontal and vertical direction. The standard deviations for both, the horizontal (σ_x) and vertical (σ_y) distribution are given by the beam optics parameters as follows [99, 17]:

$$\sigma_x = \sqrt{\epsilon \cdot \beta_x + D_x^2 \cdot \left(\frac{\Delta p}{p} \right)^2}, \quad \sigma_y = \sqrt{\epsilon \cdot \beta_y}, \quad (9.3)$$

where ϵ denotes the beam emittance ², $\beta_x = 10.0 \text{ m/rad}$ and $\beta_y = 12.0 \text{ m/rad}$ called beta-functions are defined by the quadrupole focusing strength varying along the accelerator ring, and $D_x = 0.2 \text{ m}$ denotes the dispersion at the target point. Taking $\frac{\Delta p}{p} = 3.4 \cdot 10^{-4}$ and applying the above values in the equation 9.3 one obtains that: $\sigma_x = 4.1 \text{ mm}$ and $\sigma_y = 4.5 \text{ mm}$. This estimations were performed for the COSY-11 beam optics. For the ramping optics one obtains $\sigma_x \approx 12.6 \text{ mm}$ and $\sigma_y \approx 4.3 \text{ mm}$. The density distribution of the beam-target overlap does not

²The beam emittance [132] at a given beam momentum can be obtained from the Liouville theorem $\epsilon\beta\gamma = \text{const.}$, and the known emittance by the injection which amounted to $\epsilon^{inj} = 20 \text{ mm mrad}$. The beam momentum by injection is $P_{beam} = 276.9 \text{ MeV}/c$, which implies $\gamma^{inj}\beta^{inj} = 0.295$. Thus, the beam emittance at $P_{beam} = 3222 \text{ MeV}/c$ is $\epsilon = 1.72 \text{ mm mrad}$, since $\gamma\beta = 3.43$.

change significantly if the horizontal beam spread exceeds $\sigma_x \approx 4.5 \text{ mm}$ since, the target diameter is equal to 9 mm .

In case of the ramping tuning the large horizontal dimension of the beam caused, however, that more than half of the beam was circulating outside the target leading to the decrease of the luminosity in comparison to the measurements with the COSY-11 beam optics (compare table 7.1 on page 50).

The density of the beam-target overlap and the luminosity depends also on the position of the middle of the beam relative to the target centre. Therefore the proton beam was adjusted at the centre of the target by means of small dipole magnets called steerers [132], which were installed in the COSY ring, a few meters from the target. During the variation of the steerer magnetic field, which causes a shift of the beam with respect to the target, the counting rate of the “elastic trigger” T_{pp} was monitored. The optimal steerer parameters were adjusted to the maximum registered counting rate. This procedure, performed before the experiment, allowed to adjust the beam on the target with the precision better than 1 mm . The stability of the position of the COSY beam with respect to the target was controlled during the experiment by means of the beam position monitors [131].

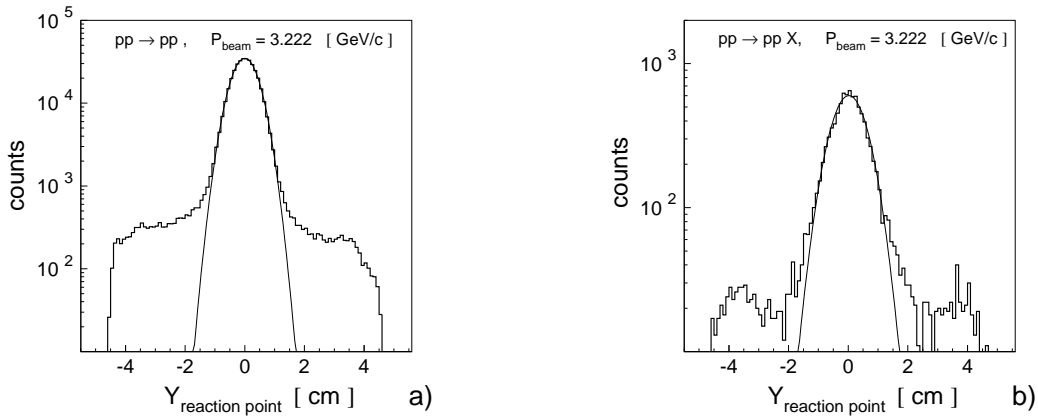


Figure 9.1: The distribution of the vertical component of the reaction point obtained in the experiment for the beam momentum of $3222 \text{ MeV}/c$. The solid line shows the fitted Gaussian distribution.

(a) The spectrum obtained for the data with the elastically scattered protons. The sigma of the fitted Gaussian function amounts to 4.2 mm (b) The spectrum of the data with the $pp \rightarrow ppX$ reactions. The standard deviation of the fitted function is equal to 5.9 mm .

In the following the obtained values for the $\sigma_y = 4.5 \text{ mm}$ and $\Delta p = 1.1 \text{ MeV}/c$ will be confronted with corresponding values obtained from the analysis of the experimental data.

For the momentum reconstruction of the ejected particles it was assumed that

their trajectories pass through the nominal target position in the horizontal plane. Therefore, from the particle track reconstruction it was not possible to determine the extensions of the target in the horizontal direction. However, this restriction was not necessary in the vertical direction, and it was possible to determine the vertical beam profile at the target by tracing the particle trajectory. Figure 9.1a shows the distribution of the reconstructed vertical component of the reaction point for the elastically scattered protons registered at a beam momentum of $3222 \text{ MeV}/c$, which can be well described by the Gaussian distribution with the standard deviation of $\sigma_y = 4.2 \text{ mm}$. “Tails” seen at both sides of the Gaussian function are due to the secondary scattering on the vacuum chamber or originate from the reactions at the rest gas spread near the target. The standard deviation of the vertical beam spread determined from the data with two registered protons is significantly larger, and amounts to $\sigma_y = 5.9 \text{ mm}$, as shown in Figure 9.1b. This difference of the σ_y determination is due to the differences of the multiple scattering in the exit window, drift chamber foils and air. The multiple scattering decreases with the growing energy of the particle traversing the medium, and protons ejected from the $pp \rightarrow pp\eta'$ reaction have kinetic energy about 480 MeV , whereas the kinetic energy of the registered elastically scattered protons is about 1360 MeV .

Additional factors, which may influence the width of the distributions shown in Figures 9.1a,b are the horizontal beam spread and the beam momentum spread. The effect of this parameters on the σ_y determination is presented in Figures 9.2a,b. Using the Monte Carlo method samples of $pp \rightarrow pp\eta'$ and $pp \rightarrow pp$ events were generated with the vertical beam spread of $\sigma_y = 4.0 \text{ mm}$ for a few different values of the horizontal beam spread σ_x (Figure 9.2a), and different values of the beam momentum spread σ_p (Figure 9.2b). In the simulation the effect of multiple scattering, and the target dimensions were taken into account. The generated events were next analyzed in the same manner as those from the experiment, and the value of σ_y was evaluated. The reconstructed value of σ_y amounts to $\sim 4.2 \text{ mm}$ in case of the $pp \rightarrow pp$ reaction and $\sigma_y \approx 5.8 \text{ mm}$ in case of the $pp \rightarrow pp\eta'$ reaction independently of the value of σ_x or σ_p .

The very good agreement of the simulated and experimental data allows to determine the standard deviation of the vertical beam spread to be $\sigma_y = 4.0 \text{ mm}$, which differs by only 12.5 % from the value $\sigma_y = 4.5 \text{ mm}$ determined from the beam optics. Therefore, for the further evaluation of the detection acceptance the averaged value $\sigma_y = 4.3 \text{ mm}$ will be used. In case of the horizontal beam spread the value of $\sigma_x = 4.1 \text{ mm}$ derived from the beam optics will be applied, since there is no possibility of establishing it from the experimental data.

With σ_y and σ_x one can now estimate a value of the beam momentum spread from the experimental data.

The fit of the Gaussian distribution to the missing mass spectrum, measured at a beam momentum of $P_{beam} = 3222 \text{ MeV}/c$, as shown in Figure 8.1a on page 51, gives the standard deviation of the missing mass spread of $\sigma_{mm} = 0.68 \text{ MeV}$.

This spread is caused i) by the finite dimension of the beam-target overlap, ii) by the inaccuracy of the track reconstruction, which is due to the drift chamber position resolution and the effect of the multiple scattering, iii) by the spread of the beam momentum, and iv) by the natural width of the η' meson $\Gamma_{\eta'} \approx 0.2 \text{ MeV}/c^2$. With the known conditions for i) the beam and the target, and ii) the drift chamber position resolution, one can estimate the beam momentum spread from the measured spread of the missing mass spectrum. From Figure 9.2c it can be deduced that the beam momentum spread is $\Delta p = 1.3 \text{ MeV}/c$, which is close to the value $\Delta p = 1.1 \pm 0.1 \text{ MeV}/c$ obtained from the measurement of the beam revolution frequency spread. Again, the mean of the values from both methods, $\Delta p = 1.2 \text{ MeV}/c$, will be taken for further considerations.

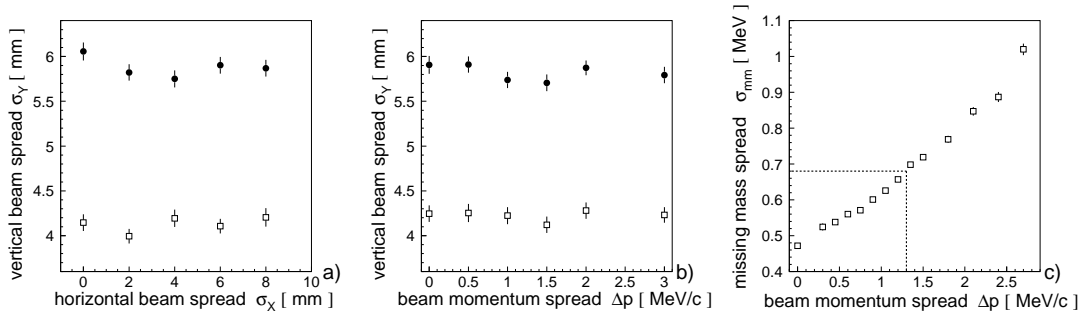


Figure 9.2: Results of the analysis of the simulated events. In (a) and (b), the solid circles correspond to the $pp \rightarrow pp\eta'$ reaction and the open squares to the $pp \rightarrow pp$ one. (a) The reconstructed value of σ_y as a function of the value of σ_x used in the simulations. (b) The reconstructed vertical beam extension versus the beam momentum spread used in the Monte Carlo calculations. (c) Dependence of the missing mass resolution on the beam momentum spread, as obtained from the Monte Carlo simulations with the beam momentum of $3222 \text{ MeV}/c$, the target diameter of 9.0 mm , $\Gamma_{\eta'} = 0.201 \text{ MeV}/c^2$, and with the vertical and horizontal beam spread equal to $\sigma_x = 4.1 \text{ mm}$ and $\sigma_y = 4.3 \text{ mm}$, respectively. The experimental value of the missing mass spread $\sigma_{mm} = 0.68 \text{ MeV}$ implies the beam momentum spread of $\Delta p \approx 1.3 \text{ MeV}/c$ as indicated by the dashed line.

9.4 Geometrical acceptance

The detection efficiency E_{eff} comprises the geometrical acceptance of the detection system and the ability of the event reconstruction from the registered signals.

The geometrical acceptance for the $pp \rightarrow pp\eta'$ reaction is shown in Figure 9.3a as a function of the beam momentum above threshold. This acceptance, defined here as the ratio of the number of events for which two protons reach the S3 detector to the number of events generated in the target, depends on the angular

distribution of the reaction products. Though the exact angular distribution is not known, it could be assumed, that it is predominantly determined by the three body phase space and the final state interaction of the outgoing protons, which is especially strong for protons with small relative momentum at a 1S_0 wave [133, 134].

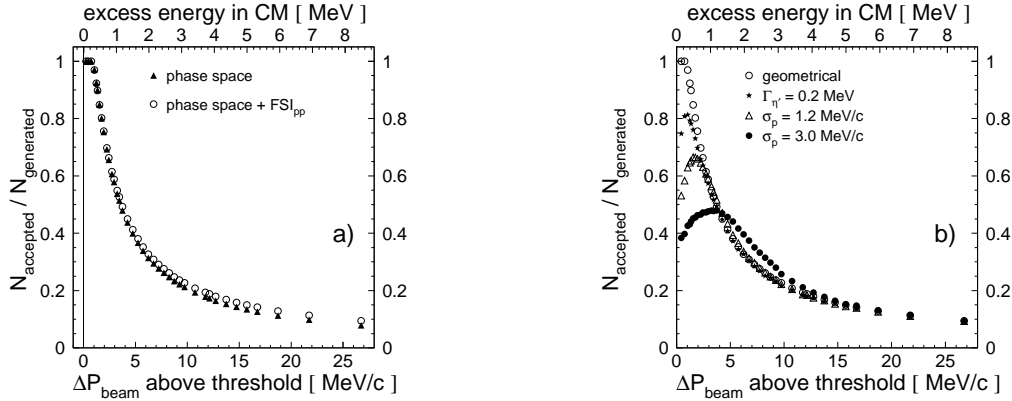


Figure 9.3: Efficiency of the detection system for the $pp \rightarrow pp\eta'$ reaction as a function of the beam momentum above threshold (lower axis), or as a function of the excess energy (upper axis)

(a) The efficiency obtained assuming the point-like target and the ideal proton beam with no spread in momentum or space. Full triangles indicate the computation performed under the assumption that the momentum distribution of the outgoing particles is governed by the three body phase space only. Taking into account the proton-proton final state interaction gives the open circles (see appendix C). (b) Open circles are the same as in Figure a). Stars indicate the ratio defined in a) but taking into account the natural width of the η' meson and the real beam and target dimensions. For the open triangles and solid circles additionally the beam momentum spread was included in the simulations.

Figure 9.3a depicts that the efficiency obtained with and without proton-proton final state interaction differs by about 9 % at a beam momentum of $3222 \text{ MeV}/c$ (ΔP_{beam} above threshold $\approx 14 \text{ MeV}/c$) and by about 4 % at a beam momentum of $3214 \text{ MeV}/c$ (ΔP_{beam} above threshold $\approx 6 \text{ MeV}/c$).

The real beam and target dimensions and the effect of the multiple scattering included in calculations, decreases the efficiency by about 2 %. A further decrease of about 3 % is caused by the nuclear reactions in the detector media and air. The 3 % losses due to the nuclear reactions, obtained by means of the GEANT simulation program agrees with rough estimations. Namely, before the two protons produced in the target reach the S3 detector they pass through the S1, S2 and S7 scintillators, which altogether constitutes 1.4 cm of the plastic scintillator material. One cubic centimeter of such material contains about $5.2 \cdot 10^{22}$ atoms of

hydrogen and about $4.7 \cdot 10^{22}$ atoms of carbon [103]. Taking the total cross section for the proton-proton reaction as $\sim 40 \cdot 10^{-27} \text{ cm}^2$ [25] and for the proton-carbon as $\sim 280 \cdot 10^{-27} \text{ cm}^2$ ³ one obtains, that at least one of the two protons will undergo a nuclear reaction in the S1, S2 or S7 scintillators with 4 % probability⁴.

The beam momentum spread influences the value of the efficiency E_{eff} as well, which is particularly strong, if the spread is comparable with the value of the beam momentum above the reaction threshold. As an extreme example let us consider a measurement with the beam momentum being exactly the threshold momentum but with a finite spread. Then only half of the protons circulating in the accelerator ring possess enough energy to initiate the studied reaction, whereas all of them could contribute to the elastic scattering.

Figure 9.3b shows that a beam momentum spread of $1.2 \text{ MeV}/c$ causes changes of the efficiency in the order of 2 % for the beam momentum ranging between $6 \text{ MeV}/c$ and $14 \text{ MeV}/c$ above threshold. This figure depicts also that the number of registered events, in this momentum range, would grow with the increasing beam momentum spread. As an example the calculations for the $\sigma_p = 3.0 \text{ MeV}/c$ are shown by full circles.

9.5 Efficiency of the track reconstruction in the drift chambers

The efficiency of the track reconstruction for events with two simultaneously registered particles influences significantly the overall detection efficiency as can be seen in figure 9.4a. For the calculations of the reconstruction efficiency, the program for track reconstruction was applied to a sample of events generated by the Monte Carlo method. For the generation of the drift chamber signals, the two-track-resolution was taken to be 3 mm as established in chapter 5.1. It means that two tracks in a given detection plane being closer than 3 mm were only registered as one signal. The position resolution of the detection cell was simulated by smearing out the distance between the sense wire and the particle trajectory. The distances were smeared out according to the Gaussian distribution with the standard deviation of 0.25 mm , which was evaluated also in chapter 5.1.

Figure 9.4b shows that the reconstruction efficiency decreases strongly with the worsening of the two-track-resolution and with the decreasing beam momentum above threshold. The latter is due to the decreasing distances between tracks in the drift chambers the closer the threshold is approached.

³According to the Glauber theory the total cross section for the proton-carbon reaction is approximately given by $\sigma_{pC} = \sigma_{pp} \cdot 12^{0.78}$ [135].

⁴A probability that one proton causes a nuclear reaction flying through the scintillator of 1.4 cm thickness amounts to: $P = 1.4 \cdot 4.7 \cdot 10^{22} \cdot 280 \cdot 10^{-27} + 1.4 \cdot 5.2 \cdot 10^{22} \cdot 40 \cdot 10^{-27} = 0.021$. Thus, the probability that at least one proton out of two will cause a nuclear reaction equals $1 - (1 - P)^2 = 0.04$.

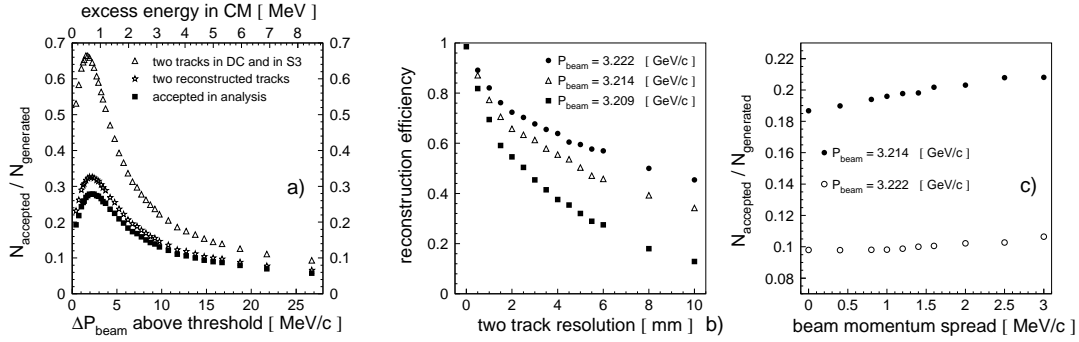


Figure 9.4: (a) Simulated efficiency of the detection system as a function of the beam momentum above threshold (lower axis), or as a function of the excess energy (upper axis). The triangles are the same as in figure 9.3b. Stars indicate the ratio of the number of events for which both proton trajectories were reconstructed to the number of all generated events. The solid squares indicates the ratio of the number of events which fulfilled all requirements demanded in the analysis to the number of all generated events. (b) Efficiency of the two track reconstruction as a function of the two-track-resolution of the drift chambers. The two-track-resolution was estimated to be $3.0 \text{ mm} \pm 1.0 \text{ mm}$, where the error of $\pm 1.0 \text{ mm}$ causes the inaccuracy of the reconstruction efficiency of about $\pm 8\%$. (c) The overall detection efficiency as a function of the beam momentum spread for the nominal beam momentum of $P_{\text{beam}} = 3222 \text{ MeV}/c$ and $P_{\text{beam}} = 3214 \text{ MeV}/c$. Taking the beam momentum spread of $1.2 \text{ MeV}/c$ with the accuracy of $\pm 0.1 \text{ MeV}/c$ one obtains the changes of the detection efficiency of $\pm 0.5\%$.

The two-track-resolution is established with an accuracy of $\pm 1 \text{ mm}$. Thus, changing it from 3 mm to 4 mm one observes the variation of the reconstruction efficiency by 8% . Contribution to the systematical error from the inaccuracy of the beam momentum spread is much smaller and amounts to $\sim 0.5\%$, see figure 9.4c.

The relative position of the detectors, the dipole magnet, and the target is known with the accuracy of $\sim 2 \text{ mm}$, which may lead to the error in acceptance smaller than 1% . Similarly the errors of regarding losses caused by multiple scattering and nuclear reaction is smaller than 1% . Finally, the error of the efficiency due to the inaccuracy of the calculations of the proton-proton final state interaction is assumed to be smaller than 0.5% , since the whole effect causes changes smaller than 9% and the parameters of the proton-proton scattering are well known (see appendix C).

Summarizing the contributions from all above effects the systematical error of the detection efficiency evaluation is established to be 11% .

The full squares in figure 9.4a denote the overall detection efficiency obtained regarding all discussed effects and the requirements used in the data analysis. Table 9.1 gives values of the detection efficiency E_{eff} evaluated for the real beam

momenta of the measurements presented in this work.

P_{beam} real [MeV/c]	systematical error of P_{beam} [MeV/c]	E_{eff} detection efficiency	systematical error of $E_{eff} = 11\%$
3213.1	1.1	0.225	0.025
3213.5	1.1	0.209	0.023
3217.5	1.1	0.139	0.015
3221.1	1.1	0.106	0.012

Table 9.1: Detection efficiency

9.6 Energy loss analysis - events with close flying particles

The aim of the following analysis is to check the value of the efficiency for the reconstruction of two tracks as established by the Monte Carlo simulation in the previous sections.

For the evaluation of the number of the $pp \rightarrow pp\eta'$ reactions, presented in section 6.4 only those events were considered for which at least two tracks were reconstructed from the signals in the drift chambers. This analysis gave $N = 164.3 \pm 23.4$ at a nominal beam momentum of $P_{beam} = 3222 \text{ MeV}/c$, where the efficiency of the two track reconstruction amounts to 68% as shown in Figure 9.4b, leaving 77 ± 11 events corresponding to the $pp \rightarrow pp\eta'$ reaction to be found among events with only one reconstructed track.

A method based on the energy loss analysis is used for the identification of events with two close protons, for which only one track was reconstructed. Selecting such events and assuming that both protons have the same momentum it is possible to calculate the mass of a non-observed system which should be equal to the η' meson mass in the case of the $pp \rightarrow pp\eta'$ reaction. If the obtained number of events with the η' production, among events of one reconstructed track, will be consistent with 77 ± 11 then the evaluated reconstruction efficiency would be confirmed.

At first, the energy loss information was used for the identification of the number of registered particles.

Figures 9.5a,b,c show the normalized energy loss distribution corresponding to one proton (white histogram) or two protons (shaded histogram) crossing the S1, S2 or S3 detectors, respectively. The spectrum for the S7 detector, not shown here, looks similarly as this of the S1 counter. The values presented on the horizontal axis are equivalent to the energy loss measured in detectors divided by the expected energy loss for one proton. The expected energy loss was calculated

multiplying the stopping power, which depends on the particle velocity, by the path length in the scintillator material. The velocity is known from the time of flight measurement, and the values of the stopping power was taken from the literature [136].

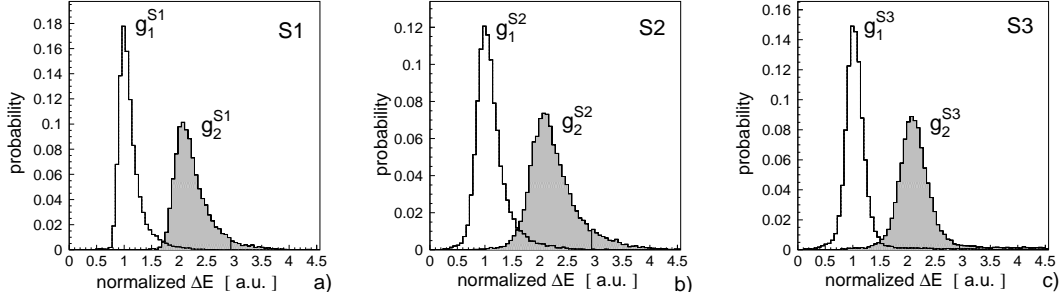


Figure 9.5: Energy loss spectra for one and two particles crossing the scintillation detectors. The energy loss is normalized to the expected energy loss for one particle obtained from the known stopping power and the path length in the scintillator. The shaded histogram corresponds to two particles crossing the detector. The number of entries per energy bin was normalized so that the sum over all bins is equal to 1.

(a) Energy loss for the S1 detector, (b) for S2 and (c) for S3.

In the case of the S1 detector, with the thickness of 4 mm, the energy distribution has the Vavilov [107] form and for the S3 detector having a thickness of 50 mm it is close to the Gaussian function. In the case of the S2 scintillator having thickness of 2.0 mm one would expect the form close to the Landau [107] distribution, however the observed one is rather the Gaussian. This is because of the relatively poor resolution of the light collection in this thin and long detector.

Each event is characterized by a set of five values of the normalized energy loss measured in the scintillation detectors, namely:

$$\Delta E \equiv (\Delta E_{S1}, \Delta E_{S2}, \Delta E_{S3}, \Delta E_{S7a}, \Delta E_{S7b}).$$

The white and shaded histograms in Figures 9.5 can be treated as the probability functions for the registration of the given energy loss if one or two protons crossed the detector, respectively. Calling this probability functions g_i^{Sj} as indicated in Figures 9.5 one can define a probability that a given set of measured ΔE values corresponds to one registered track, namely:

$$P_{1tr}(\Delta E) = g_1^{S1}(\Delta E_{S1}) \cdot g_1^{S2}(\Delta E_{S2}) \cdot g_1^{S3}(\Delta E_{S3}) \cdot g_1^{S7a}(\Delta E_{S7a}) \cdot g_1^{S7b}(\Delta E_{S7b}), \quad (9.4)$$

and similarly the probability P_{2tr} that the given set of ΔE values corresponds to the event with two tracks is given by:

$$P_{2tr}(\Delta E) = g_2^{S1}(\Delta E_{S1}) \cdot g_2^{S2}(\Delta E_{S2}) \cdot g_2^{S3}(\Delta E_{S3}) \cdot g_2^{S7a}(\Delta E_{S7a}) \cdot g_2^{S7b}(\Delta E_{S7b}), \quad (9.5)$$

In order to decide, for each event, whether the measured set of ΔE values is due to one or two protons crossing the detectors the *Neyman-Pearson test* [137] was used, which here is the *most powerful* one. Thus, for each event a ratio of the likelihoods $\alpha = P_{2tr}/P_{1tr}$ was calculated, and for $\alpha > \alpha_0$ the event was regarded as if two protons crossed the detectors. The criterion α_0 and the functions g from Figures 9.5 determine the probability for making an error by accepting the hypothesis that two particles cross the detectors when it is false. This error called *contamination* can be calculated by summing the probability P_{1tr} over the whole range of the ΔE values where the requirement that $\alpha = P_{2tr}/P_{1tr} > \alpha_0$ is fulfilled. Hence:

$$\text{contamination} = \sum P_{1tr}(\Delta E)\Theta(\alpha - \alpha_0), \quad (9.6)$$

where the summation is over the whole ΔE space, and Θ denotes the Heaviside function. Similarly one can calculate the probability for making an error of rejecting the hypothesis that two particles cross the detectors when it is true, which is called *loss*:

$$\text{loss} = \sum P_{2tr}(\Delta E)\Theta(\alpha_0 - \alpha). \quad (9.7)$$

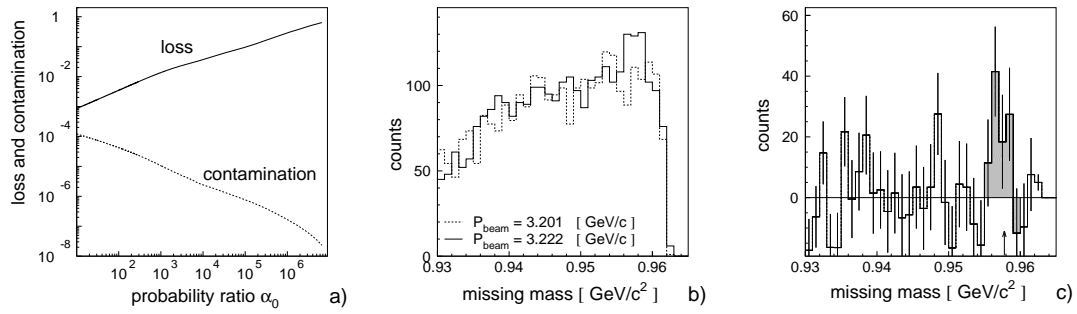


Figure 9.6: (a) Contamination - the probability of accepting the hypothesis that two particles cross the detector when it is false. Loss - probability of rejecting the hypothesis that two particles cross the detector when it is true. Both quantities are shown as a function of the probability ratio α_0 defined in the text. The calculations were performed applying equations 9.6 and 9.7. (b) Missing mass spectrum obtained under the assumption that events with the probability ratio α larger than 10^5 are with two close tracks crossing the detectors. The dashed line corresponds to the measurement below threshold at a beam momentum of $P_{beam} = 3201$ MeV/c and the solid line indicates the measurement above threshold at $P_{beam} = 3222$ MeV/c (c) Difference between solid and dashed histogram from b).

By choosing the parameter α_0 one has to find the compromise between the number of lost events with two protons and the contamination of the selected sample with the events with one proton.

For the measurement at $P_{beam} = 3222$ MeV/c about $8 \cdot 10^6$ events with one reconstructed track were registered. Among them we expect about 1000 events

with two close flying protons. The number 1000 is deduced from the missing mass spectrum in Figure 6.5, where ~ 163 events are due to the $pp \rightarrow pp\eta'$ reaction and about 2000 events from the multi pion production. Now we expect to find ~ 77 $pp \rightarrow pp\eta'$ reactions, hence $\frac{77}{163} \cdot 2000 \approx 1000$. Thus, the discussed sample of data consists of about $\frac{8 \cdot 10^6}{1000} \approx 10^4$ times more events with one proton than with two protons. Therefore the parameter α_0 was chosen to be $\alpha_0 = 10^5$ which will suppress the number of events with one proton by more than a factor of 10^6 losing only $\sim 10\%$ of events with two close flying protons, see Figure 9.6a.

In order to select the events with two protons out of all events with one reconstructed track the *Neyman-Pearson test* with a parameter $\alpha_0 = 10^5$ was applied to the data taken at $P_{beam} = 3201$ MeV/c and at $P_{beam} = 3222$ MeV/c. Further the missing mass spectra were evaluated, as shown in Figure 9.6b, by assuming that both protons have the same momentum. The dashed histogram for the beam momentum of $P_{beam} = 3201$ MeV/c is already normalized to the measurement at $P_{beam} = 3222$ MeV/c according to the integrated luminosity, and shifted to the kinematical limit defined by $P_{beam} = 3222$ MeV/c. Subtracting the histogram below threshold from the one above threshold one obtains a spectrum, shown in Figure 9.6c, with an enhancement at the position corresponding to the mass of the η' meson.

The number of $pp \rightarrow pp\eta'$ events in the peak amounts to 85 ± 33 ⁵, which is consistent with the expected 77 ± 11 events, and hence authenticate the two track reconstruction efficiency evaluated by the Monte Carlo simulations.

⁵Taking into account a 10% *loss* one obtains $\sim 94 \pm 36$ events, which is still consistent with 77 ± 11 .

PART III

RESULTS AND DISCUSSION

Teorie mijają a żaba zostaje
J. Rostand

10. Total cross section

Let us recall the formula for the total cross section:

$$\sigma(Q) = \frac{N(Q, T)/E_{eff}(Q)}{L(T)}, \quad (10.1)$$

all quantities from this formula were established in previous chapters, for each measurement period, and so, the number of measured η' mesons N can be found in table 6.1 on page 45. Table 7.1 on page 50 presents the obtained values of luminosities L , table 8.1 on page 54 shows the true excess energies Q , and finally values of the detection efficiency E_{eff} are listed in table 9.1 on page 63.

The obtained values of the total cross section for the $pp \rightarrow pp\eta'$ reaction are summarized below in table 10.1 and are published in Physical Review Letters [18].

beam momentum P_{beam} [MeV/c]	beam momentum above threshold ΔP_{beam} [MeV/c]	excess energy Q [MeV]	total cross section σ [nb]	statistical error of σ [nb]	systematical error of σ = 14% [nb]
3221.1 ± 1.1	12.8 ± 1.1	4.1 ± 0.4	25.2	3.6	3.5
3217.5 ± 1.1	9.2 ± 1.1	2.9 ± 0.4	12.7	3.2	1.8
3213.5 ± 1.1	5.2 ± 1.1	1.7 ± 0.4	2.9	1.1	0.4
3213.1 ± 1.1	4.8 ± 1.1	1.5 ± 0.4	2.5	0.5	0.4

Table 10.1: Values of the total cross sections for the η' meson production in proton-proton collisions at four excess energies close to threshold.

The overall systematical error amounts to 14%, where 11% comes from the determination of the detection efficiency E_{eff} and 3% from the luminosity measurement.

The obtained values of the total cross section are compared in Figure 10.1 with the recently reported measurements performed at the SATURNE accelerator using the SPES3 spectrometer [20]. A satisfactory agreement in the value of the absolute cross section is observed where the two experiments meet around $Q = 4 \text{ MeV}$. In addition, Figure 10.1 shows the total cross sections for the production of π^0 and η -the remaining two flavour neutral mesons from the lightest pseudoscalar nonet- in proton-proton collisions near threshold.

It is worth noting, that also the total cross section for the $pp \rightarrow pp\eta$ reaction measured at the COSY - 11 facility, indicated by a filled star, agrees well with the results obtained at the CELSIUS and SATURNE accelerators.

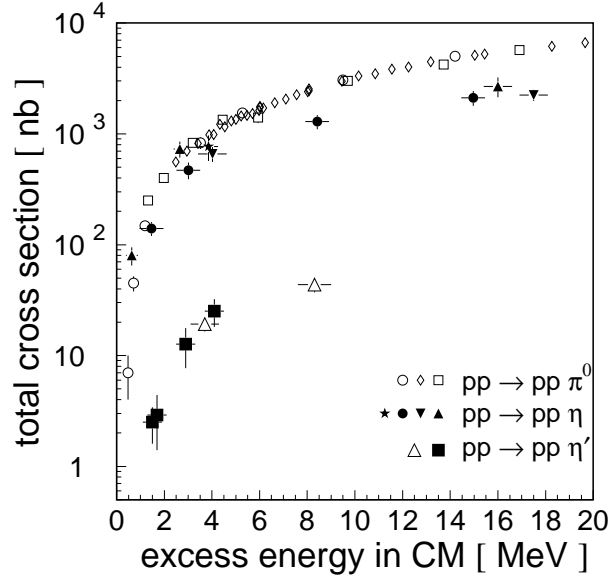


Figure 10.1: Total cross section for the reactions:

$pp \rightarrow pp\pi^0$, $pp \rightarrow pp\eta$, and $pp \rightarrow pp\eta'$ as a function of the excess energy.

$pp \rightarrow pp\pi^0$: CELSIUS [71](open circles), IUCF [70, 69](open diamonds and squares)

$pp \rightarrow pp\eta$: CELSIUS [78](filled circles), SPES3 [20, 138](filled triangles (up)),

PINOT [79](filled triangles (down)), COSY - 11 [139](filled star)

$pp \rightarrow pp\eta'$: this work (filled squares), SPES3 [20](open triangles)

The mesons π^0 and η are produced with rather similar cross sections, whereas the reaction yield for the η' meson is more than one order of magnitude smaller. However, the differences in the total cross section at the same excess energy can not be translated directly to the differences in the production amplitude, since the available phase space at a given excess energy depends on the produced meson mass. Therefore some speculations about the eventual differences in the production mechanisms between the η' meson and π^0 or η ones are left to section 11.4, where the production amplitudes will be derived and compared. This speculations will be preceded by the presentation of the influence of the proton-proton final state interaction on the total cross section energy dependence, and by the comparison of the data with model predictions.

11. Comparison with model predictions

11.1 proton-proton final state interaction

The cross section for the reaction $pp \rightarrow pp\eta'$ can be expressed, as shown in Appendix A (equation A.16), in the following Lorentz invariant form

$$\sigma_{pp \rightarrow pp\eta'} = \frac{\int \text{phase space} \cdot |M_{pp \rightarrow pp\eta'}|^2}{\text{flux factor}} = \frac{\int \prod_{i=1}^{i=3} \frac{d^3 \vec{p}_i}{2E_i} \delta^4\left(p_b + p_T - \sum_{i=1}^{i=3} p_i\right) |M_{pp \rightarrow pp\eta'}|^2}{4(2\pi)^5 \sqrt{(p_b p_T)^2 - m_b^2 m_T^2}}, \quad (11.1)$$

where, the following notation is used:

- $p_b = (E_b, \vec{p}_b)$ - four momentum vector of a beam proton,
- $p_T = (E_T, \vec{p}_T)$ - four momentum vector of a target proton,
- $p_i = (E_i, \vec{p}_i)$, $i=1,2,3$ - four momentum vectors of particles in the exit channel,
- $M_{pp \rightarrow pp\eta'}$ - transition matrix element for the $pp \rightarrow pp\eta'$ reaction.

In analogy with the *Watson-Migdal* approximation [140] for two body processes, it can be assumed that the complete transition amplitude of a production process $M_{pp \rightarrow pp\eta'}$ factorizes approximately as [4, 141]:

$$M_{pp \rightarrow pp\eta'} \approx M_0 \cdot M_{FSI} \quad (11.2)$$

where, M_0 accounts for all possible production processes, and M_{FSI} describes the elastic interaction of protons and η' meson in the exit channel. The proton-proton interaction in the initial channel is not considered close to threshold as this varies slowly with energy and would have little influence on the energy dependence [141].

An exact evaluation of the production amplitude M_0 would require the knowledge of all appropriate coupling constants and the form factors needed for the calculations of the production amplitudes illustrated by the diagrams in Figures 3.3 and 3.4. On the other hand, the exact calculation of the M_{FSI} amplitude, would require the usage of the Faddeev formalism and the knowledge of the proton-proton and proton- η' forces.

Let us, at first assume that the production amplitude M_0 is constant over the entire phase space near threshold, and that only proton-proton elastic scattering takes place in the exit channel.

Sufficiently close to threshold, the amplitude corresponding to the ${}^3P_0 \rightarrow {}^1S_0$ transition in the proton-proton system has a dominant contribution to the $pp \rightarrow pp\eta'$

reaction, as shown in appendix D. That is why it is enough to consider the 1S_0 - wave scattering of the outgoing protons.

These assumptions lead to the following formula for the total cross section, see appendix C (equation C.8):

$$\sigma_{pp \rightarrow pp\eta'}(Q) = \text{const.} \int_0^{q_{max}(Q)} \frac{dq \cdot q^2 \cdot p}{C^4 p^2 + \left(-\frac{1}{a_{pp}} + \frac{b_{pp} \cdot p^2}{2} - \frac{P_{pp} \cdot p^4}{1 + Q_{pp} \cdot p^2} - 2 \cdot p \cdot \eta_c \cdot h(\eta_c) \right)^2}, \quad (11.3)$$

where, $a_{pp} = -7.82 \text{ fm}$ denotes the scattering length for the proton-proton interaction, $b_{pp} = 2.79 \text{ fm}$ indicates the effective range, and $P_{pp} = 0.73 \text{ fm}^3$ and $Q_{pp} = 3.35 \text{ fm}^2$ [142] depict the shape coefficients defined in appendix C. Half of the relative proton-proton momentum is denoted by $p = p(q, q_{max})$, whereas q indicates the meson momentum in the centre-of-mass system, and Q the centre-of-mass excess energy. C^2 stands for the Coulomb penetration factor and η_c and $h(\eta_c)$ -Coulomb parameters- are defined in appendix C.

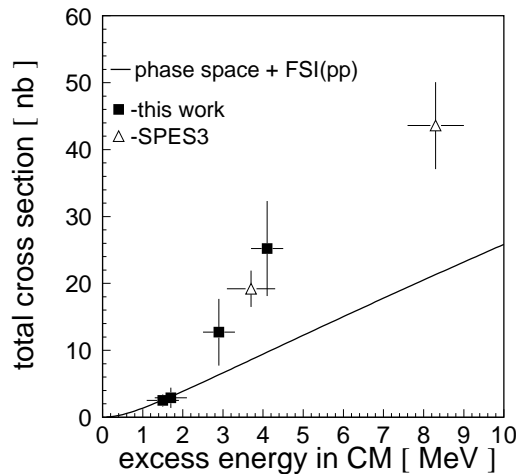


Figure 11.1: Energy dependence of the total cross section as given by the phase space factors and the proton-proton final state interaction (solid line). The experimental values of the total cross section for the $pp \rightarrow pp\eta'$ reaction are indicated by filled squares (this work) and by open triangles (SPES3 [20]). The shown errors take account of both statistical and systematical uncertainties.

The solid line in Figure 11.1 shows the anticipation of equation 11.3 with a value of the coefficient const adjusted to the experimental points at energies lower than $Q = 2 \text{ MeV}$. The discrepancy between the solid line and the experimental points for excess energies larger than $Q = 2 \text{ MeV}$ may reflect the proton- η'

interaction or the variation of the production amplitude M_0 with the excess energy, because in the derivation of equation 11.3 both these possibilities were neglected.

In case of the $pp \rightarrow pp\eta$ reaction, a similar deviation of the energy dependence for the total cross section from the predictions based on the phase space and the proton-proton final state interaction was taken as an evidence for the η -proton interaction [4, 141, 78]. Albeit η -proton interaction is much weaker than the proton-proton one (compare $a_{p\eta} = (0.5 + i0.3) fm$ [4, 143] with $a_{pp} = -7.82 fm$), it becomes important through the interference terms, since the M_{FSI} amplitude is coherent in terms involving the various final pair interactions [4].

Thus, we may speculate that at very low energies the proton- η' interaction is repulsive, and hence caused the suppression of the total cross section very close to threshold. On the other hand, the observed deviation of the experimental points from the solid line may be attributed to the increase of the primary production amplitude with the increasing excess energy. At present, however, we can not prove any of these hypotheses.

11.2 One-pion-exchange model

In the previous section, it was assumed that the production amplitude M_0 is constant but nothing was assumed about its value and hence the absolute value of the total cross section could not be predicted. Now it will be presented how one can deduce the absolute value of the close to threshold total cross section of the $pp \rightarrow pp\eta'$ reaction from the total cross section of the $pp \rightarrow pp\eta$ reaction using the one-pion-exchange model as suggested by the authors of references [20, 144].

In the one-pion-exchange model, it is assumed that the π^0 meson is emitted by one proton and converts to the η' meson on the second one [20, 144].

If the initial proton-proton distortion and the final proton- η' interaction are neglected then this model gives the following form for the S-wave contribution (in the exit channel) to the total cross section of the $pp \rightarrow pp\eta'$ reaction [20]:

$$\sigma_{pp \rightarrow pp\eta'}(Q) = A \cdot \frac{(m_p + m_{\eta'})^2}{(2m_p + m_{\eta'})^{5/2}} \cdot \frac{\sqrt{m_{\eta'}}}{(m_p m_{\eta'} + m_\pi^2)^2} \cdot |f(\pi^0 p \rightarrow p\eta')|^2 \cdot F(Q), \quad (11.4)$$

where, m_p , $m_{\eta'}$ and m_π denote the proton, η' , and π masses, respectively, $|f(\pi^0 p \rightarrow p\eta')|^2 = 10 \mu b/sr$ [20] stands for the spin average of the square of the $\pi^0 p \rightarrow p\eta'$ amplitude, and the function $F(Q)$ describes approximately the effect of the proton-proton final state interaction [145]:

$$F(Q) = \epsilon \left(\frac{Q}{\epsilon} \right)^2 \left(1 + \sqrt{1 + \frac{Q}{\epsilon}} \right)^{-2}, \quad (11.5)$$

where, including Coulomb distortion, $\epsilon \approx 0.45 MeV$. This parametrization of the proton-proton final state interaction gives within the accuracy of a few per cent the

same result as the exact formula of equation 11.3. This allows, however, to infer that the influence of the proton-proton final state interaction on the production cross section is fairly independent of the produced meson mass, and depends only on the centre-of-mass excess energy [146].

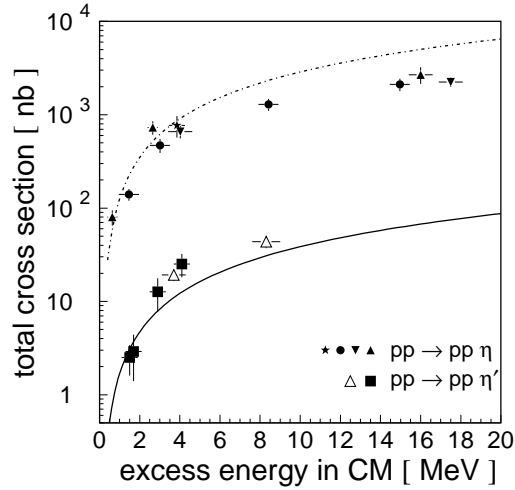


Figure 11.2: Total cross section for the $pp \rightarrow pp\eta$ and $pp \rightarrow pp\eta'$ reactions as a function of the excess energy Q .

$pp \rightarrow pp\eta$: CELSIUS [78](filled circles), SPES3 [20, 138](filled triangles (up)), PINOT [79](filled triangles (down)), COSY - 11 [139](filled star)

$pp \rightarrow pp\eta'$: this work (filled squares), SPES3 [20](open triangles)

The errors shown for the $pp \rightarrow pp\eta'$ points take account of both statistical and systematic uncertainties, whereas in case of the $pp \rightarrow pp\eta$ reaction only statistical errors are indicated.

The value of the overall factor A in equation 11.4 does not depend on the η' meson properties [20], and therefore it should be the same for the counterpart of equation 11.4 describing the total cross section of the $pp \rightarrow pp\eta$ reaction. Thus, knowing the threshold value for the $|f(\pi^0 p \rightarrow p\eta)|^2 = 365 \mu b/sr$, and the total cross section for the $pp \rightarrow pp\eta$ reaction it is possible to calculate the value of the factor A , and hence to predict the total cross section for the $pp \rightarrow pp\eta'$ reaction, since the $|f(\pi^0 p \rightarrow p\eta')|^2$ is known, and since the influence of the proton-proton interaction depends approximately only on the value of Q .

The total cross section for the $pp \rightarrow pp\eta$ reaction, obtained from the one-pion-exchange model, with the value of A adjusted to fit the lowest energy points of η production, is shown by the dashed line in Figure 11.2. The application of the same value of A in equation 11.4 for the calculation of the $pp \rightarrow pp\eta'$ total cross section, results in the solid line.

The predicted absolute values of the total cross section for the $pp \rightarrow pp\eta'$ reaction agree at the lowest energy points. This agreement shows that the relative close to threshold production of the η and η' mesons is comparable in the pion-proton and proton-proton collisions. However, we are still not able to infer anything about the relative contribution of a different production mechanisms of the $pp \rightarrow pp\eta'$ reaction.

Since in this parametrization the energy dependence of the total cross section is determined, as in the previous section, by the phase space and the proton-proton final state interaction one can explicitly see the deviation between the predictions and the data which is explained by the attractive ηpp interaction [78, 20, 4, 141]. One sees also, as in Figure 11.1, that the energy dependence of the production amplitude as given by the phase space and proton-proton final state interaction is not enough to describe the $pp \rightarrow pp\eta'$ reaction cross section.

11.3 Born-term - upper limit for the $pp\eta'$ coupling constant

The production amplitude M_0 can be calculated only if the appropriate coupling constants and the reaction mechanisms are known. Some possible production mechanisms are discussed in section 3.2 (see Figures 3.3 and 3.4), but their contributions are not evaluated yet. The only, till now, performed calculations take account of the direct radiation of the η' meson by protons, as illustrated in Figure 3.3a. The calculations were performed in the effective Lagrangian approach (see section 3.3). The initial and final proton-proton interactions were included as given by the folded-diagram nucleon-nucleon potential (OBEPF) [97].

It is not possible, however, to define the absolute contribution from the direct production since the value of the coupling constant $g_{\eta'pp}$ is not established. There exist some contradictory predictions, discussed in section 3.3, which implies that $g_{\eta'pp}$ amounts to about five or that $g_{\eta'pp}$ is equal to $2.48_{-0.65}^{+0.59}$ or that $g_{\eta'pp}$ is smaller than 1.

Since, the $g_{\eta'pp}$ coupling constant is the only free parameter in these calculations it can be adjusted to fit the experimental data. Figure 11.3 compares the result of the calculations with the experimental data, where the value of coupling constant $g_{\eta'pp}$ was taken to be 2.2.

With the assumption that the production amplitudes from the heavy meson exchange (Figure 3.3c) and other possible mechanisms have the same sign as the amplitude of the direct term, the value $g_{\eta'pp} = 2.2$ can be taken as an upper limit for the $g_{\eta'pp}$ coupling constant. This result is consistent with the predictions of the dispersion method and the calculations based on the quark contribution to the proton spin, see section 3.3.

The assumption about the signs of the amplitudes is plausible, since for example, the positive interference between direct and heavy meson production was

found in case of the $pp \rightarrow pp\pi^0$ reaction [72].

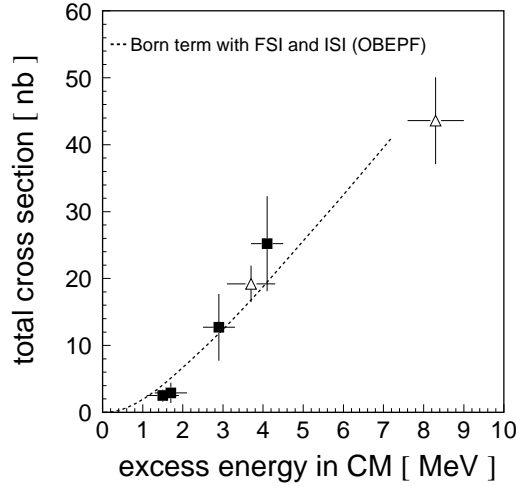


Figure 11.3: Total cross section for the $pp \rightarrow pp\eta'$ reactions as a function of excess energy Q . The dashed curve presents the result of the calculation where only the direct production was considered. Experimental points are taken from: this work (filled squares), and SPES3 [20](open triangles).

11.4 Comparison of the production amplitudes for the $pp \rightarrow pp\pi^0$, $pp \rightarrow pp\eta$, and $pp \rightarrow pp\eta'$ reactions

If we assume that the primary production amplitude does not change with the excess energy, and that only the proton-proton interaction is present in the exit channel we can calculate M_0 according to the following equation:

$$|M_0| = \sqrt{\frac{\text{flux factor} \cdot \sigma_{pp \rightarrow pp\eta'}}{\int \text{phase space} \cdot M_{FSI}^2}} = \sqrt{\frac{\sigma_{pp \rightarrow pp\eta'} \cdot 4(2\pi)^5 \cdot \sqrt{(p_b p_T)^2 - m_b^2 m_T^2}}{\int \prod_{i=1}^{i=3} \frac{d^3 \vec{p}_i}{2E_i} \delta^4\left(p_b + p_T - \sum_{i=1}^{i=3} p_i\right) |M_{pp \rightarrow pp}|^2}}, \quad (11.6)$$

for which some integration were performed in appendix C in order to enable the numerical calculation. The meaning of parameters is described in section 11.1, particularly $M_{pp \rightarrow pp}$ denotes the proton-proton scattering amplitude. According to this equation and the experimental values of the total cross section one can evaluate the modulus of the M_0 amplitude and verify whether it is really constant

as was assumed for its derivation. A deviation from a constant would reflect a proton- η' interaction or the variation of $|M_0|$.

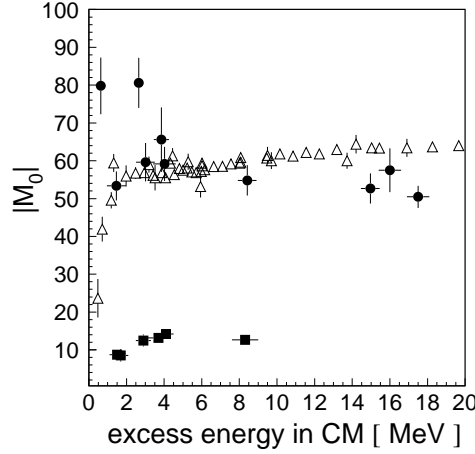


Figure 11.4: Modulus of the dimensionless primary production amplitude M_0 as defined in equation 11.6. The symbols show the results extracted from the experimental data for the reactions $pp \rightarrow pp\pi^0$ (open triangles) [71, 70, 69], $pp \rightarrow pp\eta$ (filled circles) [78, 20, 138, 79, 139], and $pp \rightarrow pp\eta'$ (filled squares) - data from this work and reference [20].

Figure 11.4 compares the extracted absolute values for the modulus of amplitudes for the near to threshold production of the π^0 (triangles), η (circles) and η' (squares) mesons. It can be seen that $|M_0|$ is indeed fairly constant for excess energies larger than 3 MeV for all these reactions. Whereby very close to threshold it decreases rapidly for the pion production with the similar tendency for the η' , whereas in case of the η mesons it increases.

Thus completing the conclusions drawn in the previous sections, the behaviour of the extracted $|M_0|$ can be attributed to the attractive interaction of the proton-eta and repulsive interaction of the proton-pion and proton- η' or to the actual variation of the primary production amplitude very close to the reaction threshold.

The large difference between the absolute values of the obtained modulus of the production amplitude for η and η' mesons, may suggest that the production mechanisms for these mesons are different. And since it is known that the η is produced via the excitation of the baryonic resonance, thus probably it is not the case for the η' production.

12. Conclusion and perspectives

For the first time the total cross section for the production of the η' meson has been measured near the kinematical threshold. The experiment has been carried out at the COSY accelerator using the internal beam and the COSY-11 facility, which allows for the detection of the final protons, whereas the η' meson is identified by means of the missing mass techniques.

The values evaluated for the total cross section, at the centre-of-mass excess energy range between 1.5 MeV and 4.1 MeV , are about a factor of 50 less than the corresponding values for the η or π^0 meson production at the same excess energies. The obtained results are consistent with the recently reported measurements performed at the SATURNE accelerator at the centre-of-mass excess energies of 3.7 MeV and 8.3 MeV [20].

It would be very interesting to evaluate the production mechanisms, and especially to establish the contributions to the production process from the meson-exchange current and from the fusion of gluons emitted from the colliding protons. An answer to this question requires and “deserves a dedicated theoretical study” [5]. Unfortunately, at present only a simplest possibility of a direct emission of the η' meson from the colliding protons was studied theoretically and other more complicated production mechanisms are not evaluated so far.

The comparison of the data with the results of the calculations based on the effective Lagrangian approach, where only a direct production mechanism has been considered, yields an upper limit for the $\eta'pp$ coupling constant to be $g_{\eta'pp} < 2.2$, provided that the assumption of the signs of other possible amplitudes are correct. This result is compatible with the estimation based on the quark contribution to the proton spin and with the determination based on the dispersion method, see section 3.3. It would be interesting now to calculate the contribution to the total cross section from heavy mesons exchange and other possible terms. The experimental determination of the coupling constant is very important since this quantity, in principle, comprises the information of the meson structure, which in case of the η' is not well established as discussed in chapter 2. Especially interesting would be to determine both $g_{\eta pp}$ and $g_{\eta' pp}$ coupling constants, which for example could verify equation 3.3 derived in section 3.3.

It is not possible at present to deduce univocally whether the production of the η' meson in the proton-proton collision is mediated by a baryonic resonance. Till now, the experimentally measured values of the total cross sections for the $pp \rightarrow pp\eta'$ reaction cover only a small range of excess energies and can not reveal the enhancement in the energy dependence of the total cross section from the probable excitation of the much broader predicted resonances. The absolute value of the total cross section or the absolute value of the derived production amplitude

comprises this information, however, again at the present stage of the theory of the η' production any quantitative conclusions are not possible. One can only naively speculate that the large difference in the primary production amplitudes between the η and η' suggests that the η' primary production process is nonresonant, since close to threshold the η meson is produced predominantly through the excitation of the $S_{11}(1535)$ resonance [4, 3, 2, 20].

The planned theoretical investigations, devoted to the understanding and evaluation of the production by the meson-exchange currents may give an answer to these questions.

The analysis of the energy dependence of the total cross section suggests that either the primary production amplitude is not constant and decreases very close to threshold or that the proton- η' interaction has a repulsive character. However, for the quantitative conclusions still more theoretical investigations are needed.

The obtained results encouraged to continue the investigation in order to establish the excitation function more precisely and in a larger excess energy range. Further measurements were already performed at seven excess energies ranging between $Q = 3 \text{ MeV}$ and $Q = 15 \text{ MeV}$ with about five times higher statistics than the present measurements per energy point and with at least two times smaller beam momentum spread due to the usage of the stochastically cooled beam.

In the near future, measurements at only one or two excess energies will be carried out, in order to investigate the η' -proton interaction. It is planned to take enough data to fill a Dalitz plot and to perform an analysis which would give the correlation between the scattering length and the effective range for the η' -proton potential. This will be performed by comparing the experimental Dalitz plot with the ones obtained according to phase-space and to the assumed η' -proton interaction. This method was proven to be useful in the investigations of the Λ -proton interaction [147]. The data with high statistics will enable also a study of the angular distribution of the produced η' mesons.

Further plans concern the investigation of the momentum correlation of the outgoing protons, which should deliver information about the size of the interaction region and hence about the production mechanism [148].

A neutron detector available since last year at the COSY-11 facility, which was designed by the author of this thesis, enables also the measurement of the η' meson production in the $pd \rightarrow ppn\eta'$ reaction, which together with planned studies of the $pd \rightarrow pd\eta'$ and $pd \rightarrow {}^3\text{He}\eta'$ reactions will enable the investigations of the η' meson production mechanism in the proton-neutron scattering. The investigation of the η' production via these reactions is very scarce. There exists only one value for the near threshold total cross section of the $pd \rightarrow {}^3\text{He}\eta'$ reaction measured at the SATURNE accelerator [11], and other reactions were not studied so far. It is worth noting that the studies of the η' production in proton-deuteron collisions are also planned at the CELSIUS accelerator [149].

PART IV
APPENDICES

A. Formula for the cross section

The cross section can be expressed as:

$$\sigma = \frac{\omega}{|v_b| \rho_b \rho_T} \quad (\text{A.1})$$

where

ω is the reaction rate per unit volume,

ρ_b - number of the beam particles per unit volume,

$|v_b|$ - velocity of the beam particle,

ρ_T - number of the target particles per unit volume.

Now we will consider the reaction $pp \rightarrow pp\eta'$ using the following notations:

$p_b = (E_b, \vec{p}_b)$ four momentum vector of a beam proton,

$p_T = (E_T, \vec{p}_T)$ four momentum vector of a target proton,

$p_i = (E_i, \vec{p}_i)$, $i=1,2,3$ four momentum vectors of particles in the exit channel.

Considering a moving particle as a plane wave function $\phi = Ne^{-ipx}$ it can be shown that the probability density of finding this particle in a unit volume is given by [150]

$$\rho = 2 N^2 E \quad (\text{A.2})$$

The normalization condition

$$\int_V \rho d^3x = 1 \Leftrightarrow N^2 = \frac{1}{2VE} \quad (\text{A.3})$$

and equation A.2 yield:

$$|v_b| \rho_b \rho_T = |v_b| \frac{1}{V^2} \quad (\text{A.4})$$

In order to describe the development in time of a given state $\Phi(t)$ a so called S-matrix is introduced as follows:

$$\Phi(+\infty) = \hat{S}\Phi(-\infty) \quad (\text{A.5})$$

The probability amplitude of the transition from the initial state Φ_i to the final state Φ_f is given by a matrix element $S_{fi} = \langle \Phi_f | \hat{S} | \Phi_i \rangle$. If $\hat{S} = \mathbf{1}$ then there is no reaction, i.e. initial and final states are the same. Therefore one introduces a T-matrix describing the actual reaction, which is defined as follows:

$$S_{fi} = \delta_{fi} - i(2\pi)^4 \delta^4(p_f - p_i) T_{fi} \quad (\text{A.6})$$

Consequently the transition probability W_{fi} is given by

$$W_{fi} = |S_{fi}|^2 \stackrel{f \neq i}{=} (2\pi)^8 \left(\delta^4(p_f - p_i) \right)^2 |T_{fi}|^2 = (2\pi)^4 \delta^4(p_f - p_i) |T_{fi}|^2 Vt, \quad (\text{A.7})$$

where, V denotes the total volume of space and t the total time in which the interaction takes place. Dividing W_{fi} by V and t one obtains the transition probability per unit time and unit volume.

$$\omega_{fi} = \frac{W_{fi}}{Vt} = (2\pi)^4 \delta^4(p_f - p_i) |T_{fi}|^2 \quad (\text{A.8})$$

If we are not interested in the momenta of the outgoing particles then the $\omega_{pp \rightarrow pp\eta'}$ -reaction rate per unit volume- for the $pp \rightarrow pp\eta'$ reaction can be calculated by integrating ω_{fi} over all possible momentum values in the exit channel. Thus, changing T_{fi} into $T_{pp \rightarrow pp\eta'}$ we get:

$$\omega_{pp \rightarrow pp\eta'} = \int \prod_{i=1}^{i=3} \frac{d^3 \vec{p}_i V}{(2\pi)^3} (2\pi)^4 \delta^3(\vec{p}_b + \vec{p}_T - \sum_{i=1}^{i=3} \vec{p}_i) \delta(E_b + E_T - \sum_{i=1}^{i=3} E_i) |T_{pp \rightarrow pp\eta'}|^2, \quad (\text{A.9})$$

where

$$\prod_{i=1}^{i=3} \frac{d^3 \vec{p}_i V}{(2\pi)^3} \quad (\text{A.10})$$

is the number of final states in the phase space volume. Substitution of ω in the equation A.1 yields:

$$\sigma_{pp \rightarrow pp\eta'} = \frac{V^2 \int \prod_{i=1}^{i=3} \frac{d^3 \vec{p}_i V}{(2\pi)^3} (2\pi)^4 \delta^3(\vec{p}_b + \vec{p}_T - \sum_{i=1}^{i=3} \vec{p}_i) \delta(E_b + E_T - \sum_{i=1}^{i=3} E_i) |T_{pp \rightarrow pp\eta'}|^2}{|v_b|} \quad (\text{A.11})$$

Defining the square of the Lorentz invariant transition matrix element as ¹:

$$|M_{pp \rightarrow pp\eta'}|^2 = |T_{pp \rightarrow pp\eta'}|^2 2V E_T 2V E_b 2V E_1 2V E_2 2V E_3 \quad (\text{A.14})$$

and applying the relation:

$$|v_b| E_b E_T = [(p_b \cdot p_T)^2 - m_b^2 m_T^2]^{\frac{1}{2}}, \quad (\text{A.15})$$

the following expression of the cross section in a Lorentz invariant form is obtained:

$$\sigma_{pp \rightarrow pp\eta'} = \frac{\int \prod_{i=1}^{i=3} \frac{d^3 \vec{p}_i}{2E_i} \delta^3(\vec{p}_b + \vec{p}_T - \sum_{i=1}^{i=3} \vec{p}_i) \delta(E_b + E_T - \sum_{i=1}^{i=3} E_i) |M_{pp \rightarrow pp\eta'}|^2}{4(2\pi)^5 [(p_b \cdot p_T)^2 - m_b^2 m_T^2]^{\frac{1}{2}}}, \quad (\text{A.16})$$

¹Note that, for example, Bjorken and Drell [151] use another convention. They in the fermion case multiply $|T|^2$ by a factor of $\frac{EV}{M}$ using the following normalization of Dirac spinors

$$\bar{u}(p, s') u(p, s) = \delta_{s, s'}, \quad (\text{A.12})$$

whereas multiplying $|T|^2$ by a factor $2VE$ implies that the Dirac spinors must be normalized as:

$$\bar{u}(p, s') u(p, s) = 2M \delta_{s, s'} \quad (\text{A.13})$$

where expression $4(2\pi)^5 [(p_b \cdot p_T)^2 - m_b^2 m_T^2]^{\frac{1}{2}}$ often denoted by \mathbf{F} [122] is called the *flux factor* and

$$\int \prod_{i=1}^{i=3} \frac{d^3 \vec{p}_i}{2E_i} \delta^3(\vec{p}_b + \vec{p}_T - \sum_{i=1}^{i=3} \vec{p}_i) \delta(E_b + E_T - \sum_{i=1}^{i=3} E_i) |M_{pp \rightarrow pp\eta'}|^2, \quad (\text{A.17})$$

is sometimes denoted by $I_3(s)$ [122]. Using this notation, the cross section may be written in a compact form as:

$$\sigma = \frac{\mathbf{I}_3(\mathbf{s})}{\mathbf{F}} \quad (\text{A.18})$$

where \mathbf{s} is defined as $(p_b + p_T)^2$ and \sqrt{s} is equal to the total energy in the centre-of-mass system.

B. Phase space factors

In this part the integration of equation A.16 will be performed, in order to express $\sigma_{pp \rightarrow pp\eta'}$ in terms of the maximum η' momentum in the centre-of-mass system.

In the centre-of-mass system equation A.16 has the following form:

$$\sigma_{pp \rightarrow pp\eta'} = \frac{I_3(s)}{F} = \frac{\int \prod_{i=1}^{i=3} \frac{d^3 p_i^*}{2\sqrt{m_i^2 + (\vec{p}_i^*)^2}} \delta^3(\sum_{i=1}^{i=3} \vec{p}_i^*) \delta(E_i^* - E_f^*) |M_{pp \rightarrow pp\eta'}|^2}{2 (2\pi)^5 [s (s - 4 m_p^2)]^{\frac{1}{2}}}, \quad (\text{B.1})$$

where,

* - indicates a centre-of-mass system,

E_i^*, E_f^* - total energy in the entrance and exit channel respectively,

\sqrt{s} - total energy in the centre-of-mass frame, and

m_p - stands for the proton mass.

The total energy E_i^* of the initial channel is equal to the sum of the protons kinetic energies T_i^* and their masses:

$$E_i^* = T_i^* + 2 m_p, \quad (\text{B.2})$$

and in the exit channel the total energy E_f^* is equal to:

$$E_f^* = T_f^* + 2 m_p + m_{\eta'}, \quad (\text{B.3})$$

where, T_f^* is the summed kinetic energy in the centre-of-mass in the exit channel and $m_{\eta'}$ is the mass of the produced η' . The $\delta(E_i^* - E_f^*)$ can be substituted by $\delta(T_i^* - m_{\eta'}^* - T_f^*)$, and since the centre-of-mass kinetic energy of the outgoing particles is small in comparison with their masses one can substitute also:

$$\begin{aligned} \sqrt{s} & \text{ by } 2 m_p + m_{\eta'}, \\ \sqrt{m_i^2 + (\vec{p}_i^*)^2} & \text{ by } m_i, \quad \text{and} \\ T_f^* & \text{ by } \sum_{i=1}^{i=3} \frac{(\vec{p}_i^*)^2}{2 m_i}, \end{aligned}$$

which gives:

$$\sigma_{pp \rightarrow pp\eta'} = \frac{\frac{1}{8 m_p^2 m_{\eta'}} \int \prod_{i=1}^{i=3} d^3 p_i^* \delta^3(\sum_{i=1}^{i=3} \vec{p}_i^*) \delta(T_i^* - m_{\eta'}^* - \sum_{j=1}^{j=3} \frac{p_j^{*2}}{2 m_j}) |M_{pp \rightarrow pp\eta'}|^2}{2 (2\pi)^5 (2 m_p + m_{\eta'}) ((2 m_p + m_{\eta'})^2 - 4 m_p^2)^{\frac{1}{2}}} \quad (\text{B.4})$$

Making transformation into Jacobi coordinates system (see Appendix E) one obtains:

$$\sigma_{pp \rightarrow pp\eta'} = \frac{\int d^3\vec{P} d^3\vec{p} d^3\vec{q} \delta(\vec{P}) \delta(T_i^* - m_{\eta'} - \frac{\vec{P}^2}{2M} - \frac{\vec{p}^2}{2\mu} - \frac{\vec{q}^2}{2\nu}) |M_{pp \rightarrow pp\eta'}|^2}{16 (2\pi)^5 (2m_p + m_{\eta'}) \sqrt{m_{\eta'}^2 + 4m_p m_{\eta'}} m_p^2 m_{\eta'}}, \quad (\text{B.5})$$

where, introduced quantities have the following meaning:

\vec{P} - total momentum in the centre-of-mass system,

\vec{p} - proton momentum in the two-protons system,

\vec{q} - η' meson momentum in the reaction centre-of-mass system,

$M = 2m_p + m_{\eta'}$

$\mu = \frac{m_p}{2}$ - reduced mass of the proton-proton system,

$\nu = \frac{2m_p m_{\eta'}}{2m_p + m_{\eta'}}$ - reduced mass of the η' - two-protons system.

Since the transition matrix element $M_{pp \rightarrow pp\eta'}$ is obviously independent of the motion of the centre-of-mass, integration over \vec{P} yields:

$$\sigma_{pp \rightarrow pp\eta'} = \frac{\int d^3\vec{p} d^3\vec{q} \delta(T_i^* - m_{\eta'} - \frac{\vec{p}^2}{2\mu} - \frac{\vec{q}^2}{2\nu}) |M_{pp \rightarrow pp\eta'}|^2}{16 (2\pi)^5 (2m_p + m_{\eta'}) \sqrt{m_{\eta'}^2 + 4m_p m_{\eta'}} m_p^2 m_{\eta'}}. \quad (\text{B.6})$$

Making transformation into the spherical coordinates of \vec{p} and \vec{q} and denoting $|\vec{p}|$ by p and $|\vec{q}|$ by q one gets:

$$\sigma_{pp \rightarrow pp\eta'} = \frac{\int dp dq d\Omega_p d\Omega_q p^2 q^2 \delta(T_i^* - m_{\eta'} - \frac{p^2}{2\mu} - \frac{q^2}{2\nu}) |M_{pp \rightarrow pp\eta'}|^2}{16 (2\pi)^5 (2m_p + m_{\eta'}) \sqrt{m_{\eta'}^2 + 4m_p m_{\eta'}} m_p^2 m_{\eta'}} \quad (\text{B.7})$$

Assuming that $|M_{pp \rightarrow pp\eta'}|^2$ does not depend on the orientation of the η' momentum in the centre-of-mass system and on the relative protons momentum, an integration over all angles gives:

$$\sigma_{pp \rightarrow pp\eta'} = \frac{4\pi \cdot 4\pi \cdot \int dp dq p^2 q^2 \delta(T_i^* - m_{\eta'} - \frac{p^2}{2\mu} - \frac{q^2}{2\nu}) |M_{pp \rightarrow pp\eta'}|^2}{16 (2\pi)^5 (2m_p + m_{\eta'}) \sqrt{m_{\eta'}^2 + 4m_p m_{\eta'}} m_p^2 m_{\eta'}} \quad (\text{B.8})$$

The δ function in the above equation implies that the following equation must be fulfilled:

$$T_i^* - m_{\eta'} - \frac{p^2}{2\mu} - \frac{q^2}{2\nu} = 0, \quad (\text{B.9})$$

where, for a given T_i^* , q has a maximum value if p is equal to zero. Thus, putting $p = 0$ one obtains:

$$q_{max}^2 = 2\nu (T_i^* - m_{\eta'}) \quad (\text{B.10})$$

This implies that equation B.8 can be rewritten as follows:

$$\sigma_{pp \rightarrow pp\eta'} = \frac{\int dp dq p^2 q^2 \delta\left(\frac{q_{max}^2 - q^2}{2\nu} - \frac{p^2}{2\mu}\right) |M_{pp \rightarrow pp\eta'}|^2}{4 (2\pi)^3 (2m_p + m_{\eta'}) \sqrt{m_{\eta'}^2 + 4m_p m_{\eta'}} m_p^2 m_{\eta'}} \quad (\text{B.11})$$

In order to integrate over p the following theorem will be used:

$$\delta(f(x)) = \sum_i \frac{1}{|f'(x_i)|} \delta(x - x_i), \text{ where } f(x_i) = 0. \quad (\text{B.12})$$

In our case

$$f(p) = \frac{q_{max}^2 - q^2}{2\nu} - \frac{p^2}{2\mu},$$

and hence

$$f(p) = 0 \text{ for } p = \sqrt{\frac{\mu}{\nu}(q_{max}^2 - q^2)},$$

and

$$|f'(p)| = \frac{p}{\mu} = \frac{2p}{m_p}.$$

Applying this theorem to equation B.11 one obtains:

$$\sigma_{pp \rightarrow pp\eta'} = \frac{\int dp dq p q^2 \delta\left(p - \sqrt{\frac{\mu}{\nu}(q_{max}^2 - q^2)}\right) |M_{pp \rightarrow pp\eta'}|^2}{8 (2\pi)^3 (2m_p + m_{\eta'}) \sqrt{m_{\eta'}^2 + 4m_p m_{\eta'}} m_p m_{\eta'}}, \quad (\text{B.13})$$

which after the substitution of $\frac{\mu}{\nu}$ by $\frac{m_{\eta'} + 2m_p}{4m_{\eta'}}$ yields:

$$\sigma_{pp \rightarrow pp\eta'} = \frac{\int dp dq p q^2 \delta\left(p - \sqrt{\frac{m_{\eta'} + 2m_p}{4m_{\eta'}}(q_{max}^2 - q^2)}\right) |M_{pp \rightarrow pp\eta'}|^2}{8 (2\pi)^3 (2m_p + m_{\eta'}) \sqrt{m_{\eta'}^2 + 4m_p m_{\eta'}} m_p m_{\eta'}} \quad (\text{B.14})$$

Now the integration over p can be easily performed, provided that $M_{pp \rightarrow pp\eta'}$ is independent of p, giving:

$$\sigma_{pp \rightarrow pp\eta'} = \frac{\int_0^{q_{max}} dq q^2 \sqrt{\frac{m_{\eta'} + 2m_p}{4m_{\eta'}}(q_{max}^2 - q^2)} |M_{pp \rightarrow pp\eta'}|^2}{8 (2\pi)^3 (2m_p + m_{\eta'}) \sqrt{m_{\eta'}^2 + 4m_{\eta'} m_p} m_p m_{\eta'}} \quad (\text{B.15})$$

Furthermore, assuming that $|M_{pp \rightarrow pp\eta'}|^2$ is independent of q one gets:

$$\sigma_{pp \rightarrow pp\eta'} = \frac{\sqrt{m_{\eta'} + 2m_p} |M_{pp \rightarrow pp\eta'}|^2 \int_0^{q_{max}} dq q^2 \sqrt{q_{max}^2 - q^2}}{16 (2\pi)^3 (2m_p + m_{\eta'}) \sqrt{m_{\eta'}^2 + 4m_{\eta'} m_p} m_p m_{\eta'}^{\frac{3}{2}}}.$$

Substitution of q by $x \cdot q_{max}$, with $x \in [0,1]$ gives:

$$\begin{aligned} \sigma_{pp \rightarrow pp\eta'} &= \frac{\sqrt{m_{\eta'} + 2m_p} |M_{pp \rightarrow pp\eta'}|^2 q_{max}^4 \int_0^1 dx x^2 \sqrt{1-x^2}}{16 (2\pi)^3 (2m_p + m_{\eta'}) \sqrt{m_{\eta'}^2 + 4m_{\eta'}m_p} m_p m_{\eta'}^{\frac{3}{2}}} = \\ &= \frac{\sqrt{m_{\eta'} + 2m_p} |M_{pp \rightarrow pp\eta'}|^2 q_{max}^4 \frac{\pi}{16}}{16 (2\pi)^3 (2m_p + m_{\eta'}) \sqrt{m_{\eta'}^2 + 4m_{\eta'}m_p} m_p m_{\eta'}^{\frac{3}{2}}}. \end{aligned} \quad (\text{B.16})$$

It means that the total cross section governed by the phase space factors would be proportional to the fourth power of the maximum η' momentum in the centre-of-mass system q_{max}^4 , or to the second power of the excess energy Q^2 , since in the nonrelativistic limit $Q \sim q_{max}^2$ (see equation F.1 in appendix F).

C. Proton-proton final state interaction

The proton-proton scattering amplitude for the relative angular momentum $l=0$ is expressed by [152]:

$$M_{pp \rightarrow pp} = \frac{e^{i\delta_{pp}} \cdot \sin\delta_{pp}}{C^2 \cdot p}. \quad (\text{C.1})$$

In this equation p denotes a momentum of either proton in the centre-of-mass of the collision partners, and δ_{pp} indicates the phase shift. The Coulomb penetration factor C^2 in the denominator is due to the Coulomb interaction between two protons. This factor can be defined as a ratio of “the probability of finding two protons close together to the probability of finding two uncharged particles together, other things being equal” [153, 154]:

$$C^2 = \frac{2\pi\eta_c}{e^{2\pi\eta_c} - 1}, \quad (\text{C.2})$$

where, η_c denotes the so-called relativistic Coulomb parameter $\eta_c = \alpha/v$, with α being the fine structure constant and v being the proton velocity in the rest system of the other proton. The factor C^2 is always less than unity due to the Coulomb repulsion between protons. At high energies, where C^2 is close to unity the nuclear scattering will be predominant, and for the very low energies nuclear and Coulomb scattering are expected to compete. The limit is expected approximately at 0.8 MeV of the proton energy in the rest system of the other proton, where $C^2 = 0.5$ [153]¹.

The phase shift δ_{pp} in equation C.1 is obtained from the modified *Cini-Fubini-Stanghellini* formula, with *Wong-Noyes* Coulomb correction [155]:

$$C^2 \cdot p \cdot \text{ctg}\delta_{pp} + 2 \cdot p \cdot \eta_c \cdot h(\eta_c) = -\frac{1}{a_{pp}} + \frac{1}{2} \cdot b_{pp} \cdot p^2 - \frac{P_{pp} \cdot p^4}{1 + Q_{pp} \cdot p^2}, \quad (\text{C.3})$$

where, $h(\eta_c) = -\ln(\eta_c) - 0.57721 + \eta_c^2 \cdot \sum_{n=1}^{\infty} \frac{1}{n \cdot (n^2 + \eta_c^2)}$ [153]. Phenomenological quantities $a_{pp} = -7.8 \text{ fm}$ and $b_{pp} = 2.8 \text{ fm}$ denote the scattering length and the effective range, respectively. The parameters $P_{pp} = 0.73 \text{ fm}^3$ and $Q_{pp} = 3.35 \text{ fm}^2$ are not phenomenological constants, they are related to the detailed shape of the nuclear potential as obtained from the OPE model. P_{pp} and Q_{pp} were computed

¹In the case of the $pp \rightarrow pp\eta'$ reaction maximum possible energy of a proton seen from another proton is equal to 0.8 MeV already at $1.3 \text{ MeV}/c$ of the beam momentum above threshold. Hence, below this energy Coulomb interaction is important in the proton-proton final state interaction.

from the pion-nucleon coupling constant and the pion mass according to formulas from reference [142].

Equations C.1 and C.3 yields:

$$|M_{pp \rightarrow pp}|^2 = \frac{1}{C^4 \cdot p^2 + \left(-\frac{1}{a_{pp}} + \frac{b_{pp} \cdot p^2}{2} - \frac{P_{pp} \cdot p^4}{1 + Q_{pp} \cdot p^2} - 2 \cdot p \cdot \eta_c \cdot h(\eta_c) \right)^2} \quad (\text{C.4})$$

Figure C.1a shows the square of the proton proton scattering amplitude as obtained from equation C.4. Figure C.1b compares the distributions of the relative momentum of the outgoing protons from the $pp \rightarrow pp\eta'$ reaction, calculated for a beam momentum of 15 MeV/c above threshold, with and without the inclusion of the proton-proton final state interaction. The calculation shows that the attractive nuclear proton-proton interactions modifies the relative momentum spectrum such that the enhancement at low relative momenta is observed in comparison to the pure phase space distribution.

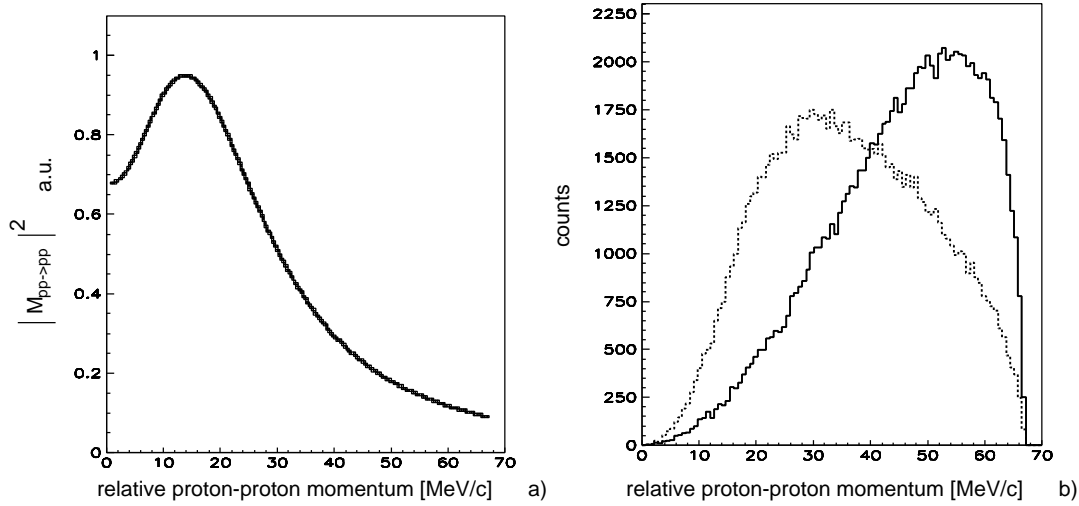


Figure C.1: (a) Square of the proton-proton scattering amplitude as a function of the centre-of-mass momentum. (b) Relative proton-proton momentum distribution for the $pp \rightarrow pp\eta'$ reaction as given by the phase-space without proton-proton FSI - solid line, and with proton-proton FSI - dotted line.

It is shown in appendix B in equation B.14 that the total cross section for the $pp \rightarrow pp\eta'$ reaction can be expressed as:

$$\sigma_{pp \rightarrow pp\eta'} = \frac{\int dp dq p q^2 \delta\left(p - \sqrt{\frac{m_{\eta'} + 2m_p}{4m_{\eta'}} (q_{max}^2 - q^2)}\right) |M_{pp \rightarrow pp\eta'}|^2}{8 (2\pi)^3 (2m_p + m_{\eta'}) \sqrt{m_{\eta'}^2 + 4m_p m_{\eta'}} m_p m_{\eta'}}, \quad (\text{C.5})$$

where, the Jacobi momenta p and q denote a momentum of either proton in the proton-proton centre-of-mass, and the η' momentum in the reaction centre-of-mass, respectively. $M_{pp \rightarrow pp\eta'}$ indicates the overall production amplitude, which can be factorize according to the Watson-Migdal approximation as [140]²:

$$|M_{pp \rightarrow pp\eta'}| = |M_0| \cdot |M_{pp \rightarrow pp}|, \quad (\text{C.6})$$

where, M_0 accounts for all possible primary production processes and $M_{pp \rightarrow pp}$ describes the elastic interaction of protons in the exit channel. Combining equations C.4, C.5 and C.6 one obtains:

$$\sigma_{pp \rightarrow pp\eta'} = \frac{\int dp dq p q^2 \delta\left(p - \sqrt{\frac{m_{\eta'} + 2m_p}{4m_{\eta'}}} (q_{max}^2 - q^2)\right) |M_0|^2}{C^4 \cdot p^2 + \left(-\frac{1}{a_{pp}} + \frac{b_{pp} \cdot p^2}{2} - \frac{P_{pp} \cdot p^4}{1 + Q_{pp} \cdot p^2} - 2 \cdot p \cdot \eta_c \cdot h(\eta_c)\right)^2} \cdot \frac{8 (2\pi)^3 (2m_p + m_{\eta'}) \sqrt{m_{\eta'}^2 + 4m_p m_{\eta'}}}{m_p m_{\eta'}}, \quad (\text{C.7})$$

which, after the integration over p under the assumption that $|M_0|$ is constant gives:

$$\sigma_{pp \rightarrow pp\eta'} = \frac{|M_0|^2 \cdot \int_0^{q_{max}} \frac{dq \cdot p \cdot q^2}{C^4 \cdot p^2 + \left(-\frac{1}{a_{pp}} + \frac{b_{pp} \cdot p^2}{2} - \frac{P_{pp} \cdot p^4}{1 + Q_{pp} \cdot p^2} - 2 \cdot p \cdot \eta_c \cdot h(\eta_c)\right)^2}}{8 (2\pi)^3 (2m_p + m_{\eta'}) \sqrt{m_{\eta'}^2 + 4m_p m_{\eta'}} m_p m_{\eta'}}, \quad (\text{C.8})$$

where, $p = \sqrt{\frac{m_{\eta'} + 2m_p}{4m_{\eta'}}} (q_{max}^2 - q^2)$, and $q_{max} = \sqrt{\frac{4 \cdot Q \cdot m_{\eta'} \cdot m_p}{2 \cdot m_p + m_{\eta'}}}$, as shown in appendix F, with Q denoting the centre-of-mass excess energy.

²“Watson has suggested a procedure to separate the energy dependence due to the final state interaction between two collision partners from the reaction amplitude. In essence, the procedure involves expressing the square of the matrix element as a term that varies slowly with energy times the s-wave elastic-scattering of the two particles. The method is valid if the relative momentum between the interacting particles is small, and the final state interaction is strong compared with the primary reaction” [156].

D. Dominant partial waves

The reaction $pp \rightarrow pp\eta'$ is defined by quantum numbers for the initial $|pp\rangle$ and final $|pp\eta'\rangle$ states, with the following representation:

$$|p; {}^{2S+1}L_J; T\rangle \quad (\text{D.1})$$

for the $|pp\rangle$ state where, p denotes the proton-proton relative momentum, $L = 0, 1, \dots$ - the orbital angular momentum, $S = 0, 1$ - the spin, $T = 1$ - the isospin, and J the total angular momentum¹. Using the Jacobi coordinates system (see appendix E) one may represent the $|pp\eta'\rangle$ state as:

$$|p; q; {}^{2s+1}l_j; \lambda; T; J; M\rangle, \quad (\text{D.2})$$

where, q denotes the η' momentum relative to the pp system, λ - the angular momentum of the η' according to the proton pair, M - the projection of the total spin J , and l, s and j describes the angular momentum, spin, and the total angular momentum of the protons pair, respectively.

In practice, however, describing the $pp \rightarrow pp\eta'$ reaction one writes only non-trivial parameters², and hence the transition between $|pp\rangle$ and $|pp\eta'\rangle$ states reads:

$${}^{2S+1}L_J \rightarrow {}^{2s+1}l_j \lambda. \quad (\text{D.3})$$

For the measurements far above threshold, both the initial and final states will be a superposition of many partial waves.

This work concerns the measurements of the $pp \rightarrow pp\eta'$ reaction at an excess energy range from $Q = 1.5 \text{ MeV}$ to $Q = 4.1 \text{ MeV}$. The excess energy $Q = 4.1 \text{ MeV}$ means that the η' meson is always produced with the momentum smaller than ${}^3q_{max}(Q) = 72 \text{ MeV}/c$ in the centre-of-mass system.

The range of the strong interaction causing the η' production is of the limited extent. It is certainly not longer than the one defined by the exchange of the π^0 meson, which is of the order of $r_0 = \frac{\hbar}{m_{\pi}c} \approx 1.5 \text{ fm}$ according to the Yukawa

¹The Pauli principle requires that: $(-1)^{L+S+T} = -1$.

²The “p”, in the initial channel, is skipped because one knows it from the known proton beam momentum. Similarly “T” in the initial channel is 1 and it remains 1 after reactions. In the measurement of the total cross section one is not interesting in the values of “p” and “q” in the final state. And finally the total angular momentum “J” in the exit channel is skipped because it must be equal to “J” before reaction.

³The maximum η' momentum in the centre-of-mass system can be expressed as: (for the derivation see appendix F) $q_{max}^2 = \frac{4 \cdot Q \cdot m_{\eta'} \cdot m_p}{2 \cdot m_p + m_{\eta'}}$

parametrization⁴. Thus, classically, the centre-of-mass angular momentum of the produced η' , in the studied energy range ($Q \leq 4.1 \text{ MeV}$), is smaller than⁵:

$$r_0 \cdot q_{max} = \frac{\hbar}{m_\pi c} \cdot q_{max} \approx 0.5 \hbar. \quad (\text{D.4})$$

Therefore, one can safely assume that the centre-of-mass angular momenta larger than $0 \hbar$ will not play an important role in the η' production, which proves that only s-wave production should be significant for all energy point described in this work. This implies that both l and λ from equation D.3 are equal to zero.

If the orbital angular momentum of the proton pair is $l = 0$ than the Pauli excluding principle requires that $s = 0$ (the proton spins must be antiparallel) and hence, j and also the total spin in the exit channel must be zero. Thus, near threshold only $^1S_0 s$ state will play an important role in the exit channel. The parity of the $|pp\eta'\rangle$ system amounts to⁶: $P_{pp\eta'} = (-1)^{l+\lambda} \cdot P_{\eta'} = -1$. The negative parity requires L from the initial channel to be odd ($P_{pp} = (-1)^L$). Hence, according to the Pauli principle, the spin S of the $|pp\rangle$ system must be equal to 1. $L = 1, 3, \dots$, $S = 1$, and $J = 0$, which implies that L must be equal to 1, since L and S should add to J .

Thus, for beam momenta, for which the assumption that $l = 0$ and $\lambda = 0$ is justified, one concludes that the $pp \rightarrow pp\eta'$ reaction dominantly occurs through the transition between the following partial waves:

$$^3P_0 \rightarrow ^1S_0 s. \quad (\text{D.5})$$

Therefore, for the measurements presented in this work ($Q \leq 4.1$) it is enough to consider only the above transition especially that the next exit state $^1S_0 p$ is forbidden.

⁴According to Yukawa parametrization the interaction potential defined by the pion exchange can be described as follows: $V(r) = g \frac{1}{r} \cdot e^{-\frac{r}{r_0}}$, where $r_0 = \frac{\hbar}{m_\pi c}$, and g stands for the coupling constant [157].

⁵Gell-Mann and Watson [158] have argued that the orbital angular momenta of the meson, in the centre-of-mass system, greater than $l \hbar = \frac{p \hbar}{m c}$ will not play an important role for the $pp \rightarrow ppX$ reactions. Here “m” and “p” denote the mass and momentum of the produced meson, respectively.

⁶The η' meson has the following quantum numbers: $I^G(J^{PC}) = 0^+(0^{-+})$ [25].

E. Jacobi coordinates system

Let us consider three particles with masses m_1 , m_2 and m_3 placed in the positions \vec{r}_1 , \vec{r}_2 and \vec{r}_3 respectively. Usually it is more convenient to describe the position of three particles by means of a Jacobi coordinates. Then one can use the vector of the centre-of-mass \vec{R}_{CM} , the relative vector of particles 1 and 2 \vec{r} , and the vector between the third particle and the centre-of-mass of the first and the second ones $\vec{\rho}$. See figure below.

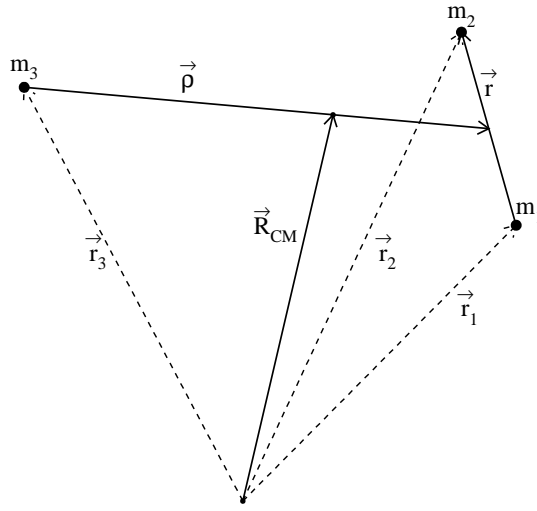


Figure E.1: Definition of the Jacobi coordinates system

The transformation from Cartesian to Jacobi coordinates and vice versa are given by the following matrices:

$$\begin{bmatrix} \vec{R}_{CM} \\ \vec{r} \\ \vec{\rho} \end{bmatrix} = \begin{bmatrix} \frac{m_1}{M} & \frac{m_2}{M} & \frac{m_3}{M} \\ -1 & 1 & 0 \\ \frac{m_1}{m_1+m_2} & \frac{m_2}{m_1+m_2} & -1 \end{bmatrix} \begin{bmatrix} \vec{r}_1 \\ \vec{r}_2 \\ \vec{r}_3 \end{bmatrix} \quad (\text{E.1})$$

$$\begin{bmatrix} \vec{r}_1 \\ \vec{r}_2 \\ \vec{r}_3 \end{bmatrix} = \begin{bmatrix} 1 & -\frac{m_2}{m_1+m_2} & \frac{m_3}{M} \\ 1 & \frac{m_1}{m_1+m_2} & \frac{m_3}{M} \\ 1 & 0 & -\frac{m_1+m_2}{M} \end{bmatrix} \begin{bmatrix} \vec{R}_{CM} \\ \vec{r} \\ \vec{\rho} \end{bmatrix} \quad (\text{E.2})$$

where $M = m_1 + m_2 + m_3$.

Now we shall calculate the canonically conjugated momenta \vec{P} , \vec{p} and \vec{q} corresponding to the Jacobi coordinates \vec{R}_{CM} , \vec{r} and $\vec{\rho}$ respectively. According to the definition they are given by:

$$\vec{P} = -i \frac{\partial}{\partial \vec{R}_{CM}}, \quad \vec{p} = -i \frac{\partial}{\partial \vec{r}}, \quad \vec{q} = -i \frac{\partial}{\partial \vec{\rho}}. \quad (\text{E.3})$$

Thus,

$$\begin{aligned} \vec{P} &= -i \frac{\partial \vec{r}_1}{\partial \vec{R}_{CM}} \frac{\partial}{\partial \vec{r}_1} - i \frac{\partial \vec{r}_2}{\partial \vec{R}_{CM}} \frac{\partial}{\partial \vec{r}_2} - i \frac{\partial \vec{r}_3}{\partial \vec{R}_{CM}} \frac{\partial}{\partial \vec{r}_3} = -i \frac{\partial}{\partial \vec{r}_1} - i \frac{\partial}{\partial \vec{r}_2} - i \frac{\partial}{\partial \vec{r}_3} = \\ &= \vec{p}_1 + \vec{p}_2 + \vec{p}_3, \end{aligned} \quad (\text{E.4})$$

$$\begin{aligned} \vec{p} &= -i \frac{\partial \vec{r}_1}{\partial \vec{r}} \frac{\partial}{\partial \vec{r}_1} - i \frac{\partial \vec{r}_2}{\partial \vec{r}} \frac{\partial}{\partial \vec{r}_2} - i \frac{\partial \vec{r}_3}{\partial \vec{r}} \frac{\partial}{\partial \vec{r}_3} = i \frac{m_2}{m_1 + m_2} \frac{\partial}{\partial \vec{r}_1} - i \frac{m_1}{m_1 + m_2} \frac{\partial}{\partial \vec{r}_2} \\ &= \frac{m_1 \vec{p}_2 - m_2 \vec{p}_1}{m_1 + m_2}, \end{aligned} \quad (\text{E.5})$$

$$\begin{aligned} \vec{q} &= -i \frac{\partial \vec{r}_1}{\partial \vec{\rho}} \frac{\partial}{\partial \vec{r}_1} - i \frac{\partial \vec{r}_2}{\partial \vec{\rho}} \frac{\partial}{\partial \vec{r}_2} - i \frac{\partial \vec{r}_3}{\partial \vec{\rho}} \frac{\partial}{\partial \vec{r}_3} = -i \frac{m_3}{M} \frac{\partial}{\partial \vec{r}_1} - i \frac{m_3}{M} \frac{\partial}{\partial \vec{r}_2} + i \frac{m_1 + m_2}{M} \frac{\partial}{\partial \vec{r}_3} \\ &= \frac{m_3}{M} \vec{p}_1 + \frac{m_3}{M} \vec{p}_2 - \frac{m_1 + m_2}{M} \vec{p}_3 = \frac{m_3(\vec{p}_1 + \vec{p}_2) - (m_1 + m_2)\vec{p}_3}{M}. \end{aligned} \quad (\text{E.6})$$

The matrix transforming Cartesian to the Jacobi momenta, and the opposite one are as follows:

$$\begin{bmatrix} \vec{P} \\ \vec{p} \\ \vec{q} \end{bmatrix} = \begin{bmatrix} 1 & 1 & 1 \\ -\frac{m_2}{m_1 + m_2} & \frac{m_1}{m_1 + m_2} & 0 \\ \frac{m_3}{M} & \frac{m_3}{M} & -\frac{m_1 + m_2}{M} \end{bmatrix} \begin{bmatrix} \vec{p}_1 \\ \vec{p}_2 \\ \vec{p}_3 \end{bmatrix} \quad (\text{E.7})$$

$$\begin{bmatrix} \vec{p}_1 \\ \vec{p}_2 \\ \vec{p}_3 \end{bmatrix} = \begin{bmatrix} \frac{m_1}{M} & -1 & \frac{m_1}{m_1 + m_2} \\ \frac{m_2}{M} & 1 & \frac{m_2}{m_1 + m_2} \\ \frac{m_3}{M} & 0 & -1 \end{bmatrix} \begin{bmatrix} \vec{P} \\ \vec{p} \\ \vec{q} \end{bmatrix} \quad (\text{E.8})$$

Now it will be demonstrated that in the nonrelativistic approximation $\vec{p} = \mu \dot{\vec{r}}$ and $\vec{q} = \nu \dot{\vec{\rho}}$, where μ is the reduced mass of particles 1 and 2 and ν is the reduced mass of particle 3 and the subsystem of particles 1 and 2.

$$\vec{p} = \frac{m_1 \vec{p}_2 - m_2 \vec{p}_1}{m_1 + m_2} = \frac{m_1 m_2 \dot{\vec{r}}_2 - m_2 m_1 \dot{\vec{r}}_1}{m_1 + m_2} = \frac{m_1 m_2}{m_1 + m_2} (\dot{\vec{r}}_2 - \dot{\vec{r}}_1) = \mu \dot{\vec{r}} \quad (\text{E.9})$$

$$\begin{aligned}
 \vec{q} &= \frac{m_3(\vec{p}_1 + \vec{p}_2) - (m_1 + m_2)\vec{p}_3}{M} = \frac{m_3(\dot{r}_1 m_1 + \dot{r}_2 m_2) - (m_1 + m_2)\dot{r}_3 m_3}{M} = \\
 &= \frac{(m_1 + m_2)m_3 \frac{\dot{r}_1 m_1 + \dot{r}_2 m_2}{m_1 + m_2} - (m_1 + m_2)\dot{r}_3 m_3}{M} = \\
 &= \frac{m_3(m_1 + m_2) \left(\frac{\dot{r}_1 m_1 + \dot{r}_2 m_2}{m_1 + m_2} - \dot{r}_3 \right)}{M} = \\
 &= \frac{(m_1 + m_2)m_3}{M} \dot{\rho} = \nu \dot{\rho} \tag{E.10}
 \end{aligned}$$

In the nonrelativistic case \vec{q} is equivalent to the momentum of particle 3 in the centre-of-mass system and \vec{p} is equal to the momentum of particle 2 in the centre-of-mass of the subsystem of particles 1 and 2.

Let us now verify the last statement. The momentum of particle 3 in the centre-of-mass system is equal to $m_3 \vec{v}_3^*$, where $\vec{v}_3^* = \vec{v}_3 - \vec{V}_{CM}$. Therefore:

$$\begin{aligned}
 \vec{p}_3^* &= m_3 \dot{r}_3^* = m_3 \dot{r}_3 - m_3 \dot{R}_{CM} = m_3 \dot{r}_3 - m_3 \frac{\dot{r}_1 m_1 + \dot{r}_2 m_2 + \dot{r}_3 m_3}{M} = \\
 &= \frac{M \dot{r}_3 - m_3(\dot{r}_1 + \dot{r}_2 + \dot{r}_3)}{M} = \frac{(m_1 + m_2)\dot{r}_3 - m_3(\dot{r}_1 + \dot{r}_2)}{M} = -\vec{q} \tag{E.11}
 \end{aligned}$$

Similarly, it will be shown that \vec{p} is equivalent to the momentum of particle 2 in the centre-of-mass of the subsystem of particles 1 and 2. A vector of the centre-of-mass of the subsystem of particles 1 and 2 is equal to $\frac{m_2 \vec{r}_2 + m_1 \vec{r}_1}{m_1 + m_2}$. Thus the momentum of particle 2 in the (2,1) centre-of-mass system can be expressed as:

$$m_2 \left[\dot{r}_2 - \left(\frac{m_2 \dot{r}_2 + m_1 \dot{r}_1}{m_1 + m_2} \right) \right] = \frac{m_2 m_1 (\dot{r}_2 - \dot{r}_1)}{m_1 + m_2} = \mu \dot{r} = \vec{p} \tag{E.12}$$

The nice feature of the transformation from Cartesian to Jacobi coordinates is that its Jacobian is equal to unity, as it is shown below:

$$\begin{aligned}
 \left| \frac{\partial(\vec{p}_1, \vec{p}_2, \vec{p}_3)}{\partial(\vec{P}, \vec{p}, \vec{q})} \right| &= \left| \begin{array}{ccc} \frac{\partial \vec{p}_1}{\partial \vec{P}} & \frac{\partial \vec{p}_1}{\partial \vec{p}} & \frac{\partial \vec{p}_1}{\partial \vec{q}} \\ \frac{\partial \vec{p}_2}{\partial \vec{P}} & \frac{\partial \vec{p}_2}{\partial \vec{p}} & \frac{\partial \vec{p}_2}{\partial \vec{q}} \\ \frac{\partial \vec{p}_3}{\partial \vec{P}} & \frac{\partial \vec{p}_3}{\partial \vec{p}} & \frac{\partial \vec{p}_3}{\partial \vec{q}} \end{array} \right| = \left| \begin{array}{ccc} \frac{m_1}{M} & -1 & \frac{m_1}{m_1 + m_2} \\ \frac{m_2}{M} & 1 & \frac{m_2}{m_1 + m_2} \\ \frac{m_3}{M} & 0 & -1 \end{array} \right| = \\
 &= \left| \frac{m_3}{M} \begin{array}{cc} -1 & \frac{m_1}{m_1 + m_2} \\ 1 & \frac{m_2}{m_1 + m_2} \end{array} \right| - \left| \begin{array}{cc} \frac{m_1}{M} & -1 \\ \frac{m_2}{M} & 1 \end{array} \right| =
 \end{aligned}$$

$$= \left| \frac{m_3}{M} \left(-\frac{m_2}{m_1 + m_2} - \frac{m_1}{m_1 + m_2} \right) - \frac{m_1}{M} - \frac{m_2}{M} \right| = \left| -\frac{m_3}{M} - \frac{m_1}{M} - \frac{m_2}{M} \right| = 1 \quad (\text{E.13})$$

F. Reaction kinematics

Let us consider $pp \rightarrow pp\eta'$ reaction with the following notation:

- m_p - proton mass,
- $m_{\eta'}$ - η' meson mass,
- E_b - total beam energy,
- p_b - beam momentum,
- T - kinetic beam energy,
- Q - excess energy \equiv kinetic energy available in the exit channel
in the centre-of-mass system,
- s - Mandelstam variable \equiv square of the total four-momentum vector,
- q_{max} - maximum η' meson momentum in the centre-of-mass system,
- p_{max} - maximum momentum of either proton in the proton-proton centre-of-mass system.

Laboratory system:

$$P_b = (E_b, \vec{p}_b) = (T + m_p, \vec{p}_b) - \text{beam four momentum vector}$$

$$P_T = (m_p, \vec{0}) - \text{target four momentum vector}$$

$$s = (P_b + P_T)^2 = (E_b + m_p, \vec{p}_b)^2 = (E_b + m_p)^2 - p_b^2$$

Centre-of-mass system:

$$P_b^* = (E_b^*, \vec{p}_b^*)$$

$$P_T^* = (E_T^*, \vec{p}_T^*) = (E_b^*, -\vec{p}_b^*)$$

$$s = (P_b^* + P_T^*)^2 = (E_b^* + E_T^*)^2 = (Q + 2m_p + m_{\eta'})^2$$

$$s = 2m_p(E_b + m_p) \qquad E_b = \frac{s}{2m_p} - m_p$$

$$s = 2m_p(T + 2m_p) \qquad T = \frac{s}{2m_p} - 2m_p$$

$$s = 2m_p(\sqrt{m_p^2 + \vec{p}_b^2} + m_p) \qquad p_b = \sqrt{\left(\frac{s}{2m_p} - m_p\right)^2 - m_p^2}$$

$$s = (Q + 2m_p + m_{\eta'})^2 \qquad Q = \sqrt{s} - 2m_p - m_{\eta'}$$

Values at threshold:

$$s_{threshold} = (2m_p + m_{\eta'})^2$$

$$T_{threshold} = \frac{m_{\eta'}^2}{2m_p} + 2m_{\eta'}, \quad p_{b-threshold} = \sqrt{\left(m_p + 2m_{\eta'} + \frac{m_{\eta'}^2}{2m_p}\right)^2 - m_p^2}$$

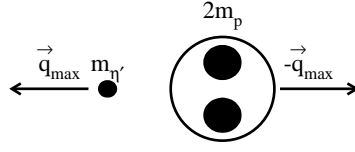


Figure F.1: The produced meson has a maximum momentum if both protons are emitted with the same momentum vector.

According to Figure F.1 s can be expressed as follows:

$s = (E_{\eta'}^* + E_{2p}^*)^2 = \left(\sqrt{q_{max}^2 + m_{\eta'}^2} + \sqrt{q_{max}^2 + 4 \cdot m_p^2} \right)^2$, and solving for q_{max} one obtains:

$$q_{max} = \frac{1}{2} \sqrt{\frac{(s - 4 \cdot m_p^2 - m_{\eta'}^2)^2 - 16 \cdot m_p^2 \cdot m_{\eta'}^2}{s}}$$

The nonrelativistic approximation gives:

$$s = \left(\frac{q_{max}^2}{2 \cdot m_{\eta'}} + \frac{q_{max}^2}{4 \cdot m_p} + 2 \cdot m_p + m_{\eta'} \right)^2, \text{ and}$$

$$q_{max} = \sqrt{\frac{(\sqrt{s} - 2 \cdot m_p - m_{\eta'}) \cdot 4 \cdot m_{\eta'} \cdot m_p}{2 \cdot m_p + m_{\eta'}}} = \sqrt{\frac{4 \cdot Q \cdot m_{\eta'} \cdot m_p}{2 \cdot m_p + m_{\eta'}}} \quad (\text{F.1})$$

If the produced η' meson is in the rest in the reaction centre-of-mass system then the outgoing protons have a maximum relative momentum, and their centre-of-mass system is identical with the reaction centre-of-mass. In this case the kinetic energy of each proton is equal to the half of the excess energy Q and hence, the maximum proton momentum in the proton-proton centre-of-mass system can

be expressed as: $p_{max} = \sqrt{\left(\frac{Q}{2} + m_p\right)^2 - m_p^2}$.

It can be shown that the following approximation:

$$\mathbf{p}_b^{\text{above}} \approx \mathbf{E}_b^{\text{above}} \approx \mathbf{3} \cdot \mathbf{Q} \quad (\text{F.2})$$

is valid for the $pp \rightarrow pp\eta'$ reaction close to threshold, where p_b^{above} and E_b^{above} indicate the beam momentum and energy above threshold, respectively.

In the remaining part the second approximation will be proved:

$$\begin{aligned}
Q &= \sqrt{s} - 2 \cdot m_p - m_{\eta'} \\
&= \sqrt{2 \cdot m_p \cdot (E_b + m_p)} - 2 \cdot m_p - m_{\eta'} \\
&= \sqrt{2 \cdot m_p \cdot (E_{b\text{-threshold}} + E_b^{\text{above}} + m_p)} - 2 \cdot m_p - m_{\eta'} \\
&= \sqrt{2 \cdot m_p \cdot \left(\frac{m_{\eta'}^2}{2 \cdot m_p} + 2 \cdot m_{\eta'} + m_p + E_b^{\text{above}} + m_p \right)} - 2 \cdot m_p - m_{\eta'} \\
&= \sqrt{m_{\eta'}^2 + 4 \cdot m_p^2 + 4 \cdot m_p \cdot m_{\eta'} + E_b^{\text{above}} \cdot 2 \cdot m_p} - 2 \cdot m_p - m_{\eta'} \\
&= (m_{\eta'} + 2 \cdot m_p) \cdot \sqrt{1 + \frac{E_b^{\text{above}} \cdot 2 \cdot m_p}{(m_{\eta'} + 2 \cdot m_p)^2}} - 2 \cdot m_p - m_{\eta'} \\
&\approx (m_{\eta'} + 2 \cdot m_p) \cdot \left(1 + \frac{1}{2} \cdot \frac{E_b^{\text{above}} \cdot 2 \cdot m_p}{(m_{\eta'} + 2 \cdot m_p)^2} + \dots \right) - 2 \cdot m_p - m_{\eta'} \\
&= m_{\eta'} + 2 \cdot m_p + \frac{E_b^{\text{above}} \cdot m_p}{m_{\eta'} + 2 \cdot m_p} - 2 \cdot m_p - m_{\eta'} \\
&\approx \frac{1}{3} \cdot E_b^{\text{above}}
\end{aligned}$$

Acknowledgement

I would like to thank my supervisor Prof. L. Jarczyk as well as Prof. W. Oelert, and Prof. K. Kilian for giving me the possibility to investigate many interesting reactions, together with the COSY - 11 group, at the accelerator in the Research Centre Jülich. The study of the mechanisms responsible for the production of the “elementary” particles is a very fascinating work. I owe a great debt to Prof. L. Jarczyk and Prof. A. Strzałkowski for introducing me into this interesting subject, and especially for teaching me and my friends, on a long seminars, how to connect phenomena with the abstract mathematical expressions.

I owe a great debt to Prof. L. Jarczyk and Prof. W. Oelert for their continuous interest and many remarks and suggestions during writing this thesis, and finally the correction of the whole work. I would like also to thank Dr. J. Smyrski, Dr. Ch. Hanhart, and Dr. J. Zejma for reading some parts of the manuscript.

I had an extraordinary luck to be guided in my work by Prof. W. Oelert. The work with him is a pure mental pleasure due to his invaluable experience, patience and tact.

I do wish to thanks all my friends from Cracow, Jülich, and Münster who shared the effort of performing the experiment and who helped me to carry the furniture to the long vehicle. Specifically, I owe a profound gratitude to:

Dr. J. Balewski for his help in analyzing the data,

Dr. H. Dombrowski, Dr. A. Khoukaz, T. Lister, C. Quentmeier, and C. Thomas for delivering a huge hydrogen clusters,

J. Foryciarz, J. Kuroś, J. Majewski, I. Pelmann, M. Prior, Dr. K. Pysz, S. Sewerin, R. Skibiński, Dr. M. Wolke, P. Wüstner and P. Żolnierczuk for the nice atmosphere during the daily work,

Dr. D. Grzonka and Dr. T. Sefzick for their kind and quick answers to various questions concerning the experimental apparatus and many other problems,

G. Schepers for his hospitality and for his patient in teaching me german language,

U. Seddik for teaching me arabic language,

M. Sokołowski for his trials to explain me the method of the track reconstruction,

W. Klimala and P. Kulesa for the fruitful discussions concerning this part of the nature which is still far from being described by physics.

I am thankful to the Research Centre Jülich for the financial support of my stay in Germany. Without the scholarship I was granted, the preparation of this thesis would not be possible.

Finally, I do appreciate the love and patience of my wife.

References

- [1] J. Haidenbauer, Ch. Hanhart, J. Speth, *Acta Phys. Pol.* **B 27** (1996), 2893
- [2] G. Fäldt, C. Wilkin, *Z. Phys.* **A 357** (1997), 241
- [3] H. Calèn et al., *Phys. Rev. Lett.* **79** (1997), 2642
- [4] A. Moalem et al., *Nucl. Phys.* **A 589** (1995), 649
- [5] N. Nikolaev, *CosyNews* **No. 3** May 1998, Published by the Forschungszentrum Jülich in Cooperation with CANU, the COSY User Organisation of the Universities
- [6] N. Nikolaev, IKP, FZ Jülich, Germany & Landau Ins., Russia, private communication
- [7] C. Hanhart, IKP, FZ Jülich, Germany, private communication
- [8] A.V. Efremov et al., *Phys. Rev. Lett.* **64**, (1990), 1495
- [9] C. Ernst et al., preprint nucl-th/9712069
W.K. Wilson et al, *Phys. Rev.* **C 57** (1998), 1865
- [10] *Experimental Techniques in Nuclear Physics*, edited by D.N. Poenaru and W. Greiner, Walter de Gruyter, Berlin · New York 1997
- [11] R. Wurzinger et al., *Phys. Lett.* **B 374** (1996), 283
- [12] Y. Le Bornec, *Nucl. Phys.* **A 553** (1993), 635c
see also IPNO-DRE 90.07
- [13] V. Flaminio, W.G. Moorhead, D.R.O. Morrison, N. Rivoire, CERN-HERA **84-01** (1984)
- [14] H. Müller, *Z. Phys.* **A 353** (1995), 103
H. Müller, *Z. Phys. A - Atomic Nuclei* **336** (1990), 103
H. Müller, K. Sistemich, *Z. Phys. A - Hadrons and Nuclei* **344** (1992), 197
H. Müller, *Z. Phys. A - Hadrons and Nuclei* **339** (1991), 409
- [15] R. Maier, *Nucl. Instr. & Meth. in Phys. Res.* **A 390** (1997), 1

- [16] H. Dombrowski et al., Nucl. Instr. & Meth. in Phys. Res. **A 386** (1997), 228
- [17] S. Brauksiepe et al., Nucl. Instr. and Meth. in Phys. Res. **A 376** (1996), 397,
D. Grzonka, W. Oelert, KFA-IKP(I)-1993-1
<http://ikpe1101.ikp.kfa-juelich.de/>
- [18] P. Moskal et al., Phys. Rev. Lett. **80** (1998), 3202, nucl-ex/9803002
- [19] P. Moskal for the COSY - 11 collaboration,
Investigation of the $pp \rightarrow pp\eta'$ reaction at COSY - 11,
COSY Proposal **No. 11.5**, IKP, FZ Jülich, november 1997,
and
*Proposal for the investigation of the $pp \rightarrow pp\eta'$ reaction
at the COSY - 11 detection system*,
COSY Proposal **No. 11.2**, IKP, FZ Jülich, march 1996,
and also
P. Moskal for the COSY-11 Collaboration
Annual Report, IKP, FZ Jülich 1997 p. 38
<http://ikpe1101.ikp.kfa-juelich.de/>
- [20] F. Hibou et al., preprint nucl-ex/9802002, accepted by Phys. Rev.
- [21] G.R Kalbfleisch et al., Phys. Rev. Lett. **12** (1964), 527
- [22] M. Goldberg et al., Phys. Rev. Lett. **12** (1964), 546
- [23] H. M. Pilkuhn, *Relativistic Particle Physics*,
Springer-Verlag New York, 1979
- [24] O. Nachtmann, *Elementary Particle Physics*,
Springer-Verlag Berlin Heidelberg, 1990
- [25] R.M. Barnett et al., *Review of Particle Physics*, Phys. Rev. **D 54** (1996)
- [26] T.-P. Cheng, L.-F. Li, *Gauge theory of elementary particle physics*,
Oxford University Press, 1991
- [27] F.J. Gilman, R. Kauffman, Phys. Rev. **D 36** (1987), 2761
see also Errata: Phys. Rev. **D 37** (1988), 3348
- [28] A. Bramon, R. Escribano, M.D. Scadron, hep-ph/9711229
- [29] M. D. Scadron, *Advanced Quantum Theory*,
Springer-Verlag Berlin Heidelberg, 1991
- [30] M. Bardadin-Otwinowska et al., Phys. Rev. **D 4** (1971), 2711
- [31] A.V. Kisselev, V.A. Petrov, Z. Phys. **C 58** (1993), 595

- [32] J.F. Donoghue, B.R. Holstein, Y.-C.R. Lin, *Phys. Rev. Lett.* **55** (1985), 2766
- [33] N.A. Roe et al, *Phys. Rev.* **D 41** (1990), 17
- [34] D. Antreasyan et al., *Phys. Rev.* **D 36** (1987), 2633
- [35] A. Duane et al., *Phys. Rev. Lett.* **32** (1974), 425
- [36] F. Butler et al., *Phys. Rev.* **D 42** (1990), 1368
- [37] D. Coffman et al., *Phys. Rev.* **D 38** (1988), 2695
- [38] R.M. Baltrusaitis et al., *Phys. Rev.* **D 32**, (1985), 2883
- [39] A. Bramon, R. Escribano, M.D. Scadron, hep-ph/9703313
- [40] B. Bagchi, A. Lahiri, S. Niyogi,
Phys. Rev. **D 41** (1990), 2871 and references therein.
- [41] H. Leutwyler, Preprint BUTP-96/5, hep-ph/9601236
- [42] D.J. Griffiths, *Introduction to Elementary Particles*,
John Wiley & Sons, Inc. New York 1987
- [43] J.L. Rosner, *Phys. Rev.* **D 27**, (1983), 1101
- [44] M.R. Pennington,
DTP-90/68, Proceedings of the Oxford Conference, September 1990
- [45] G. 't Hooft, *Phys. Rev. Lett.* **37** (1976), 8,
S. Weinberg, *Phys. Rev.* **D 11** (1975), 3583
- Talk given at the Workshop on the Structure of the η' Meson.
New Mexico State University and CEBAF, Las Cruces, New Mexico,
March 8, 1996, World Scientific, 1996, ISBN 981-02-3159-8
- [46] R.M. Davidson, page 79
- [47] M. Burkardt, J. Goity, page 1
- [48] G. Kilcup, page 9
- [49] A.R. Zhitnitsky, page 21
- [50] N.C. Mukhopadhyay, J.-F. Zhang, M. Benmerrouche, page 111
- [51] B. Diekmann, *Phys. Rep.* **159** (1988), 99
- [52] J.F. Donoghue, H. Gomm, *Phys. Lett.* **121B** (1983), 49
- [53] F. Lenz, *Nucl. Phys.* **B 279** (1987), 119

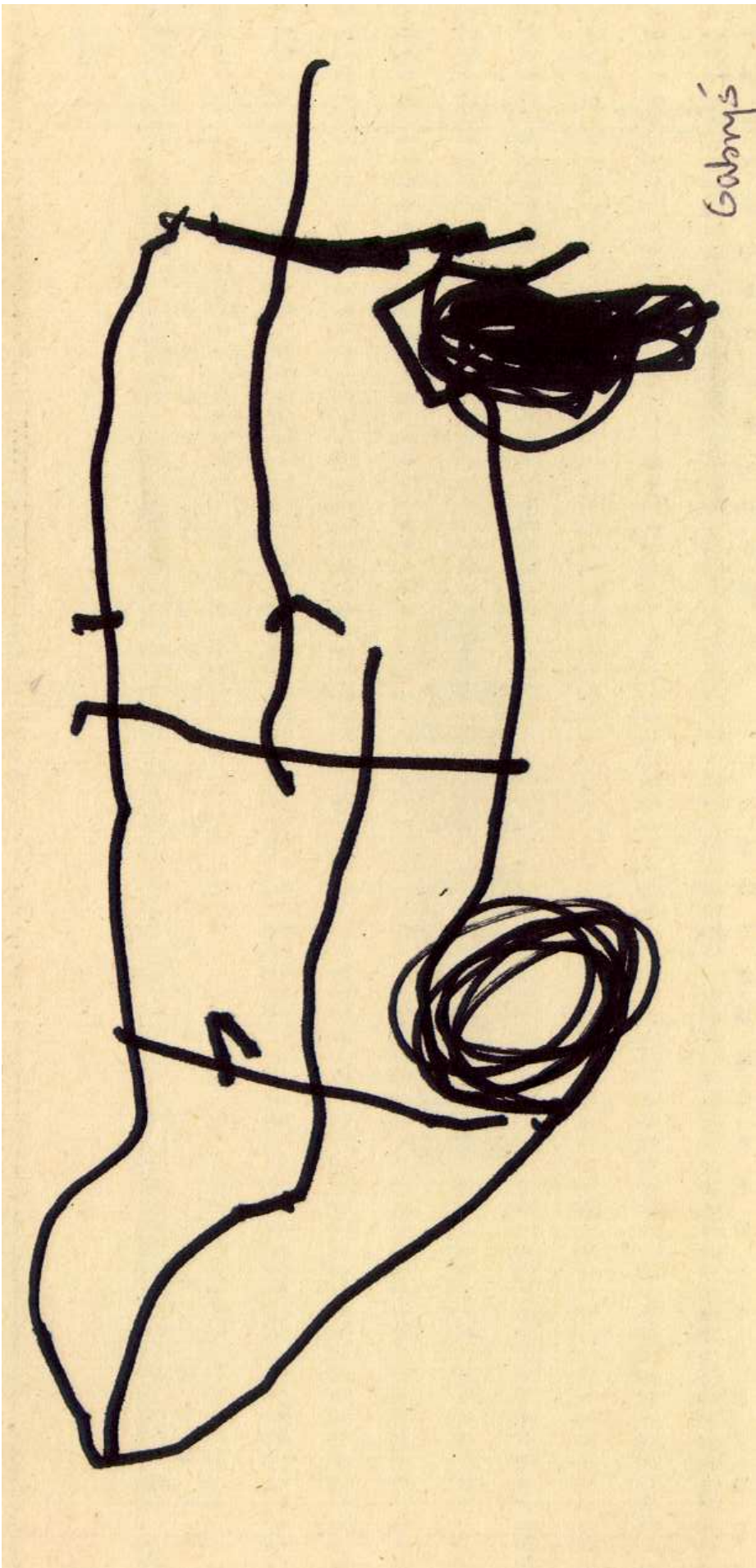
-
- [54] S. Al-Harran et al., Nucl. Phys. **B 183** (1981), 269
- [55] R.H. Capps, Phys. Rev. **D 17** (1978), 1862
- [56] H.J. Lipkin, Phys. Lett. **B 67** (1977), 65
- [57] E. Kawai, Phys. Lett. **B 124** (1983), 262
- [58] J.Jousset et al., Phys. Rev. **D 41**, (1990), 1389
- [59] M.L. Nekrasov, hep-ph/9503405
- [60] K. Geiger, B. Müller, W. Greiner,
Z. Phys. C - Particles and Fields **48** (1990), 257
- [61] F.E. Close, G.R. Farrar, Z. Li, hep-ph/9610280
- [62] F.E. Close, hep-ph/9610426
- [63] P. Ball et al., Phys. Lett. **B 365** (1996), 367
- [64] D. Atwood, A. Soni, hep-ph/9704357
- [65] D. Atwood, A. Soni, hep-ph/9706512
- [66] W.-S. Hou, B. Tseng, hep-ph/9705304 v2
- [67] E.V. Shuryak, A.R. Zhitnitsky, hep-ph/9706316
- [68] D.S. Koltun, A. Reitan, Phys. Rev. **141** (1966), 1413
- [69] H.O. Meyer et al., Phys. Rev. Lett. **65** (1990), 2846
- [70] H.O. Meyer et al., Nucl. Phys. **A 539** (1992), 633
- [71] A. Bondar et al., Phys. Lett. **B 356** (1995), 8
- [72] C. Hanhart et al., Phys. Lett. **B 358** (1995), 21
- [73] C.J. Horowitz, H.O. Meyer, D.K. Griegel, Phys. Rev. **C 49** (1994), 1337
- [74] E. Hernández, E. Oset, Phys. Lett. **B 350** (1995), 158
- [75] J.M. Laget et al., Phys. Lett **B 257** (1991), 254
- [76] U. Schuberth, Ph.D. dissertation at Uppsala University,
Acta Universitatis Upsaliensis **5**, 1995
- [77] B.L. Alvaredo, E. Oset, Phys. Lett. **B 324** (1994), 125
- [78] H. Calèn et al., Phys. Lett. **B 366** (1996), 39

- [79] E. Chiavassai et al., Phys. Lett. **B 322** (1994), 270
- [80] J.-F. Zhang et al., Phys. Rev. **C 52** (1995), 1134
- [81] S. Capstick, W. Roberts, Phys. Rev. **D 49** (1994), 4570
- [82] S. Capstick, N. Isgur, Phys. Rev. **D 34** (1986), 2809
- [83] J. Haidenbauer, IKP, FZ Jülich, Germany, private communication
- [84] M. Benmerrouche, N.C. Mukhopadhyay, Phys. Rev. **D 51** (1995), 3237
- [85] M. Benmerrouche, N.C. Mukhopadhyay, Phys. Rev. Lett. **67**, (1991), 1070
- [86] O. Dumbrajs et al., Nucl. Phys. **B 216** (1983), 277
- [87] M.M. Nagels et al., Nucl. Phys. **B 147** (1979), 189
M.M. Nagels et al., Few body systems and nucl. forces I, (1978), 17
- [88] W. Grein, P. Kroll, Nucl. Phys. **A 338** (1980), 332
- [89] I. Halperin, A. Zhitnitsky, hep-ph/9706251
- [90] B. Adeva et al., preprint CERN-EP/98-86, submitted to Phys. Rev. **D**
- [91] B. Adeva et al., preprint CERN-EP/98-85, submitted to Phys. Rev. **D**
- [92] D. Adams et al., preprint CERN-PPE/97-22, submitted to Phys. Rev. **D**
- [93] J. Ellis, M. Karliner, hep-ph/9601280 and references therein
- [94] G.M. Shore, G. Veneziano, Phys. Lett. **B 244** (1990), 75
- [95] V.W. Hughes et al., Phys. Lett. **B 212** (1988), 511
- [96] J. Ashman et al., Phys. Lett. **B 206** (1988), 364
- [97] J. Haidenbauer, K. Holinde, M.B. Johnson,
Phys. Rev. **C 45** (1992), 2055
- [98] A. Khoukaz,
Ph.D. dissertation at Westfälische Wilhelms-Universität Münster (1996)
- [99] G. Schepers,
Ph.D. dissertation at Westfälische Wilhelms-Universität Münster (1998)
- [100] LeCroy Corporation, Research System Division,
Chestnut Ridge, New York 10977-6499
- [101] B. Gugulski et al., Berichte des FZ Jülich, KFA-IKP(I)-1992-3, 1992

- [102] P.A. Żołnierczuk, Ph.D. dissertation at Jagellonian University, 1997
- [103] *Premium plastic and liquid scintillators*,
Bicron Corporation, Newbury, OH 44065, USA.
C.R. Hurlbut, *Plastic scintillators a survey*,
presented at the American Nucl. Soc. Winter Meeting, November, 1985
- [104] Thorn Emi Electron Tubes Ltd., Ruislip, Middlesex, England.
- [105] Hamamatsu Photonics K.K, Electron Tube Division, 314-5 Shimokanzo,
Toyooka-Village, Iwata-gun, Shizuoka-ken, 438.01, Japan.
- [106] P. Moskal, Diploma work at Jagellonian University,
Berichte des FZ Jülich; Jül-2825, 1993
- [107] William R. Leo, *Techniques for Nuclear and Particle Physics Experiments*,
Springer - Verlag Berlin Heidelberg, 1997
- [108] T. Tanimori et al., Nucl. Inst. and Meth. **216** (1983), 57
- [109] G. Anton et al., Nucl. Instr. and Meth. **A 310** (1991), 631
- [110] M. Wolke, Diploma work, Berichte des FZ Jülich; Jül-2825, 1993
- [111] M. Köhler et al., Berichte des FZ Jülich; Jül-3071, 1995
- [112] FIC 8234 Dual 68040 Fast Intelligent Controller, Users' Manual, Creative
Electronic Systems, Geneva, Switzerland (1992).
- [113] EXB-8500 Cartridge Tape Subsystem, User's Manual, EXABYTE Corp.,
Boulder, Colorado 80301 (1990)
- [114] M. Wolke, Ph.D. dissertation at Bonn-Universität Bonn (1998)
<http://ikpe1101.ikp.kfa-juelich.de/>
- [115] P. Wüstner, Ph.D. dissertation at Ruhr-Universität Bochum (1998)
- [116] K.H. Watzlawik et al., IEEE Trans. Nucl. Sci. **43**(1) (1996), 44
- [117] S. Brauksiepe, Diploma work, Berichte des FZ Jülich; Jül-3202, 1996
- [118] J. Majewski et al., Annual Report, IKP, FZ Jülich 1993 (1994) p. 249.
This units were designed especially for the use in the COSY - 11 experiments.
- [119] Michael Rook, Ph.D. dissertation at Bonn-Universität Bonn, Berichte des
FZ Jülich; Jül-2922, 1994
- [120] COSY - 11 collaboration, *Three Dimensional Magnetic Field in the COSY
dipole magnet*, Annual Report, IKP, FZ Jülich 1996 p. 38

- [121] Michael Rook, Diploma work at Köln-Universität, Berichte des FZ Jülich; Jül-2407, 1990
- [122] E. Byckling, K. Kajantie, *Particle Kinematics*, John Wiley & Sons Ltd. (1973) ISBN 0 471 12885 6
- [123] B. Maglič, G. Gosta, Phys. Lett. **18** (1965), 185
D. McLeod, Nucl. Inst. and Meth. **72** (1969), 333
- [124] J. Bystricky, J. Physique **48** (1987), 1901, and references therein.
- [125] D. Albers et al., Phys. Rev. Lett. **78** (1997), 1652, to receive the data contact: <http://www.iskp.uni-bonn.de/edda/> or edda-data@kaa.desy.de
- [126] R. Hagedorn, *Relativistic Kinematics*, W.A. Benjamin, Inc. New York (1964)
- [127] P. Moskal for the COSY-11 Collaboration
Annual Report, IKP, FZ Jülich 1996 p. 36
<http://ikpe1101.ikp.kfa-juelich.de/>
- [128] J.T. Balewski et al., Phys. Lett. **B 420** (1998), 211
and also, Phys. Lett. **B 388** (1996), 859
- [129] D. Prasuhn, IKP, FZ Jülich, Germany, private communication
- [130] GEANT-Detector Description and Simulation Tool, CERN Program Library Long Writeup W5013, CERN, 1211 Geneva 23, Switzerland 1993
- [131] G. Schepers, D. Prasuhn, Annual Report, IKP, FZ Jülich 1996 p. 47
C. Bovet et al., CERN/MPS-SI/INT. DL/70/4 (1970)
- [132] K. Wille, *Physik der Teilchenbeschleuniger und Synchrotronstrahlungsquellen*, B.G. Teubner Stuttgart (1992) ISBN 3-519-03087-X
- [133] Ch. Hanhart, Ph.D. dissertation at Bonn-Universität Bonn (1997)
- [134] R. Machleidt, K. Holinde, Ch. Elster,
Phys. Rep. (Rev. Sect. of Phys. Lett.) **149** (1987), 1
- [135] W. Cassing et al., Z. Phys. **A 340** (1991), 51; Z. Phys. **A 349** (1994), 77
- [136] *Stopping Powers and Ranges for Protons and Alpha Particles*, International Commission on Radiation Units and Measurements
7910 Woodmont Avenue, Bethesda, Maryland 20814, U.S.A., ICRU Report **49**
- [137] W.T. Eadie, D. Drijard, F.E. James, M. Roos, B. Sadoulet
Statistical Methods in Experimental Physics, North-Holland, 1971
Metody statystyczne w fizyce doświadczalnej, PWN 1989

- [138] A.M. Bergdolt et al. Phys. Rev. **D 48** (1993), R2969
- [139] COSY-11 Collaboration, Annual Report, IKP, FZ Jülich 1995 p. 39
- [140] K.M. Watson, Phys. Rev. **88** (1952), 1163
- [141] A. Moalem, L. Razdolskaja, E. Gedalin, BGU-94/04, hep-ph/9505264
- [142] J.P. Naisse, Nucl. Phys. **A 278** (1977), 506
- [143] C. Wilkin, Phys. Rev. **C 47** (1993), R938
- [144] J.-F. Germond, C. Wilkin, Nucl. Phys. **A 518** (1990), 308
- [145] G. Fäldt, C. Wilkin, Phys. Lett. **B 382** (1996), 209
- [146] C. Wilkin,
University College London, United Kingdom, private communication
- [147] J.T. Balewski et al., Eur. Phys. J. **A 2** (1998), 99-104
- [148] B. Kamys, Jagellonian University, Poland, private communication,
and Rev. of Mod. Phys. **62** (1990), 553
- [149] H. Calèn, Uppsala University, Sweden, private communication
- [150] I.J.R. Aitchison, A.J.G. Hey, *Gauge theories in particle physics*
Bristol, UK: Hilger (1989)
- [151] J.D. Bjorken, S.D. Drell, *Relativistic quantum mechanics*
McGraw-Hill, New York (1964)
- [152] D. Y. Wong, H.P. Noyes, Phys. Rev. **126** (1962), 1866
- [153] J.D. Jackson, J.M. Blatt, Rev. of Mod. Phys. **22** (1950), 77
- [154] H.A. Bethe, Phys. Rev. **76** (1949), 38
- [155] H.P. Noyes, H.M. Lipinski, Phys. Rev. **C 4** (1971), 995
- [156] H.O. Meyer, J.A. Niskanen, Phys. Rev. **C 47** (1993), 2474
- [157] T. Mayer-Kuckuk, *Fizyka jądrowa*, PWN, Warszawa 1987
- [158] M. Gell-Mann, K.M. Watson, Ann. Rev. Nucl. Sci. **4** (1954), 219



Gabon's